Energy Calibration for the Gerda and Legend-200 Experiments

Dissertation

zur

Erlangung der naturwissenschaftlichen Doktorwürde
(Dr. sc. nat.)

vorgelegt der
Mathematisch-naturwissenschaftlichen Fakultät
der

Universität Zürich

von

Chloe Ransom

aus
dem Vereinigten Königreich

Promotionskommission

Prof. Dr. Laura Baudis (Vorsitz)
Prof. Dr. Nicola Serra
Dr. Roman Hiller
Dr. Junting Huang

Zürich, 2021

ABSTRACT

Whether neutrinos are Majorana particles, i.e. their own antiparticles, has not yet been determined. In this case, processes such as neutrinoless double-beta ($0\nu\beta\beta$) decay could be observed in a number of isotopes. The signature of this decay would be a peak in the summed electron spectrum at $Q_{\beta\beta}$. Chapter 1 introduces neutrinos and $0\nu\beta\beta$ decay and describes how experimental sensitivity to this decay can be optimised, and the status of the field.

The GERDA experiment searched for $0\nu\beta\beta$ decay in ^{76}Ge (for which isotope $Q_{\beta\beta}$ = 2039.006 keV), and operated between November 2011 and November 2019 (Chapter 2). It achieved the lowest background level and most stringent half-life limit of any $0\nu\beta\beta$ decay experiment of $T_{1/2}^{0\nu\beta\beta} > 1.8 \cdot 10^{26}$ yr (90% C.L.).

In this work, the energy calibration analysis for the germanium detectors of GERDA is presented (Chapter 3). The energy scale of these detectors was determined via their weekly exposure to ^{228}Th sources. A major development of the final GERDA $0\nu\beta\beta$ decay analysis was the division of the data from each detector into stable sub-periods called partitions. For each partition, the effective energy resolution at $Q_{\beta\beta}$ was determined. The average resolutions ($\pm$ the standard deviation) at $Q_{\beta\beta}$ across the partitions for the BEGe/Coaxial/IC detectors are (2.8 ± 0.3) keV, (4.0 ± 1.3) keV and (2.9 ± 0.1) keV respectively. Dedicated studies were performed to study various sources of systematic uncertainties to the resolution at $Q_{\beta\beta}$, with an average total uncertainty of 0.13 keV. The energy bias for the events near $Q_{\beta\beta}$ was approximated as the residual of the single-escape peak of ^{208}Tl at 2.1 MeV in the combined spectra. The average bias is -0.1 keV with a standard deviation of 0.3 keV.

After the success of the GERDA experiment, the LEGEND collaboration aims to build the next generation of ^{76}Ge $0\nu\beta\beta$ decay experiments (Chapter 4). The first stage, LEGEND-200, is under construction, and aims to achieve a half-life sensitivity exceeding 10^{27} yr.

For the energy calibration of the germanium detectors, LEGEND-200 will operate Source Insertion Systems that are able to deploy multiple sources each, instead of just a single one as in GERDA (technical drawings can be found in Appendix A). Monte Carlo simulation studies were performed to determine the optimal source separations on the steel band, and the number and location of stopping points by the germanium detectors (Chapter 5). Assuming a nominal source activity of 5 kBq, the time required to determine a precise energy scale within the experimental constraints is 94 min,

excluding the time required to move the sources. As a comparison, Gerda required 135 min to calibrate around 40 kg of detectors.

In Appendix B the characterisation of a photomultiplier tube with a MgF$_2$ window is described. Unlike many other materials, MgF$_2$ is transparent to 128 nm wavelengths and thus is directly sensitive to the scintillation light of liquid argon.

CONTENTS

NEUTRINOS AND DOUBLE-BETA DECAY

There is a theory which states that if ever anyone discovers exactly what the Universe is for and why it is here, it will instantly disappear and be replaced by something even more bizarre and inexplicable. There is another theory mentioned, which states that this has already happened. - Douglas Adams, The Restaurant at the End of the Universe

1.1 THE STANDARD MODEL

The Standard Model of Particle Physics is one of the greatest achievements in the history of physics. It classifies all known elementary particles into fermions or bosons, as shown in Figure 1.1.
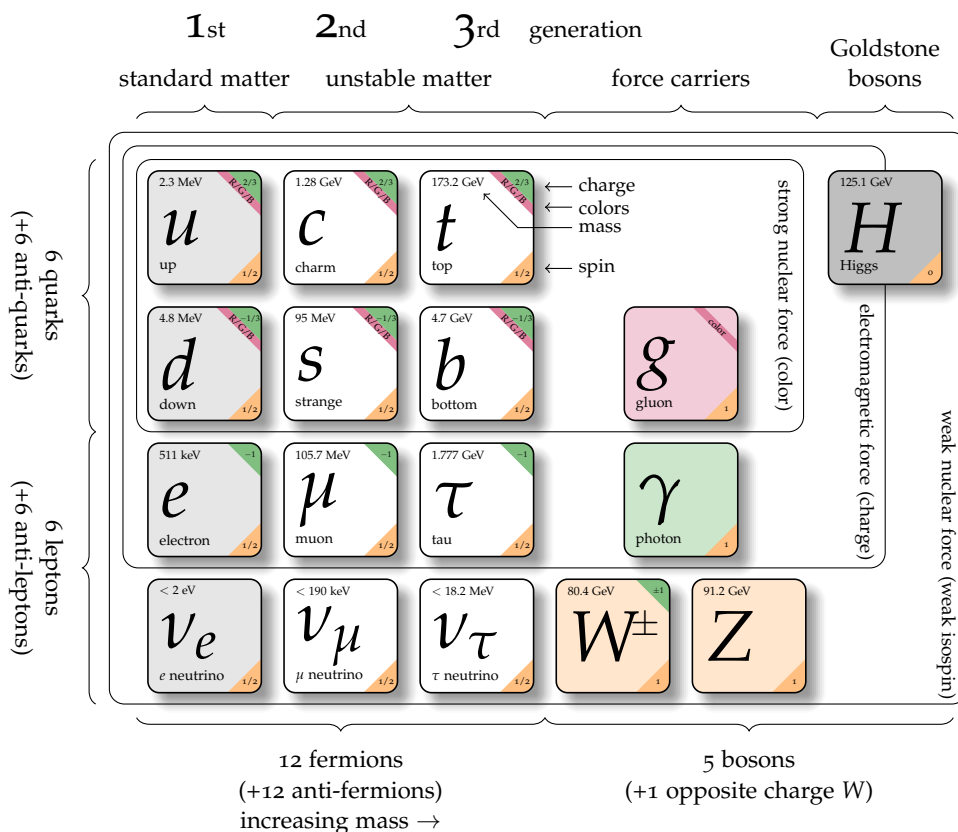

Figure 1.1: The Standard Model. From [1].

The six leptons and six quarks make up the fermions, and are in turn divided into three generations of isospin doublets. The lepton doublets are each composed of one electrically charged particle, and one uncharged

neutrino, as follows: (e^-, ν_e), (μ^-, ν_μ) and (τ^-, ν_τ). Similarly the charged quarks are coupled as follows: (u, d), (c, s) and (t, b).

The force transmitting bosons are the massless gluons, g (strong force), the massive $W^\pm$ and Z bosons (weak force) and the massless photon, γ (electromagnetic force). The weak force, mediated by the massive W and Z bosons and thus having a much shorter range than the other forces, couples to all the fermions. All fermions except the neutrinos carry electric charge and thus experience the electromagnetic force. The quarks possess colour charge and thus interact via the strong force. Since the gluons themselves also possess colour charge, they self-interact, and result in the phenomenon called confinement, where colour-charged particles cannot be isolated.

In addition to the fermions and force carrying bosons is the Higgs boson, a spin-0 particle. This boson is implied by the Higgs mechanism where electroweak symmetry breaking causes the Higgs field to obtain a vacuum expectation value. The breaking of the electroweak symmetry results in the W and Z bosons acquiring masses. In turn, the fermions gain masses (specifically, Dirac masses) through their coupling with the Higgs field.

Since its development in the 1970s, the Standard Model has been successful at predicting and explaining a range of phenomena. However, cracks have begun to appear, particularly in the realm of neutrinos. Assuming that neutrinos acquire their mass in the same way as the other fermions in the SM requires unnaturally small coupling constants, as well as the introduction of as-yet unobserved right-handed neutrinos. Alternatively, neutrinos may possess a Majorana mass, described more in Section 1.4, making possible beyond the Standard Model processes such as $0\nu\beta\beta$ decay, discussed in Section 1.5. This thesis was completed in the context of the GERDA and LEGEND collaborations which search for $0\nu\beta\beta$ decay. The study of these light particles, that remain elusive due to their weakly interacting nature, may yet uncover the next step in our understanding of the Universe.

1.2 DISCOVERY OF THE NEUTRINO(S)

Neutrino history can be said to have begun in 1911 with observations of the beta-decay energy spectrum by Meitner and Hahn [2]. In 1914, Chadwick determined that this energy spectrum was continuous [3], apparently violating the conservation of energy, momentum and angular momentum. The neutrino was then postulated by Pauli in 1930 to solve this problem [4]. Pauli suggested that an electrically neutral, spin $\frac{1}{2}$ particle emitted alongside the beta particle could carry missing energy away from the nucleus and thus explain the continuous spectrum. This particle would have to be extraordinary weakly interacting, to explain why it had not been observed in these beta-decay experiments. Fermi's theory of beta decay, writ-

ten in 1934, formalised the introduction of the neutrino, giving a theoretical framework to describe the decay of the neutron within a nucleus [5],

$$n \rightarrow p + \beta^- + \bar{\nu}_e. \tag{1.1}$$

From this understanding came proposals on how to look for the neutrino, ranging from the observation of the nuclear recoil in beta-capture [6] to neutrino-capture on a scintillating target [7]. It was by employing this latter approach that Cowan and Reines conclusively demonstrated the observation of the neutrino in 1956 [8].

The muon, discovered in cloud chamber cosmic rays experiments in 1936 [9, 10], was shown to decay to an electron and seemingly nothing else [11]. Following the intuition for beta decay, a neutrino (or a neutretto, as named at the time) was postulated to be also emitted [12]. In 1962 the muon neutrino was detected and distinguished from the electron neutrino by Leon Lederman, Melvin Schwartz and Jack Steinberger [13]. This was in turn followed by the tau neutrino discovery in 2000 at Fermilab [14], completing the picture of the three generations of neutrinos known today.

1.3 NEUTRINO OSCILLATIONS

Starting in 1962, the Homestake experiment set out to measure the solar neutrino flux, by employing the following reaction:

$$\nu_e + {}^{37}\text{Cl} \rightarrow e^- + {}^{37}\text{Ar}. \tag{1.2}$$

By 1992 it had become clear that the observed rate was distinctly lower than the rate predicted by the Standard Solar Model (SSM) [15]: a rate of only 2.5 SNU (Solar Neutrino Unit, 1 event per 10^{36} target atoms per second) was measured, while the SSM predicted between 6-8 SNU. This became known as the famous "Solar Neutrino Problem", and for many years, debate raged as to whether theoretical or experimental issues were at fault for the discrepancy. For a time, some feared that the Sun was burning out [16].

The solution to this puzzle finally came in 2001, with the SNO experiment. SNO measured the solar neutrino flux through neutral current events, which are sensitive to all neutrino flavours, as well as the electron neutrino flux through charged current events, as shown in Figure 1.2. It observed that the total neutrino flux was consistent with the SSM, with the electron neutrinos contributing approximately $\frac{1}{3}$ of the total [17].

This can be explained with neutrino flavour mixing, analogously to the quark sector, as discussed by Maki, Nakagawa and Sakata [18], and oscillations between them, as proposed by Pontecorvo in 1957 [19].
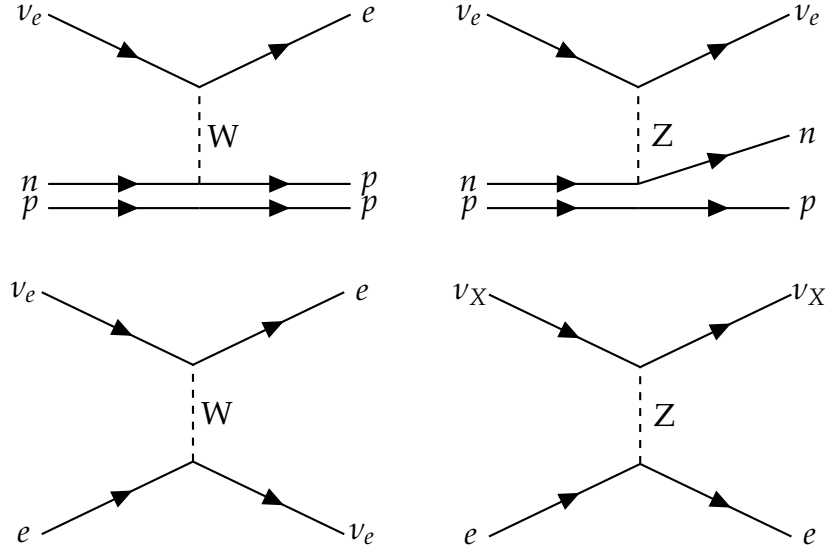
Figure 1.2: Neutrino interactions with deuterium in SNO. While all neutrino flavours can participate in neutral current (top right) and elastic scattering (bottom) interactions, only electron-neutrinos can partipate in charged current (top left) interactions.

If neutrinos are massive, and furthermore, the masses of the three neutrinos are not identical, then the three flavour eigenstates can be expressed as a superposition of the three mass eigenstates:

$$\nu_\alpha = \sum_{i=1}^{3} U_{\alpha i}\nu_i, \tag{1.3}$$

where i labels the mass eigenstates and α the flavour eigenstates: electron, muon and tau. U is the Pontecorvo-Maki-Nakagawa-Sakata (PMNS) matrix, a 3×3 unitary matrix, commonly parametrised by three mixing angles θ_{12}, θ_{23}, θ_{13}, a CP-violating phase δ_{CP} and the two Majorana phases α_1 and α_2, as follows:

$$U = \begin{pmatrix} 1 & 0 & 0 \\ 0 & c_{23} & s_{23} \\ 0 & -s_{23} & c_{23} \end{pmatrix} \cdot \begin{pmatrix} c_{13} & 0 & s_{13}e^{-i\delta_{CP}} \\ 0 & 1 & 0 \\ -s_{13}e^{i\delta_{CP}} & 0 & c_{13} \end{pmatrix} \cdot \begin{pmatrix} c_{21} & s_{12} & 0 \\ -s_{12} & c_{12} & 0 \\ 0 & 0 & 1 \end{pmatrix}$$
$$\cdot \begin{pmatrix} 1 & 0 & 0 \\ 0 & e^{i\alpha_1} & 0 \\ 0 & 0 & e^{i\alpha_2} \end{pmatrix}, \tag{1.4}$$

where $c_{ij} \equiv \cos\theta_{ij}$ and $s_{ij} \equiv \sin\theta_{ij}$ [20]. For Dirac neutrinos, $\alpha_1 = \alpha_2 = 0$, whereas for Majorana neutrinos (see Section 1.4), the phases α_1 and α_2 can take any value in the [0, 2π] range.

The transition probability between neutrino flavours α and β is given by

$$P_{\alpha \to \beta} = \delta_{\alpha\beta} - 4\sum_{i>j} \mathrm{Re}\left(U^*_{\alpha i}U_{\beta i}U_{\alpha j}U^*_{\beta j} \right)\sin^2\left(\frac{\Delta m^2_{ij}L}{4E} \right)$$
$$+ 2\sum_{i>j} \mathrm{Im}\left(U^*_{\alpha i}U_{\beta i}U_{\alpha j}U^*_{\beta j} \right)\sin\left(\frac{\Delta m^2_{ij}L}{2E} \right), \qquad (1.5)$$

where L is the distance travelled, E is the neutrino energy and $\Delta m^2_{ij} = m^2_i - m^2_j$ is the squared mass difference between mass eigenstates [21].

The above expression is valid for neutrino oscillations in a vacuum. When neutrinos instead travel through matter, their phase of oscillation is affected, since the electron neutrino component of the propagating mass eigenstates can scatter with the electrons through the charged current interaction. This effect is known as the MSW effect [22]. The two-neutrino equation of motion in matter can then be expressed as

$$i\frac{\mathrm{d}}{\mathrm{d}x}\begin{pmatrix} \nu_e \\ \nu_X \end{pmatrix} = 2\pi \begin{pmatrix} -\frac{\kappa\cos 2\theta}{L_{\mathrm{vacuum}}} + \frac{1}{L_{\mathrm{matter}}} & \frac{\kappa\sin 2\theta}{2L_{\mathrm{vacuum}}} \\ \frac{\kappa\sin 2\theta}{2L_{\mathrm{vacuum}}} & 0 \end{pmatrix}\begin{pmatrix} \nu_e \\ \nu_X \end{pmatrix}, \qquad (1.6)$$

where $\kappa = \mathrm{sign}(m^2_2 - m^2_1)$ and $L_{\mathrm{matter(vacuum)}}$ is the matter (vacuum) oscillation length in natural units, where the matter oscillation length depends on the electron density [23]. For anti-neutrinos the sign in front of $1/L_{\mathrm{matter}}$ is reversed.

Experimental evidence exists for neutrino oscillations in not only solar [24–30] neutrinos, but also reactor [31–33], atmospheric [34, 35] and accelerator [36–38] neutrinos. Global fits to this data have determined the PMNS matrix elements and the absolute value of the mass squared differences.

By exploiting the MSW effect in the propagation of solar neutrinos, the sign of Δm^2_{21} has also been measured [20]. As yet, the sign of Δm_{32} has not been determined since this requires the observation of muon neutrinos (produced on or near Earth) with very long baselines. Future long-baseline reactor oscillation experiments such as Dune [39] and T2HK [40,41] aim to measure this sign with high significance.

1.4 DIRAC OR MAJORANA FERMIONS

In the Standard Model (SM), neutrinos are assumed to be exactly massless [42]. In 1956, the Wu experiment demonstrated parity violation during the β decay of $^{60}\mathrm{Co}$ [43], and later experiments showed that parity is in fact maximally violated in weak interactions. Such evidence led Marshak and Sudarshan to propose the left-handed V–A form for the weak Lagrangian at a Padua-Venice conference in September 1957 [44,45], which

was then shortly followed by a Feynman and Gell-Mann paper outlining the same [46]. The Goldhaber experiment in 1958 showed that the neutrinos emitted in the electron capture decay of $^{152\text{m}}$Eu are always of negative helicity [47]. Since for a massless particle, helicity and chirality (handedness) are the same, the neutrino was introduced to the SM as a purely left-handed particle.

However, the existence of neutrino oscillations requires neutrinos to have a non-zero mass. The simplest way of accounting for the mass of the neutrino is analogous to the other fermions, by introducing right-handed gauge-singlet counterparts, ν_R [48]:

$$\mathcal{L}_D = -\overline{L}Y^\nu \Phi \nu_R. + \text{h.c.} \tag{1.7}$$

After spontaneous symmetry breaking, the Higgs acquires a vacuum expectation value, v, and the neutrino acquires a Dirac mass

$$m_D = \frac{v}{\sqrt{2}}Y^\nu, \tag{1.8}$$

although the Yukawa couplings Y^ν are unusually small (by several orders of magnitude), compared to the other fermions.

Alternatively, the neutrino, as the only electrically neutral fermion, could possess a Majorana mass term [49].

$$\mathcal{L}_M = -\frac{1}{2}\overline{\nu_L}M_L \nu_L^C + \text{h.c.} \tag{1.9}$$

This would require the neutrino to be identical to the anti-neutrino, violating lepton number conservation, such that the two observed particles are distinguished only by their chirality [48]. The observations of the Goldhaber experiment described above could be explained by the smallness of the neutrino mass, which makes helicity = chirality a good approximation for neutrinos.

The smallness of the neutrino masses can then be explained naturally, via the see-saw mechanism, which introduces heavy right-handed sterile neutrinos [50–52]. These mix with the known neutrinos, suppressing their masses.

$$\mathcal{L}_{\nu_R} = -\overline{L}Y^\nu \Phi \nu_R - \frac{1}{2}\overline{\nu_L^C}M_R \nu_R + \text{h.c.} \tag{1.10}$$

After spontaneous symmetry breaking, this can be rewriten by defining the doublet

$$\nu = \begin{pmatrix} \nu_L^C \\ \nu_R \end{pmatrix}, \tag{1.11}$$

i.e.

$$\mathcal{L}_{\nu_R} = \overline{\nu}\mathcal{M}\nu. \tag{1.12}$$

where

$$\mathcal{M} = \begin{pmatrix} 0 & m_D \\ m_D & M_R \end{pmatrix}. \tag{1.13}$$
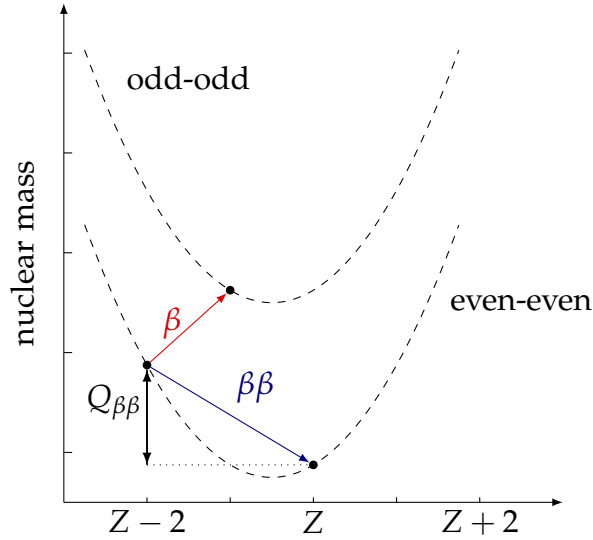
Figure 1.3: Isobaric mass parabolae for odd-odd (upper) and even-even (lower) nuclei. When a single β decay (red) is energetically forbidden, $\beta\beta$ decay (blue) may be observable. $Q_{\beta\beta}$ indicates the energy released in $\beta\beta$ decay, which is shared among the decay products. Adapted from [55] and [56].

This matrix can be diagonalised to find the mass eigenstates. In the see-saw limit, where $M_D \ll M_R$, the mass eigenstates are given by

$$m_\nu \sim -\frac{m_D^2}{M_R}, \quad \text{and} \quad M_N \sim M_R. \tag{1.14}$$

Additionally, the CP violating decay of these heavy sterile neutrinos could potentially explain the dominance of matter over antimatter today through leptogenesis [48, 53, 54].

1.5 DOUBLE-BETA DECAY

The SM process of neutrino accompanied double-beta ($2\nu\beta\beta$) decay is observable when β decay is either energetically forbidden (see Fig. 1.3) or suppressed due to angular momentum differences between mother and daughter nuclei [57]. Since this decay is a second-order process, the half-lives for $2\nu\beta\beta$ decay are among the longest observed, ranging from 10^{19} yr to 10^{24} yr [58].

If the neutrino is a Majorana fermion, that is, has a Majorana mass component, the hypothetical lepton number violating process of neutrinoless double-beta ($0\nu\beta\beta$) decay could be observed. The two processes are shown in Fig. 1.4, with the summed energy spectrum of the two emitted electrons in Fig. 1.5. Since the two neutrinos interact only weakly and therefore would not be detected by a $2\nu\beta\beta$ decay experiment, the only way to distinguish between the two processes is in the energy of the two emitted elec-
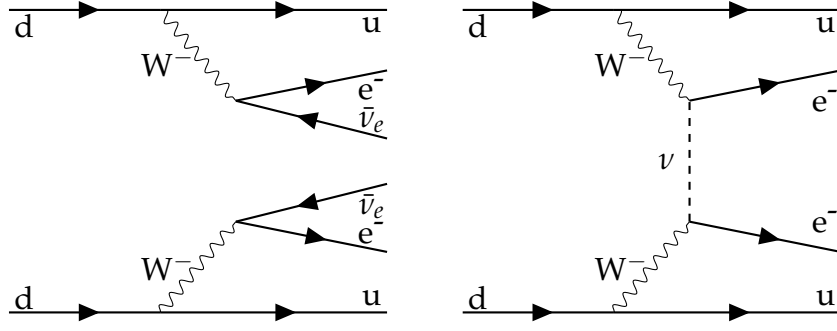
Figure 1.4: Feynman diagrams for $2\nu\beta\beta$ decay (left) and $0\nu\beta\beta$ decay (right). Adapted from [55].
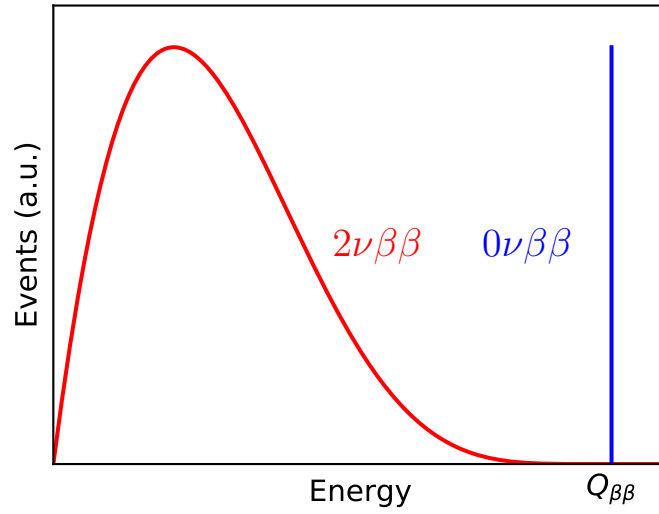
Figure 1.5: The summed energy spectrum of the two emitted electrons in $2\nu\beta\beta$ decay (red) and $0\nu\beta\beta$ decay (blue). The ratio of the two processes is unknown.

trons. $0\nu\beta\beta$ decay would exhibit a peak in the summed energy spectrum at $Q_{\beta\beta}$, while $2\nu\beta\beta$ produces a continuous spectrum [59], approximately given by

$$F(E) = (E^4 + 10E^3 + 40E^2 + 60E + 30)E(Q_{\beta\beta} - E)^5. \qquad (1.15)$$

In the simplest case where $0\nu\beta\beta$ decay is mediated by the exchange of a single light Majorana neutrino, the half-life is given by [60,61]

$$\left[T_{1/2}^{0\nu\beta\beta}\right]^{-1} = G_{0\nu}(Q_{\beta\beta}, Z)\,|M_{0\nu}|^2\,\frac{m_{\beta\beta}^2}{m_e^2}, \qquad (1.16)$$

where $G_{0\nu}$ is the phase space integral, $M_{0\nu}$ is the nuclear matrix element, m_e is the electron mass and $m_{\beta\beta}$ is the effective Majorana mass, given by

$$m_{\beta\beta} = \left|\sum_i U_{ei}^2 m_i\right|. \qquad (1.17)$$

1.6 ABSOLUTE MASS SCALE AND EFFECTIVE MAJORANA MASS

Oscillation experiments are not sufficient to determine the absolute mass scale of neutrinos [62], but they provide measurements on Δm_{ij}^2 as well as the absolute sign of Δm_{12}^2 (see Section 1.3). The absolute sign of Δm_{3l}^2 has not yet been determined. If Δm_{3l}^2 is positive, $m_1 < m_2 < m_3$, called the normal ordering (NO). Conversely, if Δm_{3l}^2 is negative, $m_3 < m_1 < m_2$, called the inverted ordering (IO). Current limits on Δm_{3l}^2 are [20]

$$\Delta m_{3l} = \begin{cases} \Delta m_{31}^2 = +2.525^{+0.033}_{-0.032} \cdot 10^{-3}\,\text{eV}^2 & \text{for NO,} \\ \Delta m_{32}^2 = -2.512^{+0.034}_{-0.032} \cdot 10^{-3}\,\text{eV}^2 & \text{for IO.} \end{cases} \tag{1.18}$$

Cosmological measurements provide a limit on the sum of the three neutrino masses Σ [63, 64]:

$$\Sigma = \sum_i^3 m_i < (0.12 - 0.66)\,\text{eV}. \tag{1.19}$$

Measurements of the end point of β decay spectra also probe the absolute mass scale of neutrinos, giving limits on the effective electron neutrino mass m_β [65]:

$$m_\beta = \sqrt{\sum_i \left| U_{ei}^2 \right| m_i^2} < 1.1\,\text{eV}. \tag{1.20}$$

Recent limits by KATRIN constrain $m_\beta < 1.1$ eV [65].

The effective Majorana mass can be expressed in terms of the mass of the lightest neutrino, m_{min}, as follows [66]. In the case of normal ordering:

$$m_1 = m_{\text{min}}$$
$$m_2 = \sqrt{m_{\text{min}}^2 + \Delta m_{21}^2}$$
$$m_3 = \sqrt{m_{\text{min}}^2 + \Delta m_{3l}^2}, \tag{1.21}$$

whereas for inverted ordering:

$$m_3 = m_{\text{min}}$$
$$m_1 = \sqrt{m_{\text{min}}^2 - \Delta m_{3l}^2 - \Delta m_{21}^2}$$
$$m_2 = \sqrt{m_{\text{min}}^2 - \Delta m_{3l}^2}. \tag{1.22}$$

Using equation 1.5, the effective Majorana mass can be expressed as the absolute value of a sum of three complex masses M_i:

$$\begin{aligned} |m_{\beta\beta}| &= \left| \sum_{i=1}^3 U_{ei}^2 m_i \right| \\ &= \left| c_{12}^2 c_{13}^2 m_1 + s_{12}^2 c_{13}^2 m_2 e^{i\alpha_1} + s_{13}^2 m_3 e^{i\alpha_2} \right| \\ &= |M_1 + M_2 + M_3| \end{aligned} \tag{1.23}$$

Fig. 1.6 shows the absolute value of these complex masses M_i, using best fit values for s_{12}^2, s_{13}^2, Δm_{21}^2 and Δm_{3l}^2 from [20]. For a certain range of m_{min}, depending on the Majorana phases α_1 and α_2, $m_{\beta\beta}$ may vanish in the normal ordering case. Fig. 1.7 shows the allowed parameter space for $m_{\beta\beta}$. The range of allowed values is given by varying the unknown Majorana phases between 0 and 2π. Notably, if the ordering is inverted, the minimum Majorana mass would be approximately 18 meV.
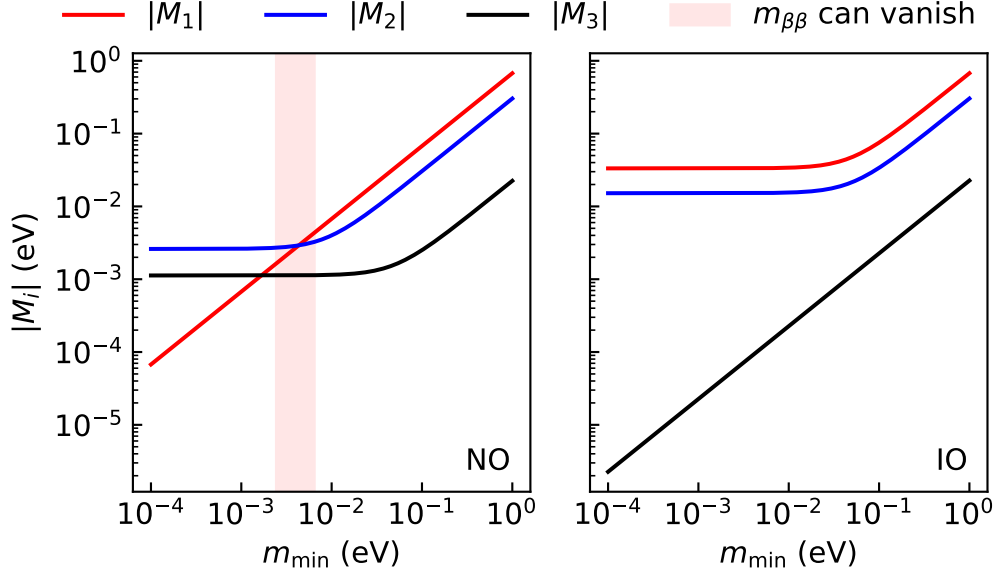

Figure 1.6: The absolute value of the complex effective masses M_i as defined in equation 1.23. The left figure shows the case for the normal ordering, and the right figure shows the inverted ordering case. The shaded region indicates where the complex effective masses may combine to give an effective Majorana mass $m_{\beta\beta}$ of zero.

1.7   EXPERIMENTAL SENSITIVITY TO $T_{1/2}^{0\nu}$

Experiments searching for $0\nu\beta\beta$ are comparable through their limits on $m_{\beta\beta}$. Individually, they constrain the half-life for that isotope, $T_{1/2}^{0\nu}$, which can be translated to constraints on $m_{\beta\beta}$ via equation 1.16.

The experimental sensitivity to $T_{1/2}^{0\nu}$ can be derived considering a simple counting experiment. The following derivation closely follows that set out in [61]. For an initial sample of N_0 $0\nu\beta\beta$ decaying nuclei, the number of $0\nu\beta\beta$ decays that occur in time t is given by

$$n_d = N_0 \left(1 - \exp\left(-\frac{\ln 2}{T_{1/2}^{0\nu}} t \right) \right) \simeq N_0 \frac{\ln 2}{T_{1/2}^{0\nu}} t, \qquad (1.24)$$

where the expansion is valid for $t \ll T_{1/2}^{0\nu}$. The observed number of decays is then given by folding in the experimental efficiency ϵ.
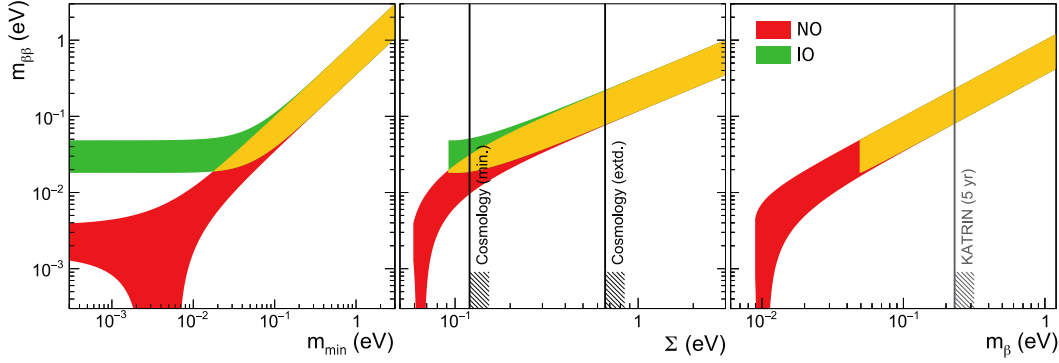
Figure 1.7: Allowed parameter space for $m_{\beta\beta}$, as a function of the mass of the lightest neutrino $m_{\min}$ (left), Σ (centre), and m_β (right). The region permitted in the case of normal ordering is shown in red, while the region permitted in the case of inverted ordering is shown in green. Where these regions overlap is shown in yellow, called the degenerate region. The centre figure shows limits on Σ from cosmology, while the right figure shows the expected sensitivity of the KATRIN experiment [65] to m_β after 5 years. The figure is adapted from [67].

If no signal is observed, the limit that can be set corresponds to the degree of fluctuations in the background that could 'hide' a signal, i.e. for a Poisson fluctuating background:

$$\sqrt{n_b} > \epsilon n_d, \tag{1.25}$$

which results in a sensitivity to the half-life $S^{0\nu}_{1/2}$ of

$$S^{0\nu}_{1/2} = \ln 2 \cdot \epsilon \frac{N_0 t}{\sqrt{n_b}}. \tag{1.26}$$

The number of $0\nu\beta\beta$ decaying nuclei N_0 can be expressed as $f_{\mathrm{enr}} N_A M / A$, where f_{enr} is the enrichment fraction, i.e. the fraction of the $0\nu\beta\beta$ decaying isotope in the sample, M is the mass of the sample, N_A is Avogadro's number, and A is the atomic mass of the isotope.

The number of background events can be expressed as

$$n_b = \mathrm{BI} \cdot Mt \cdot \Delta, \tag{1.27}$$

where BI is the so-called background index (events per mass per time per energy) and Δ is the energy resolution. The sensitivity is then given by

$$S^{0\nu}_{1/2} = \ln 2 \cdot \frac{\epsilon f_{\mathrm{enr}} N_A}{A} \sqrt{\frac{Mt}{BI \cdot \Delta}}. \tag{1.28}$$

Here the experimental sensitivity can be improved by either:

1. increasing the signal efficiency ϵ or enrichment fraction f_{enr},

2. increasing the sample mass M or observation time t,

3. reducing the background rate, or

4. improving the energy resolution.

Alternatively, consider a scenario where there is no background. In this case, the limit that can be placed is given by the maximum signal rate that is consistent at some confidence level with zero observed events. For Poisson statistics, the probability of observing zero events for an given expectation number of $0\nu\beta\beta$ decays ϵn_d is:

$$P = e^{-\epsilon n_d} > P_0, \tag{1.29}$$

where P_0 is some threshold defining a confidence level. Then

$$\epsilon n_d < -\ln P_0 = \text{const.} \tag{1.30}$$

The sensitivity is then proportional to:

$$S_{1/2}^{0\nu} \propto \epsilon f_{\text{enr}} \cdot Mt, \tag{1.31}$$

i.e. the sensitivity will increase approximately linearly with the acquired exposure (defined as Mt).

The 'background-free' condition can be defined by

$$\sqrt{n_b} < -\ln P_0, \tag{1.32}$$

because in this case the sensitivity is determined by Equation 1.30, instead of Equation 1.25. For $P_0 = e^{-1}$, the condition becomes

$$\text{BI} \cdot Mt \cdot \Delta < 1. \tag{1.33}$$

Therefore, the 'background-free' regime requires a low background index and high resolution, and will eventually be exited with increasing exposure, as shown in Figure 1.8.

1.8 SEARCHES FOR DOUBLE-BETA DECAY

As explained in Section 1.5, isotopes for which single-beta decay is forbidden are candidates for $0\nu\beta\beta$. Since the 1990s, various experiments have searched for $0\nu\beta\beta$ in a number of these isotopes [69–71].

As seen in Section 1.7, the best experimental sensitivity is obtained by maximising the target mass, enrichment fraction, observation time and signal efficiency, and minimising background rate and energy resolution. In general, a trade off is required among these criteria. For example, some elements have a naturally high isotopic fraction of the $0\nu\beta\beta$ candidate, such
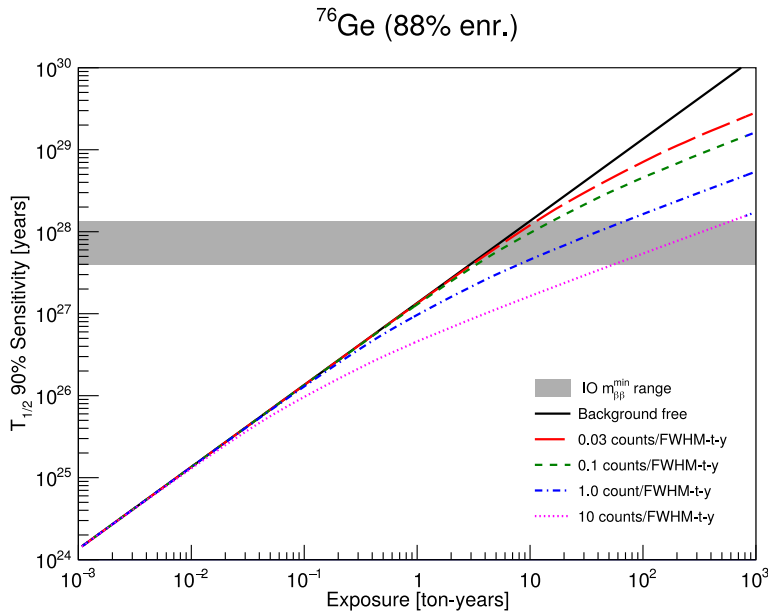
Figure 1.8: The sensitivity to $0\nu\beta\beta$ decay as a function of exposure and background. In this calculation, ϵf_{enr} is given by 60%. Figure adapted from [68].

as ^{130}Te, while other isotopes have a value of $Q_{\beta\beta}$ which is above the end-point of most natural radioactive gamma backgrounds, such as ^{48}Ca, ^{82}Se and others, and therefore have a reduced background rate around $Q_{\beta\beta}$. Different experimental approaches are used for various isotopes.

The next generation of $0\nu\beta\beta$ experiments will be ton scale experiments, seeking to reach the minimum of the allowed region in the $m_{\beta\beta}$ parameter space for the inverted mass ordering. This will require ton-scale experiments and half-life sensitivities up to 10^{28} years. Some recent and future experiments are highlighted below.

Large liquid scintillator detectors, such as KamLAND-Zen, using ^{136}Xe, and SNO+ [72], using ^{130}Te, are easily scalable with mass and thus can obtain large exposures. In 2016, KamLAND-Zen was the first experiment to set a $0\nu\beta\beta$ half-life limit of greater than 10^{26} years, corresponding to a Majorana mass limit of 61-165 meV, close to the inverted mass ordering region [73]. The upgrade to KamLAND2-Zen will improve the energy resolution from 4.6% to 2% and reduce the background by an order of magnitude [74]. The EXO-200 [75] experiment also uses ^{136}Xe, but in a Time Projection Chamber (TPC). nEXO is an upgrade of EXO-200 to be filled with 5 tons of xenon isotopically enriched at 90% [76]. The future DARWIN experiment has the main aim of searching for dark matter, but as a low-background TPC with more than 3.5 tons of ^{136}Xe, it can also be used to search for $0\nu\beta\beta$ decay [77]. The NEXT and PandaX experiments both aim to operate a TPC containing gaseous xenon, which would improve position reconstruction, and allow improved rejection of background events [78, 79].

The CUORE collaboration operates cryogenic bolometers to search for $0\nu\beta\beta$ [80]. These detectors benefit from a comparatively good energy resolution of 0.2% FWHM in their region of interest, allowing the rejection of $2\nu\beta\beta$ events. CUPID (CUORE Upgrade with Particle Identification) is a R&D project that will incorporate particle identification via the measurement of light signals generated through the Cherenkov effect or scintillation [81, 82].

Finally, there are the experiments using germanium semiconductor detectors, which exhibit the best energy resolution among $0\nu\beta\beta$ detectors, GERDA and MAJORANA [83]. Both experiments operated high-purity germanium detectors isotopically enriched in ^{76}Ge. The GERDA experiment, as the experiment under which the majority of this thesis was completed, is described in more detail in Chapter 2.

The success of the GERDA approach has inspired the formation of the LEGEND collaboration, formed of the GERDA and MAJORANA groups and other worldwide institutions, which aims to reach a sensitivity of 10^{28} years by operating 1 ton of enriched germanium detectors [84]. The LEGEND experiment is described in more detail in Chapter 4.

THE GERDA EXPERIMENT

The GERDA experiment searches for $0\nu\beta\beta$ decay of ^{76}Ge by operating high purity germanium diodes that have been isotopically enriched in ^{76}Ge up to $\sim 87\%$ [85]. For ^{76}Ge, $Q_{\beta\beta}$ is located at (2039.006 ± 0.050) keV [86]. The diodes therefore act simultaneously as both the source and detector of the decay, resulting in a high signal efficiency.

GERDA data taking began in 2011 with Phase I [87]. Phase II started in December 2015 after a substantial upgrade campaign [85]. Additionally, there was a minor upgrade in 2018 where new detectors were introduced [88]. Data taking was completed in November 2019.

This chapter provides an overview of the GERDA experiment and its search for $0\nu\beta\beta$ decay, and is structured as follows. Section 2.1 details the experimental setup of GERDA, while Section 2.2 describes the use of semiconductors as particle detectors, and the GERDA detectors in particular. Section 2.3 presents the $0\nu\beta\beta$ decay search analysis, with details on event digitisation and selection, and the statistical analysis to produce the constraint on the half-life.

2.1 EXPERIMENTAL SETUP

The GERDA experiment is located underground at the Laboratori Nazionali del Gran Sasso (LNGS) in central Italy [89]. The rock overburden of 1400 m (3500 m water equivalent) reduces the cosmic muon flux by six orders of magnitude to $(3.41 \pm 0.01) \cdot 10^{-4}$ m^{-2} s^{-1} [90].

The experimental setup is shown in Fig. 2.1. In order to reach the stringent low background requirements of GERDA an extensive screening campaign was conducted to select low-background materials, and the multiple layers passively and actively shield the germanium detectors.

Firstly, a 10 m diameter water tank surrounds the experiment, shielding from external γ and neutron radiation. Above the water tank is a clean room with a glove box and lock, used for the assembly of and accessing the experiment. The water tank is instrumented with photomultiplier tubes (PMTs) which detect Cherenkov light caused by residual cosmic muons. Additional plastic scintillator panels on top of the clean room detect muons passing through with a high incident angle.

Inside the water tank is a 4.2 m diameter cryostat, containing 64 m^3 high-purity liquid argon (LAr), which acts as a coolant and as background shielding. The cryostat is lined with 6 cm thick radiopure copper to reduce primarily γ ray emission from the stainless steel cryostat.
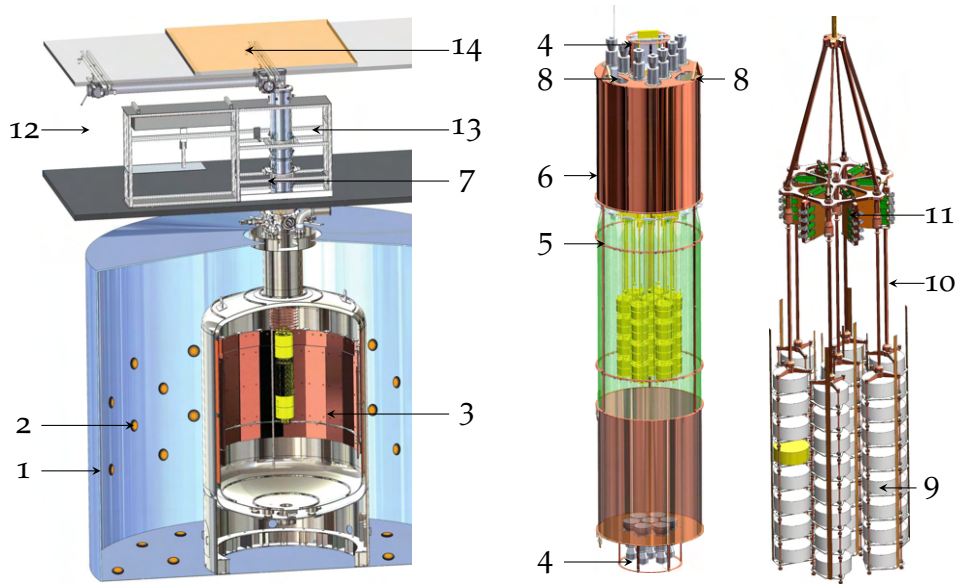
Figure 2.1: The GERDA experiment. The outermost layer is a water tank (1) instrumented with PMTs (2) as a Cherenkov cosmic muon veto. Inside is the liquid argon (LAr) cryostat (3), instrumented with photosensors (4), the optical fibre curtain (5) and the copper shroud (6). The calibration sources are lowered down alongside the detector array from the lock (7) through access points (8). Individual detectors (9) are mounted in strings, forming an array. Signal cables (10) lead from the detectors to pre-amplifiers (11). Above is the clean room (12), containing the cryostat lock (7) and glove box (13) for access, topped with an additional muon veto of plastic scintillator panels (14). Figure adapted from [91].

The germanium detectors are arranged in vertical columns, referred to as strings, forming an array, in the centre of the cryostat, contained in low-activity silicon holders. Each detector string is enclosed by a transparent nylon cylinder, known as a 'mini-shroud', which mitigates the drift of ^{42}K ions towards the detectors, caused by their high voltages supplies, a potential source of background [85].

As part of the Phase II upgrade, the liquid argon was instrumented with photosensors for the detection of the scintillation light stimulated by energy deposits in the liquid argon by background events. The photosensors consist of 16 3″ photomultiplier tubes (PMTs, R11065-20 type, produced by Hamamatsu) arranged above and below the array, and silicon photomultipliers (SiPMs) above the array. The SiPMs (PM33100 type, produced by KETEK [92]) are coupled to a curtain of wavelength shifting (WLS) fibres (BCF-91A type, produced by Saint-Gobain Crystals [92]) that surround the array, which are coated with tetraphenyl-butadiene (TPB), a wavelength shifting material, that shifts the wavelength of the scintillation light to better match the absorption spectrum of the WLS fibres, which then transmit the light to the photosensors [93, 94]. LAr is only semi-transparent to its

own scintillation light at 128 nm, but transparent to the blue light emitted by TPB. Additionally, copper shrouds located above and below the fibre curtain are lined with TPB [95] coated Tetratex [96] to effectively shift and reflect light towards the WLS fibres and photosensors. The nylon mini-shrouds surrounding the germanium detectors are also coated with TPB.

2.2 GERMANIUM DETECTORS

2.2.1 *Semiconductor detectors*

Materials are classified according to their conductivity into three types: conductors, semiconductors and insulators. The conductivity of a material is determined by their electronic band structure, that is, the range of energies that electrons may take in that material. Since electrons are fermions, the Pauli Exclusion Principle requires that no two electrons may have the same state. In a material's ground state, the electrons will thus fill up the lowest energy bands first, until reaching the Fermi level, E_F, as pictured in Figure 2.2.
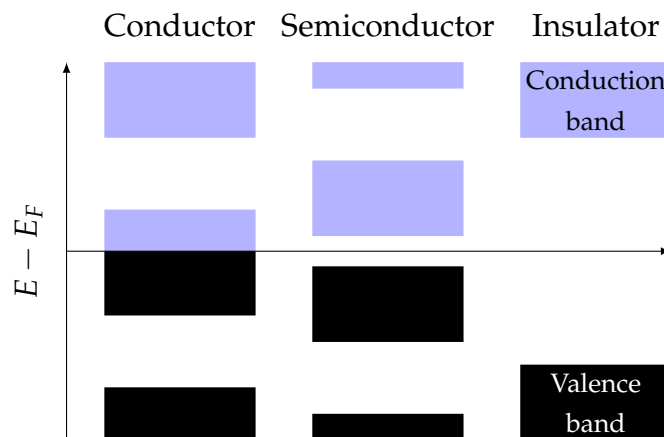

Figure 2.2: Schematic band structure of conductors (left), semiconductors (centre) and insulators (right). In a band, black indicates filled states and blue indicates vacant states.

When a voltage is applied to a material, whether a current can flow depends on whether the electrons in the material are able to absorb energy from an electric field by moving to different states. In a conductor, the Fermi level lies within a band (the conduction band), and the highest energy electrons are therefore free to move. In an insulator, the Fermi level lies between bands, and for any electron to move would require overcoming the energy gap between the top filled band (valence band) and the next (conduction band). The band structure of semiconductor is similar to that of the insulator, except that the band gap is on the order of the energy of the thermal excitations.
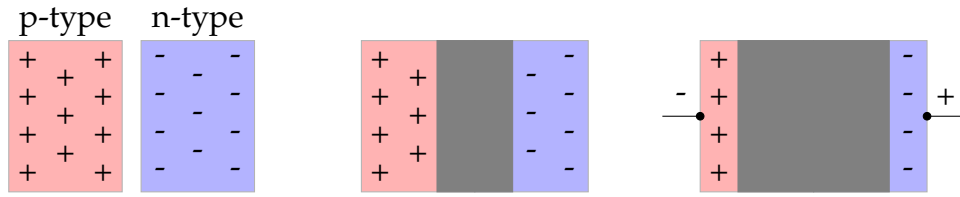
p-type   n-type

Figure 2.3: Formation of a depletion region in a diode. A p-type semiconductor has an excess of holes, in the valence band, while an n-type semiconductor has an excess of electrons in the conduction band (left). Placing the two together will cause the free electrons to drift towards the p-type conduction band, and vice versa. The recombination of electrons and holes will result in a region with no charge carriers, the depletion region (centre). Applying a voltage across the diode will increase the size of the depletion region (right). Adapted from [55].

If a semiconductor is cooled, the current due to thermal excitations is suppressed. Semiconductors can thus be exploited as particle detectors, because ionising radiation will excite electrons to the conduction band, allowing a current to flow. The absence of an electron in the otherwise full valence band is known as a hole, and can also act as a positively charged particle moving under the influence of an applied electric field.

It is difficult to entirely avoid the presence of impurities during the germanium crystal growing process. Impurities will donate an excess of either electrons or holes, which will allow current to flow when an electric field is applied, behaviour which is undesirable in a semiconducting particle detector. However, doped materials, into which impurities have intentionally been introduced, can be combined to create regions where no free charge carriers remain, see Figure 2.3. This depletion region forms the region of the detector sensitive to interactions. The size of the depletion region can be increased by the application of an electric voltage between the two regions.

The electric field will then cause electrons and holes produced by an interaction to drift. According to the Shockley-Ramo theorem [97,98], they will thus induce a current on the readout electrode:

$$I_{\text{readout}}(t) = - \int \nabla \Phi_{\text{weighting}} \cdot \mathbf{v}_{\text{drift}}(t) \, \mathrm{d}q, \tag{2.1}$$

where the integral runs over all the charge carriers q (electrons and holes), $\mathbf{v}_{\text{drift}}$ is their instantaneous velocity and $\Phi_{\text{weighting}}$ is the so-called weighting potential at the position of q. This weighting potential is the electric potential divided by $1\,\text{V}$ at the position of the charge when the readout electrode is at unit potential, all other electrodes are at zero potential and all other charge carriers are removed.

2.2.2   *The* GERDA *detectors*

Between the start of Phase II in December 2015 and the upgrade in 2018, GERDA operated two types of detectors: 10 Coaxial and 30 Broad Energy Germanium (BEGe). Three of the Coaxial detectors have a natural abundance, while the other detectors are enriched in ^{76}Ge to $\simeq$ 87%. During the upgrade of 2018, five Inverted Coaxial Point Contact (IC) detectors, of one detector, were installed, replacing all the non-enriched and one enriched Coaxial detector. Photos of the detectors and schematics are shown in Figure 2.5.
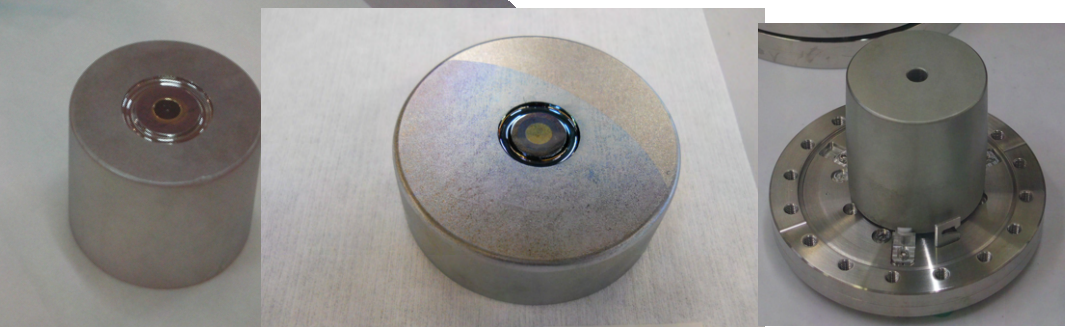

Figure 2.4: Photos of a Coaxial (left), BEGe (centre) and IC (right) detector. Not to scale.
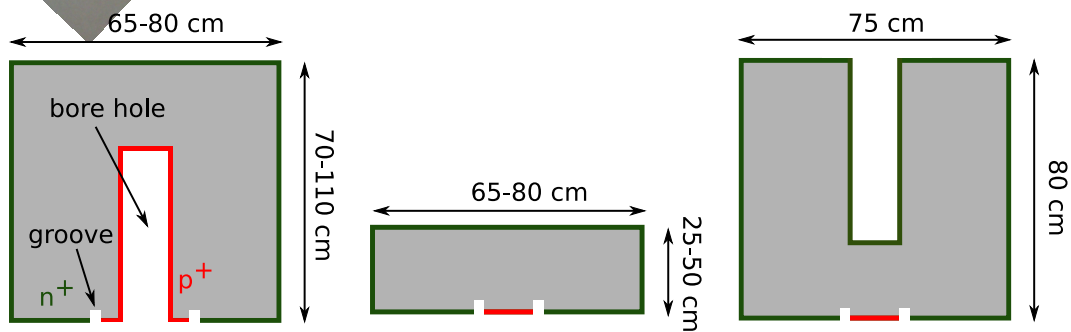

Figure 2.5: Schematic cross-section and indicated dimensions of Coaxial (left), BEGe (centre) and IC (right) detectors. The electrons and holes created due to particles interaction drift to n+ (shown in green) and p+ (shown in red) electrodes, respectively.

All these detectors are read out via their grounded p contact, while the depletion voltage is applied to the n contact. The p contact is formed by the implantation of boron atoms via an ion beam, with a thickness of $\mathcal{O}(10)$ nm. The n contact is formed by the thermal diffusion of lithium atoms, and has a thickness of $\mathcal{O}(1)$ mm. Charge carriers produced in this region are not effectively collected on the readout electrode, so this region is known as the dead-layer. This region, though reducing the active region of the material

and thus the signal efficiency to $0\nu\beta\beta$, shields the detector from surface contaminants such as α particles. A groove separates the two electrodes.

The Coaxial detectors are larger and were inherited from previous ^{76}Ge $0\nu\beta\beta$ experiments, Heidelberg-Moscow and IGEX [70, 71, 99], with a total enriched mass of 15.6 kg. They have a cylindrical shape with a height of 70-110 mm, with an internal borehole that forms a large p contact.

The BEGe detectors were developed for GERDA [100]. Though smaller, these detectors do not have a borehole, and their p contact is instead a $\mathcal{O}(1)\,\mathrm{cm}^2$ point on one side. The electric field is thus concentrated close to the p contact, such that most of the signal is caused by the holes moving in this region (see Equation 2.1). The shape of the signal is therefore relatively independent of the interaction point. The resulting dependence of the signal shape on the interaction type can be exploited to reject background events such as those caused by multiple interactions in the detector volume, or α events. The BEGe detectors also benefit from a superior energy resolution relative to the Coaxial detectors, due to their smaller electronic capacitance and therefore larger signal-to-noise ratio [55, 101] (see Section 3.1.1).

The IC detectors combine the larger size of the Coaxial detectors with the similar pulse shape and energy resolution properties of the BEGe detectors [102, 103]. Though they have a similar shape as the Coaxial detectors, their p contact is not on the borehole, but is instead a point contact on the closed surface of the crystal. Larger detectors allow a greater mass per detector channel, thus reducing complexity and auxiliary material that must be introduced to the cryostat for a given total mass of ^{76}Ge.

2.3 DATA ANALYSIS AND PHYSICS RESULTS

2.3.1 *Event digitisation*

The electronics chain for the read out of the signal from the germanium detectors consists of the Very Front End section (VFE) integrated into the detector holders, and the Charge Sensitive Preamplifier (CSP) located approximately 1 m above the array [104]. This separation avoids radioactive components close to the detectors while minimising noise contributions to the signal. A feedback loop returns the input voltage to its baseline value. A resulting signal shape is shown in Figure 2.6.

To monitor the stability of the electronics chain, a test pulse of fixed amplitude is injected every 20 s into each of the preamplifiers.

The signals are digitised by a Flash Analogue to Digital Converter (FADC) in the clean room. These are saved as Majorana-Gerda Data Objects (MGDO) inside ROOT files [105], forming the so-called tier1 data type of GERDA. Additionally, the signals from the LAr veto photosensors and the muon veto
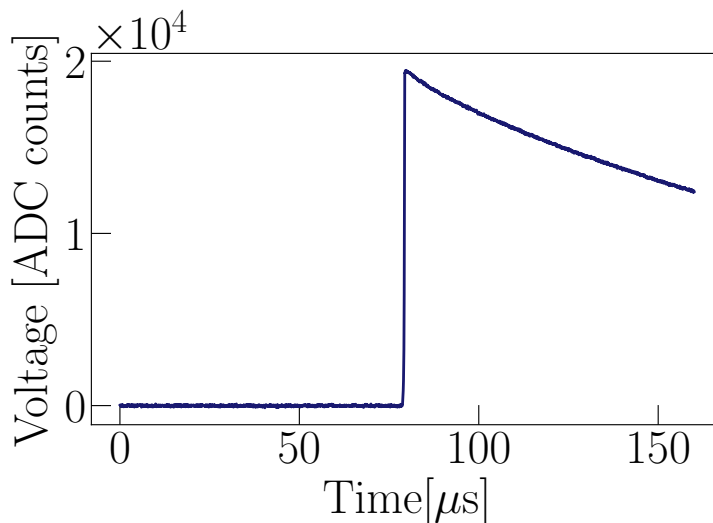
Figure 2.6: A typical digitised waveform after baseline subtraction. Taken from [56].

are recorded and synchronised to those of the germanium detectors. For more information, see [87, 93]

Dedicated calibration runs and analyses are used to extract energy observables for each detector in an event. This is described in detail in Chapter 3.

2.3.2   *Event selection*

To optimise the sensitivity to $0\nu\beta\beta$ signal events, events consistent with other topologies (see Figure 2.7) and characteristics are rejected. Only data taken during stable operating conditions are used for physics analysis, which is about 80% of the total.

Quality cuts reject events not consistent with a physical energy deposition. This includes flat and featureless waveforms consistent with only the baseline, events that saturate the dynamic range of the FADC, and pile-up events. These cuts reject $\simeq 100\%$ of non-physical events, while maintaining a signal efficiency of greater than 99.9%. More details are given in [106].

The shape of the collected waveform varies depending on the topology of the event interaction. For example, events with multiple energy deposits in a detector (so called multi-site events, or MSE) will differ from those with only localised energy deposits (single-site events, or SSE), shown schematically in Figure 2.7. Similarly, events that place close to either of the two electrodes will exhibit either fast or slow charge collection respectively. This is shown in Figure 2.8. The exploitation of the time structure of the signals is called Pulse Shape Discrimination (PSD).

For the BEGe and IC detectors, PSD takes the form of a cut based on a single parameter, A/E, where A is the maximum current amplitude and
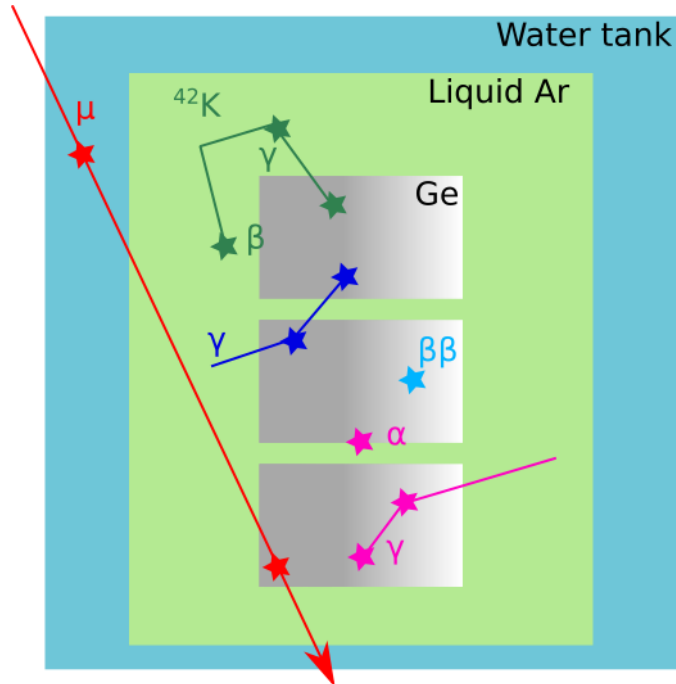
Figure 2.7: Schematic of possible event topologies in GERDA. $0\nu\beta\beta$ decay events will deposit energy only in $\sim 1\,\text{mm}^3$ of a single detector (light blue). Events depositing energy in multiple locations in a detector, or on the surface can be rejected by pulse shape discrimination (PSD) techniques, see text (magenta). Events that trigger the LAr veto and deposit energy in a germanium detector are also rejected (green), for example decays of ^{42}K. Cosmic muons events depositing energy in a germanium detector and either the water tank or plastic scintillation panels can be rejected by the muon veto (red). Events that deposit energy in multiple detectors are rejected by the detector anti-coincidence (AC) cut (dark blue).
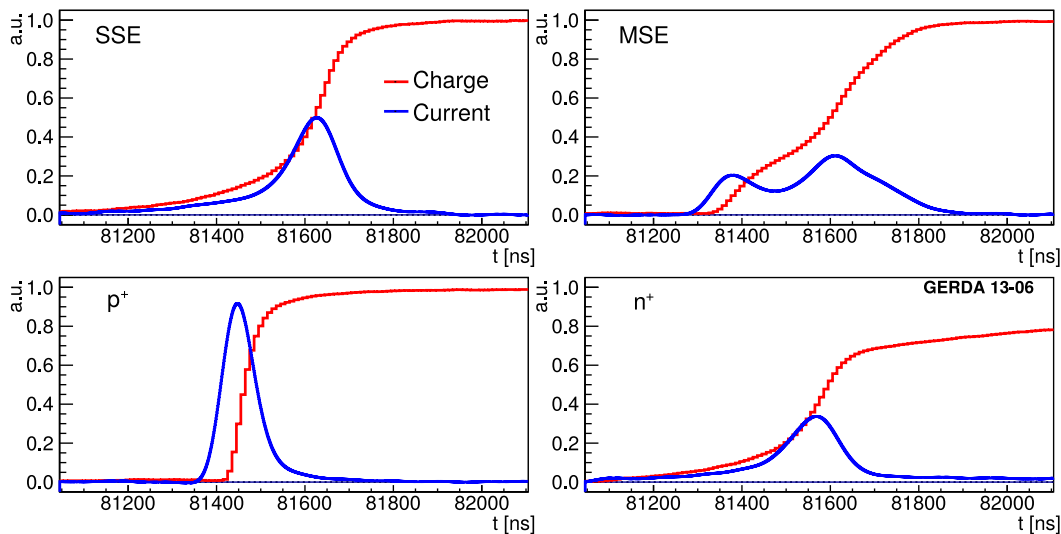
Figure 2.8: Example signals in a BEGe detector for a single-site event (top left), a multi-site event (top right), an event close to the p contact (bottom left) and a surface event on the n contact (bottom right). Figure from [107].

		PSD efficiency
Before upgrade	Coaxial	$(69.1 \pm 5.6)\%$
	BEGe	$(88.2 \pm 3.4)\%$
After upgrade	Coaxial	$(68.8 \pm 4.1)\%$
	BEGe	$(89.0 \pm 4.1)\%$
	IC	$(90.0 \pm 1.8)\%$

Table 2.1: Combined pulse shape discrimination efficiency for $0\nu\beta\beta$ decay events for different detector types and before/after the upgrade.

E is the energy of the event, determined from the maximum of the filtered waveform (see Section 3.1.2). For the Coaxial detectors, where the electric field more strongly varies across the detector volume, an artificial neutral network (ANN) is used to discriminate between SSEs and MSEs. In addition, a cut on the signal rise time rejects events on the p contact of the Coaxial detectors. Finally, for all detectors, to fully reject events with slow or incomplete charge collection, a cut based on the difference between two energy estimators, derived from the same digital filter using different shaping times, is employed. The combined signal efficiency for all PSD techniques is given in Table 2.1.

Events within $10\,\mu s$ of a trigger from the muon veto system are discarded. Similarly, events where a photosensor of the LAr veto system measures a signal greater than one photoelectron within $6\,\mu s$ are also rejected. The dead time due to the muon veto is less than 0.01%, and for the LAr veto are $(2.3 \pm 0.1)\%/(1.8 \pm 0.1)\%$ before/after the upgrade.

Finally, highly ionising radiation such as high energy γs that deposit energy in multiple detectors are rejected by the detector anti-coincidence cut.

2.3.3 *Phase II energy spectrum and backgrounds*

The Phase II data collected by GERDA between December 2015 and November 2019 corresponds to an exposure of 103.7 kg yr. Additionally, prior to GERDA Phase II, Phase I had an exposure of 23.5 kg yr.

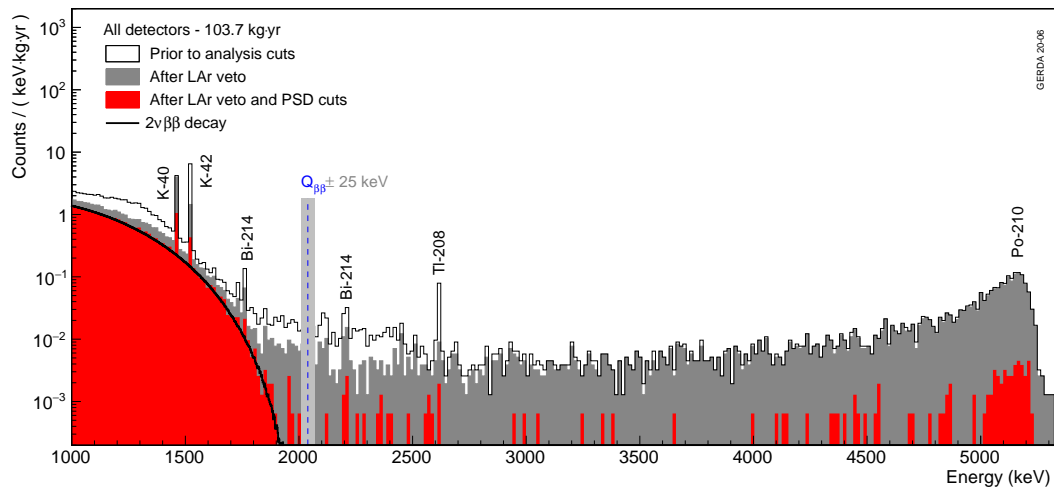The full Phase II energy spectrum before and after cuts is shown in Figure 2.9.

Figure 2.9: Combined energy spectrum for Phase II, before and after the LAr veto and PSD cuts. The blue dashed line shows the position of $Q_{\beta\beta}$. The black solid line shows the expected spectrum of $2\nu\beta\beta$ events with a half-life as measured in [108]. Prominent γ lines are shown, as well as the α peak at high energies. More information about GERDA Phase II pre upgrade background data and modelling can be found in [109].

The lower energy region is dominated by $2\nu\beta\beta$ events, for which GERDA Phase I measured a half-life of $(1.926 \pm 0.094) \cdot 10^{21}$ yr [108].

The two strongest γ lines are those at 1461 keV due to ^{40}K and 1525 keV due to ^{42}K in the LAr. The decay of ^{42}K is a cascade of a β and γ. The emitted β particle deposits energy in the LAr and thus the corresponding decay can be detected by the LAr veto system. The intensity of the ^{42}K line is therefore suppressed by the LAr veto by about a factor of five. Conversely, the decay of ^{40}K is an electron-capture event, so no additional particle can deposit energy in the LAr, and the LAr veto cannot suppress this line. The suppression of the two potassium lines is shown in Figure 2.10.

Additional weak γ lines due to the decay of ^{214}Bi and ^{208}Tl contaminants are labelled in Figure 2.9. The energy region above 3 MeV is dominated
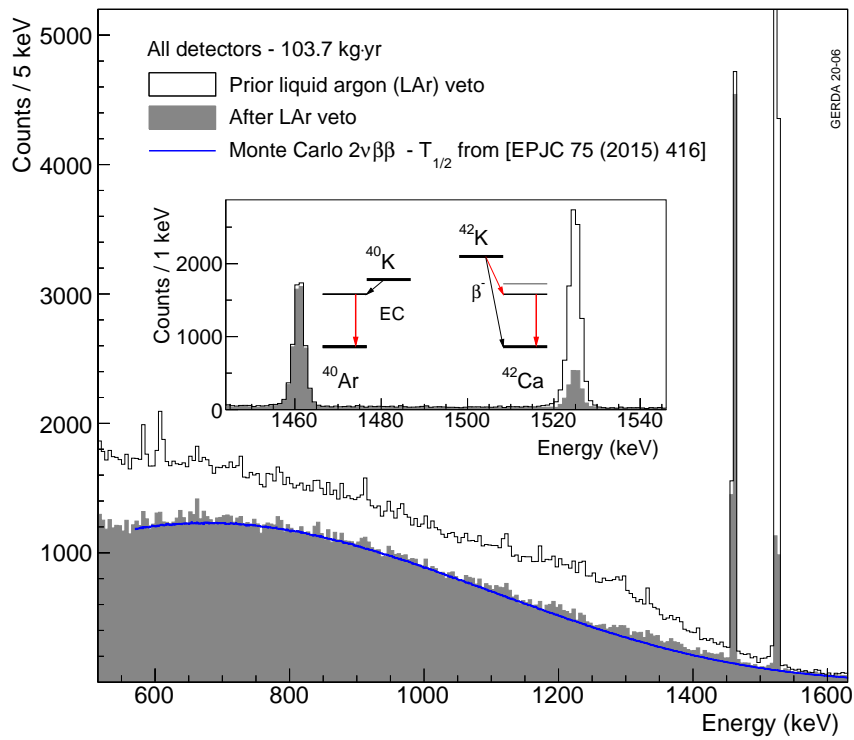
Figure 2.10: The γ lines in the background spectrum due to ^{40}K and ^{42}K. The ^{42}K line is suppressed by the LAr veto due to the emitted β particle, while the ^{40}K decay takes place via electron capture and therefore cannot be suppressed.

by α events due to the decay of ^{210}Po on the p contact of the detectors. Detailed background modelling was performed for Phase II data taken between December 2015 and April 2018 [109]. Figure 2.11 shows the individual contributions to the background around $Q_{\beta\beta}$. Approximately equal contributions to the backround index are seen from α particles with degraded energy, decays from isotopes in the ^{232}Th and ^{238}U chains, and ^{42}K decays.
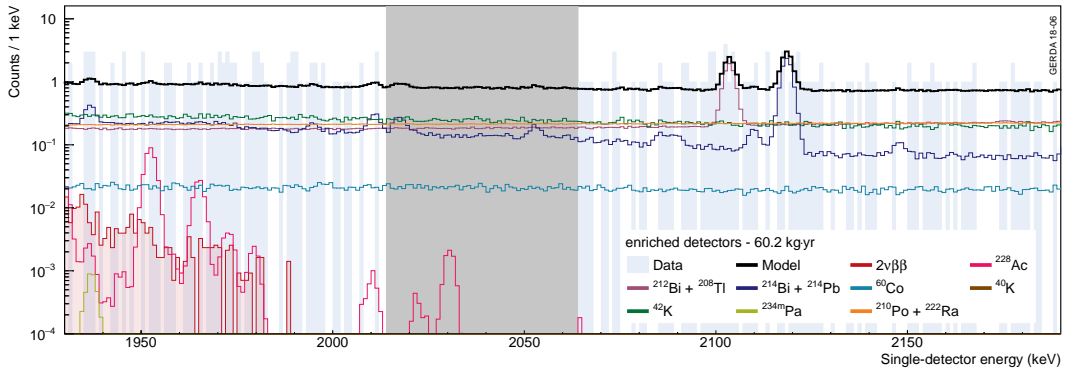

Figure 2.11: Background model around $Q_{\beta\beta}$.

2.3.4   *Statistical analysis*

The energy range fitted for the $0\nu\beta\beta$ analysis is between 1930 keV and 2190 keV excluding ±5 keV regions around the two expected γ lines at 2104 keV and 2119 keV due to the decay of ^{208}Tl and ^{214}Bi, respectively.

Previous GERDA $0\nu\beta\beta$ analyses have been reported in [67,91,110–112]. To avoid possible bias, events with energy $Q_{\beta\beta}\pm25$ keV are not analysed until the $0\nu\beta\beta$ analysis and cuts are finalised, a so-called 'blinded' analysis.

The data is divided into 408 partitions, labelled by k, i.e., data coming from each detector divided into stable periods of time during which parameters such as the efficiencies and energy resolution are stable in all detectors. In the fit, the signal strength parametrising the half-life and the background index are common parameters to all partitions, with the exception of the Phase I data sets, which are introduced as separate partitions with differing background indices.

The fit model consists of a Gaussian distribution centred at $Q_{\beta\beta}$, with the width of the energy resolution $\sigma_k = $ FWHM/2.35, and a flat distribution for the background.

The number of signal events $\mu_{s,k}$ is given by

$$\mu_{s,k} = \frac{\ln 2 \mathcal{N}_A}{T_{1/2} m_{76}} \varepsilon_k \mathcal{E}_k, \tag{2.2}$$

where $\mathcal{N}_A$ is Avogadro's number, m_{76} is the molar mass of ^{76}Ge, and $\mathcal{E}_k$ and ε_k are the exposure and $0\nu\beta\beta$ decay detection efficiency respectively of the k-th partition. The number of background events is given by

$$\mu_{b,k} = B \times \Delta E \times \mathcal{E}_k, \tag{2.3}$$

where ΔE is the net width of the analysis window and B is the background index. The likelihood function is then given by

$$\mathcal{L} = \prod_k \left[\frac{(\mu_{s,k} + \mu_{b,k})^{N_k} e^{-(\mu_{s,k}+\mu_{b,k})}}{N_k!} \times \right.$$
$$\left. \prod_{i=1}^{N_k} \frac{1}{\mu_{s,k} + \mu_{b,k}} \times \left(\frac{\mu_{b,k}}{\Delta E} + \frac{\mu_{s,k}}{\sqrt{2\pi}\sigma_k} e^{-\frac{(E_i - Q_{\beta\beta})^2}{2\sigma_k^2}} \right) \right] \tag{2.4}$$

where E_i labels the energy of the N_k events in the k-th partition.

An unbinned fit is performed in both frequentist and Bayesian frameworks, with the Frequentist fit shown in Figure 2.12. Systematic uncertainties on the limit are computed by repeating the fits, each time varying the input parameters according to their uncertainties, and are on the percent level.

Under the frequentist analysis, the best fit for the number of signal events is zero, and the lower half-life limit is given by

$$T_{1/2}^{0\nu\beta\beta} > 1.8 \cdot 10^{26} \text{ yr at 90\% C.L.,} \tag{2.5}$$
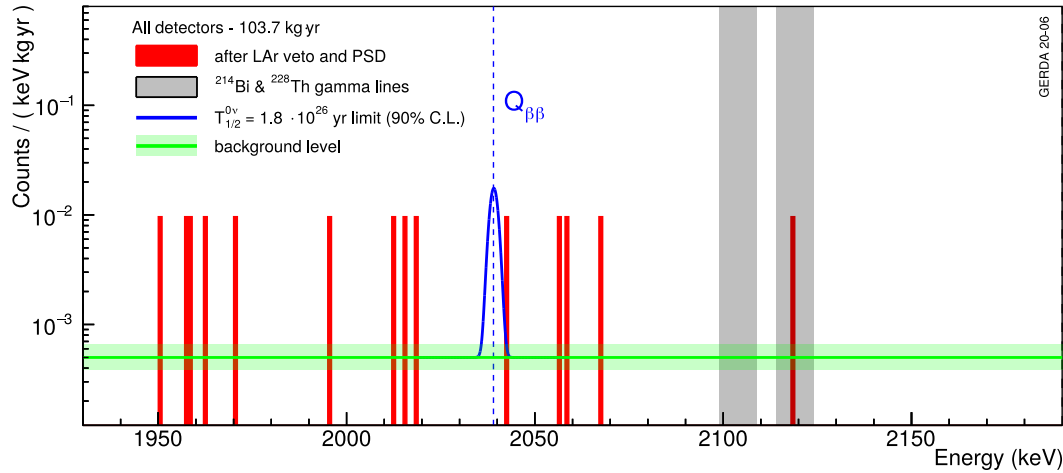

Figure 2.12: Combined energy spectrum of GERDA Phase II after unblinding and analysis cuts in the fitting window. The grey areas indicate regions in which γ lines are expected. The best fit for the background index and its 68% C.L. interval are shown by the green line and band respectively. The blue line shows the function corresponding to the hypothetical $0\nu\beta\beta$ decay signal with a half-life given by the 90% C.L. Frequentist lower limit.

with a derived Phase II background index of

$$B = 5.2^{+1.6}_{-1.3} \cdot 10^{-4} \, \text{counts}/(\text{keV kg yr}). \qquad (2.6)$$

This is the lowest background index achieved for any $0\nu\beta\beta$ experiment, and means that GERDA has succeeded in its aim to remain in the background-free regime for all of Phase II [88].

For a constant prior in $1/T^{0\nu\beta\beta}_{1/2}$ between 0 and $10^{-24} \, \text{yr}^{-1}$, the Bayesian analysis results in a lower limit of $T^{0\nu\beta\beta}_{1/2} > 1.4 \cdot 10^{26} \, \text{yr}$ at 90% C.I.

The limit on $T^{0\nu\beta\beta}_{1/2}$ can be converted into a limit on $m_{\beta\beta}$ using Eq. 1.16. For the set of nuclear matrix elements from [113–123], a limit of

$$m_{\beta\beta} < (79 - 180) \, \text{meV} \qquad (2.7)$$

is obtained, which is competitive with limits obtained with other isotopes [73, 75, 124].

GERDA has successfully demonstrated the technique of operating germanium detectors in liquid argon, and instrumenting that liquid argon as a veto, paving the way for the next generation of ^{76}Ge experiments.

In addition to the $0\nu\beta\beta$ analysis, the excellent energy resolution and low background have enabled GERDA to make a number of other physics analyses, including a search for bosonic superweakly interacting dark matter [125] and a search for decays of ^{76}Ge to excited states of ^{76}Se [126].

ENERGY CALIBRATION FOR GERDA PHASE II

A key part of all GERDA analyses is the energy determination of events. As the signature of $0\nu\beta\beta$ decay in germanium detectors is a sharp peak at the known energy of 2039 keV, the energy calibration is an essential ingredient in the search for this decay. The better the energy resolution of the detectors, the smaller the effective region of interest, and the more clearly identifiable a peak-like excess over the continuous background is.

Importantly, the energy is in fact the only way by which $2\nu\beta\beta$ decays can be distinguished from $0\nu\beta\beta$ decays, as shown in Figure 3.1. The fraction F of the $2\nu\beta\beta$ events occuring within one resolution of $Q_{\beta\beta}$ can be approximated by [127]

$$F \simeq \frac{7Q_{\beta\beta}\delta^6}{m_e}, \tag{3.1}$$

where $\delta = \Delta E/Q_{\beta\beta}$ is the fractional energy resolution. For a resolution given by 0.1% of $Q_{\beta\beta}$, similar to GERDA, the probability for a $2\nu\beta\beta$ event to fall within 3σ of $Q_{\beta\beta}$ is only $\sim 10^{-14}$, compared to 0.011 for a resolution of 10% of $Q_{\beta\beta}$.
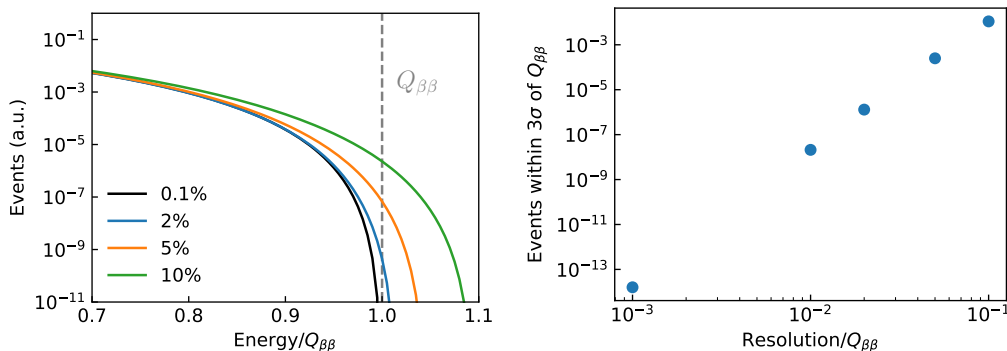

Figure 3.1: A worsening resolution leads to more $2\nu\beta\beta$ events being reconstructed at an energy above $Q_{\beta\beta}$: (left) the $2\nu\beta\beta$ spectrum near the endpoint at $Q_{\beta\beta}$ for a number of energy resolutions, given as fractions of $Q_{\beta\beta}$; (right) the fraction of $2\nu\beta\beta$ events reconstructed within 3σ of $Q_{\beta\beta}$ follows an approximate power law relative to the energy resolution, as in Eq. 3.1.

The main goals of the calibration analysis are to define and maintain a stable energy scale over the years of data taking, and determine the resolution of the detectors. It is necessary to identify the right peak region (and reject all background events with different energy), combine data from different detectors over extended periods of time, and efficiently exploit the excellent energy resolution of germanium detectors.

This chapter describes how the germanium detectors are calibrated and this data was analysed for GERDA Phase II, and is structured as follows. The remainder of this introduction details the theory behind the energy dependence of the resolution of germanium detectors, and how an estimate for the energy of an event is formed. Section 3.2 describes the procedure for taking calibration data. In Section 3.3 the method for determining of the energy scale is detailed. The stability of the energy scale and resolution is presented in Section 3.4. Section 3.5 presents the combined calibration analysis that partitions the data and calculates the energy resolution at $Q_{\beta\beta}$ for the $0\nu\beta\beta$ analysis, along with a study of systematic uncertainties. Section 3.7 describes the calculations of and correction of residual energy biases close to $Q_{\beta\beta}$. The last section of the chapter, Section 3.8, presents a comparison of the conclusions of the calibration data with GERDA background data.

3.1   INTRODUCTION

3.1.1   *Origin of energy resolution*

The width of the peaks in the energy spectrum is the result of a number of sources of uncertainty between the emission of the γ ray and its detection. The resolution is usually expressed as the Full Width of the peak at Half Maximum height:

$$\text{FWHM} = 2.355\omega, \tag{3.2}$$

where the total variance, ω, can be expressed as [128]

$$\omega^2 = \omega_I^2 + \omega_P^2 + \omega_C^2 + \omega_E^2. \tag{3.3}$$

Here, ω_I is the uncertainty on the energy of the γ ray emitted by the decaying nucleus, ω_P is the variance in the produced number of electron-hole pairs, ω_C is the variance in the fraction of charge collected by the detector, and ω_E is the result of electronic noise.

Of these contributions, ω_I is the smallest. According to the Heisenberg uncertainty principle, it can be expressed as

$$\omega_I = \frac{\hbar}{2.355\tau} \tag{3.4}$$

where τ is the lifetime of the excited state emitting the γ ray. For a typical lifetime on the order of 10^{-12} s, this contribution is $<10^{-3}$ eV, i.e. negligible.

As for ω_P, the number of electron-hole pairs produced will depend on the energy deposited in the crystal. At 77 K, the average energy required to produce an electron-hole pair, ϵ, is 2.96 eV. Thus for an energy deposit of E, the average number of electron-hole pairs produced will be $n = E/\epsilon$. If the production of electron-hole pairs was a purely Poisson process, the

variance in the number of pairs would be $\Delta n = \sqrt{n}$. However, since consecutive ionisations are not independent processes, an additional factor, the Fano factor F, must be included, such that $\Delta n = \sqrt{Fn}$ [129]. Theoretical values for the Fano factor in germanium are around 0.13 [130], while measurements put the value between 0.05 and 0.12 [131, 132]. ω_P can then be expressed as

$$\omega_P = \epsilon \Delta n = \sqrt{FE\epsilon}. \tag{3.5}$$

Incomplete collection of the charge carriers produced in an event in a detector can generate low-energy tails. This can be caused by charge trapping in the crystal due to impurities, or by a preamplifier time constant that is quicker than the rise time of the germanium signal, or shaping filter time (see Section 3.1.2). Empirically, ω_C is given by

$$\omega_C = dE, \tag{3.6}$$

where d is a proportionality constant.

The final component is electronic noise, ω_E, which itself can be divided into three components

$$\omega_E^2 = \omega_{\text{parallel}}^2 + \omega_{\text{series}}^2 + \omega_{\text{flicker}}^2, \tag{3.7}$$

called parallel, series, and flicker noise respectively.

The parallel component is associated with a current flowing in the feedback circuit of the preamplifier, which may be due to thermal noise in the feedback resistor or leakage current in the detector itself. It can be expressed as

$$\omega_{\text{parallel}} \propto \left(I_D + \frac{2kT}{R_f} \right) \tau_S, \tag{3.8}$$

where I_D is the current, T is the temperature of the resistor and τ_S is the shaping time of the preamplifier.

The series component is associated mainly with the capacitance of the detector and the detector-preamplifier connection. It can be expressed as

$$\omega_{\text{series}} \propto C^2 \left(\frac{2kT}{g_m \tau_S} \right), \tag{3.9}$$

where C is the total readout capacitance, T is the preamplifier temperature and g_m is the transconductance of the preamplifiers, or its gain, given by current in divided by voltage out.

The optimal shaping time, τ_S, is chosen to minimise the combination of the parallel and series noise.

Finally, the flicker noise or $1/f$ noise is associated with the variation in the direct current of the circuit. It is the smallest of the three electronic components.

The energy dependence of the resolution can be found by combining all these components as in 3.3.

$$\text{FWHM} = 2.355\sqrt{\omega_E^2 + F\epsilon E + d^2 E^2}, \tag{3.10}$$

$$= 2.355\sqrt{a + bE + cE^2}, \tag{3.11}$$

where here the ω_I component has been neglected. The charge collection term c is often also neglected (see Section 3.6.3). This expression implies that $b = F\epsilon \sim 10^{-4}$ keV, and should be the same for all detectors.

3.1.2 *Energy estimators*

In order to extract an estimator for the energy deposited in a detector, the waveforms are first shaped with dedicated filters, which minimise the contribution of electronic noise. The two shaping filters used in higher level data analysis are the pseudo-Gaussian filter and the ZAC (Zero Area Cusp) filter. An estimator for the deposited energy in the detector is then given in both cases by the maximum of the filtered waveform.

The Gaussian, or pseudo-Gaussian, filter is implemented as a sequence of operations on the waveform, as shown in Figure 3.2. First, a delayed differentiation with a time constant of 5 μs is applied, that is, the difference in amplitude is evaluated between sampling points separated by 5 μs. Then, a 10 μs moving average window is applied 25 times. The resulting filtered waveform is quasi-Gaussian shaped, whose height is then extracted to be used as an energy estimator, "the Gauss energy". These operations reduce the contribution of high-frequency noise contained within a waveform to the energy estimator. Since the parameters of this filter do not require any optimisation, this energy estimator is used for the online monitoring of the data.

The ZAC filter is a 2-sided sinh-curve connected by a flat top, such that its total area is zero, shown in Figure 3.3. The waveform is convoluted with the combination of the inverse preamplifier response function and the ZAC filter. Again, the height of the resulting waveform is used as an energy estimator, "the ZAC energy". To maximise its performance, the parameters of the filter, such as the flat top length, are optimised for each detector and each calibration run to minimise the resolution of the 2.6 MeV peak in the calibration spectrum, requiring additional offline processing. Uncalibrated ZAC energy estimators and thus the resulting calibration curves of any two calibrations are generally not comparable. However, an improvement in the energy resolution of ∼0.3 keV relative to the Gauss energy can be achieved with this method [133].
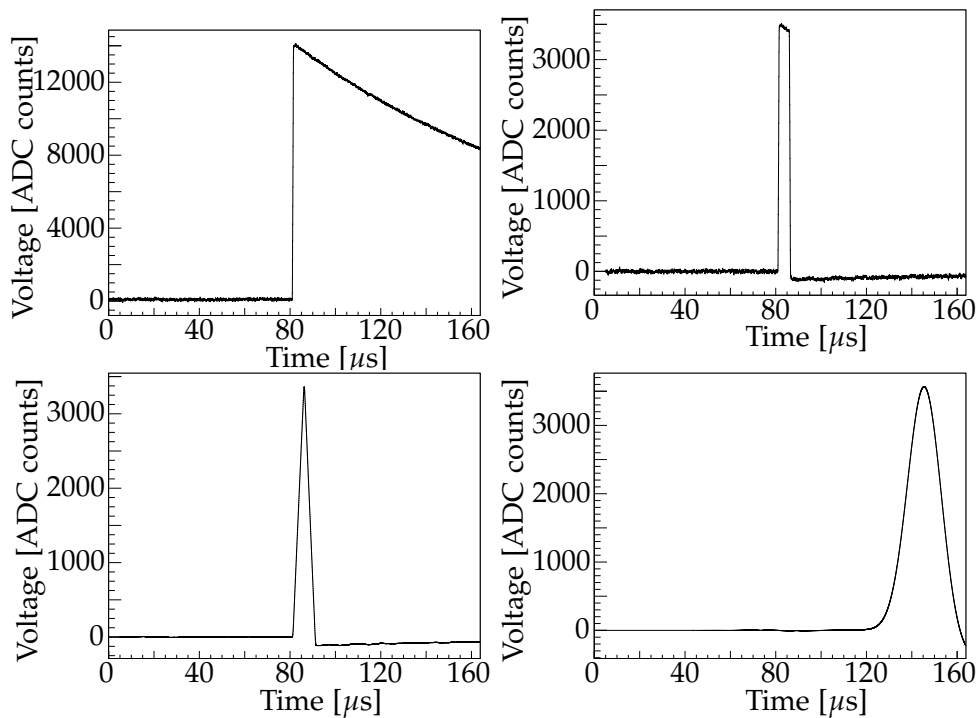
Figure 3.2: Top left: the initial waveform. Top right: the waveform after delayed differentiation. Bottom: the signal after one (left) and 25 (right) moving average operations. Figure from [55].
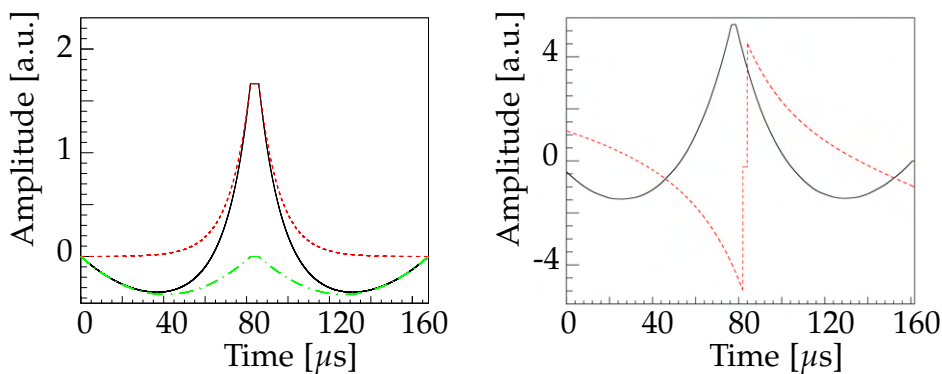

Figure 3.3: A ZAC filter (left), showing the finite cusp (red), the zero-area constraint (green) and the resulting summed filter (black). On the right, the inverse preamplifier function is shown (red) and the final filter applied to waveforms, after convolution with the ZAC filter on the left, is shown (black). Adapted from [55].
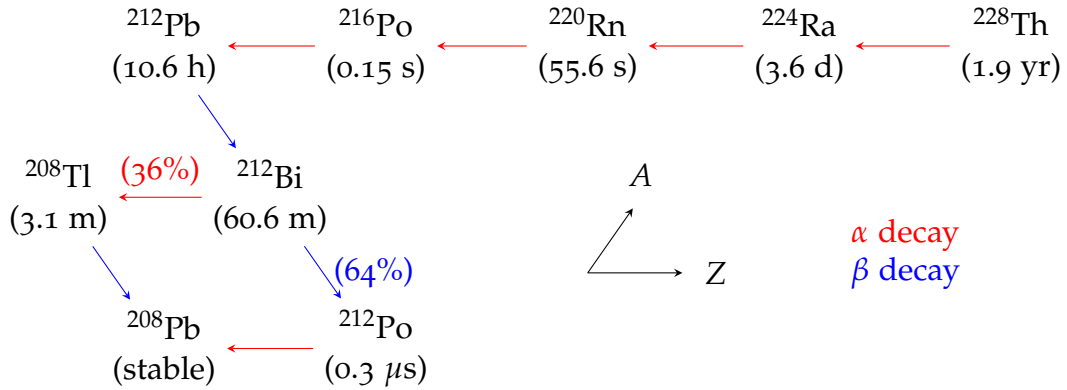
^{212}Pb ^{216}Po ^{220}Rn ^{224}Ra ^{228}Th

(10.6 h)   (0.15 s)   (55.6 s)   (3.6 d)   (1.9 yr)

^{208}Tl (36%) ^{212}Bi A

(3.1 m)   (60.6 m) α decay

(64%) $\to Z$ β decay

^{208}Pb ^{212}Po

(stable)   (0.3 μs)

Figure 3.4: The ^{228}Th decay chain. α decays are shown in red, while β decays are shown in blue. The half lives of all isotopes are reported in parentheses. Values from [135].

3.2 PROCEDURE

To convert the uncalibrated Gauss and ZAC estimators to physical energy values (into keV) the germanium detectors are exposed to ^{228}Th sources, lowered from above the cryostat alongside the detector strings.

3.2.1 *Sources*

The germanium detectors are calibrated by exposing them to three ^{228}Th sources with activities of about 10 kBq each. The ^{228}Th sources used were custom produced as a collaboration between the University of Zurich, the Paul Scherrer Institute (PSI) and the University of Mainz. Their encapsulation in gold foils reduces the rate of (α, n) reactions. It is important that the sources have a low neutron emission rate, to prevent the production of ^{77}Ge through neutron activation, whose β decay with $Q = 2.9$ MeV and $t_{1/2} = 11.3$ h would pose a problematic background for the $0\nu\beta\beta$ decay search. For more information about the production of these low-neutron emission sources, see [134].

^{228}Th is the calibration isotope of choice for a number of reasons. Its half-life of 1.9 yr is convenient with respect to the experiment's lifetime of a few years. It decays via a number of α and β decays until reaching the stable ^{208}Pb, see Figure 3.4. The consequent radiative decays after α and β decays to excited states produce monoenergetic γ rays, spanning a broad energy range. The pattern of γ lines in the resulting energy spectrum can then be exploited to identify certain γ lines and calibrate the energy scale of a detector with their known physical energies. Additionally, the detectors' energy resolutions can be determined from the width of the γ lines.

The topologies of particular γ ray events from the calibration are used to calibrate the pulse shape discrimination techniques. The highest energy

and highest intensity γ ray in the decay chain is the 2.6 MeV γ ray emitted in the ^{208}Tl decay with a branching ratio of 99.754(4)%. When this γ ray interacts in the detector volume, due to its high energy it may undergo e^+e^- pair production. The electron will deposit its energy in the detector, while the positron will quickly thermalise and then annihilate with an atomic electron in the detector. The resulting annihilation γ rays may then either be absorbed inside the detector or escape, as shown in Figure 3.5.

The peak in the energy spectrum produced when all energy is contained in the detector is called the Full Energy Peak (FEP), at 2.6 MeV. The peaks produced when one (two) annihilation γ ray(s) escape are called the Single Escape Peak (SEP) and the Double Escape Peak (DEP) respectively. For the SEP, the average energy deposited in the detector is $2.6\,\text{MeV} - m_e c^2 = 2.1\,\text{MeV}$. For the DEP, the deposited energy is $2.6\,\text{MeV} - 2m_e c^2 = 1.6\,\text{MeV}$.

For the SEP, there will be some additional broadening to the width of this peak caused by the variance in the lost annihilation γ ray energy. This additional variance is caused by the momentum uncertainty of the annihilating atomic electron, and is called Doppler broadening since the rest frame of the atomic electron and positron is no longer the rest frame of the detector [136]. This contribution can be estimated using Heisenberg's uncertainty principle.

$$\Delta x \Delta p \sim \hbar/2. \tag{3.12}$$

If Δx corresponds to the size of the germanium atom (around 1.25 Å [137]), we find $\Delta p \sim 0.8\,\text{keV}$, i.e. we expect an additional contribution to the resolution of around a keV.

The DEP is of particular interest since the energy deposited by the electron positron pair is contained within $1\,\text{mm}^3$, similarly to the two electrons in a $\beta\beta$ decay. Conversely, the FEP of ^{212}Bi at 1621 keV is more multi-site like. These peaks are therefore used to train and calibrate the various pulse shape discrimination methods.

3.2.2 Operation

Calibration data is taken approximately every 7-10 days. In total, 167 calibrations were performed during Phase II from December 2015 to November 2019. Since some periods of time were excluded from the final $0\nu\beta\beta$ decay analysis, only 142 of these calibrations were used to calibrate physics data.

During normal operation, the ^{228}Th sources are stored on top of the lock, at about $\sim 8\,\text{m}$ above the array and above the level of the LAr. Each source is encapsulated within stainless steel capsules and attached to a tantalum absorber used for shielding. Three Source Insertion Systems (SIS), developed at UZH [138] and shown in Figure 3.6, are responsible for lowering the sources into the cryostat and positioning them next to the detectors. The sources are lowered $\sim 8\,\text{m}$ via a rotary system that unrolls steel bands
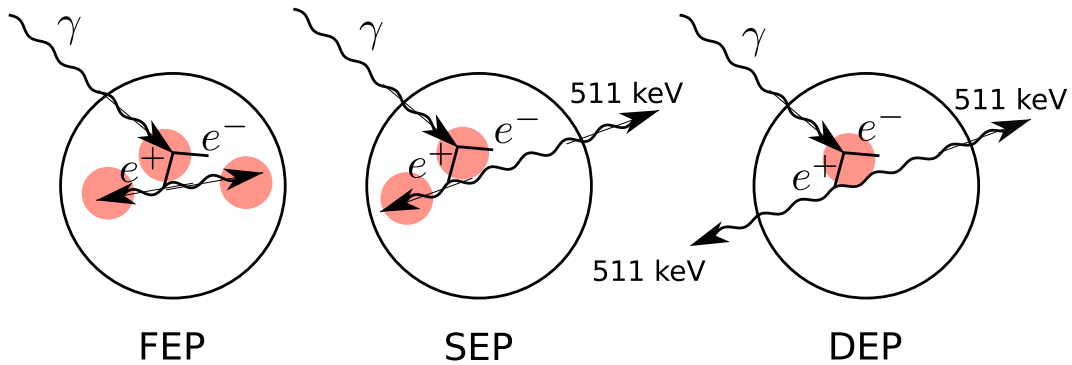
Figure 3.5: Possible event topologies due to a 2.6 MeV γ ray: 1) all the energy is contained within the detector (left), resulting in a peak at 2.6 MeV, the Full Energy Peak (FEP), or 2) one annihilation photon escapes (centre), resulting in a peak at 2.1 MeV, the Single Escape Peak (SEP), or 3) both annihilation photon escape (right), resulting in a peak at 1.6 MeV, the Double Escape Peak (DEP).

holding each source. The three sources are arranged around the detector array in order to expose them as homogeneously as possible, as shown in Figure 3.7. The sources are lowered to three heights, close to the bottom, centre and top of the array, at 8570, 8405 and 8220 mm below their initial storage position.
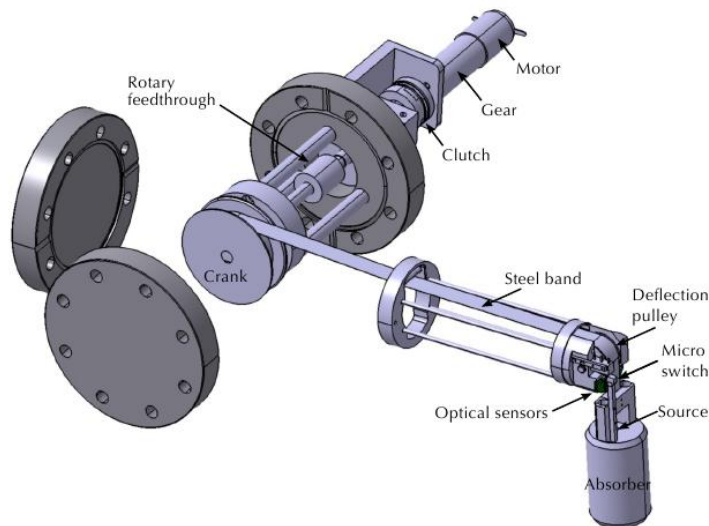

Figure 3.6: Drawing of the system used to lower the individual source from its parking position to the detector array.

During calibrations, the PMTs of the LAr veto are shutdown due to the high event rates they would otherwise observe. Until 28th August 2017 the high voltage supply of the SiPMs could not be ramped down, and so to limit data acquisition rates, only one source was lowered at a time, with
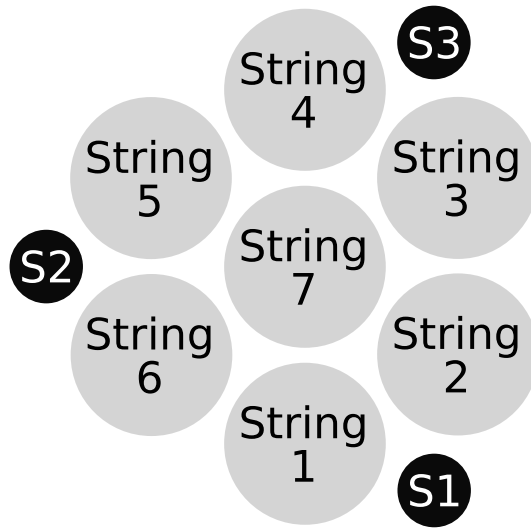
Figure 3.7: Top view of the detector strings (grey) and calibration sources (black). Not to scale.

data taken at each position data for 15-20 min. Afterwards, the voltage of the SiPMs was lowered during calibration, and all three source were lowered at once, with data taken at each height for 30 min. The time is chosen such that stronger lines and especially the double escape peak are clearly visible in every detector, while minimising the total experimental time devoted to calibrations. Typically around 1000-3000 events in the line at 2.6 MeV are observed in the smaller BEGe type detectors and 6000-10000 in the larger Coaxial and Inverted Coaxial type detectors.

The resulting energy spectrum is recorded for every detector separately. The summed spectra for each detector type from all calibrations are shown in Fig. 3.8 The calibration data is processed during data production to create tier1 data, containing waveforms in ROOT [105] format, and tier2 data, containing processed properties of the waveforms, including the Gauss and ZAC energy estimators. The calibration is performed on tier2 data with the uncalibrated energy estimators. The resulting calibration curves describing the relationship between uncalibrated energy estimators and physical energies are applied when producing tier3 data, where only the physical energies are then stored. The structure of GERDA data is briefly summarised in Table 3.1.

3.3 CALIBRATION OF THE ENERGY SCALE

The output of the analysis for each calibration run is calibration curves, i.e. functions for each detector, which describe how the uncalibrated energy estimators are transformed into physical units. Dedicated software automates much of this analysis, based on ROOT.

Data type	Format	Content
tier0	Binary	Waveforms, timestamp, muon flags, etc.
tier1	ROOT	Waveforms, timestamp, muon flags, etc.
tier2	ROOT	Uncalibrated energy, baseline, trigger, rise-time, etc.
tier3	ROOT	Calibrated energy, uncalibrated A/E, etc.
tier4	ROOT	Calibrated energy, event flags

Table 3.1: GERDA data structure

Firstly, the tier2 files are read, and quality cuts are applied to reject non-physical events. These quality cuts are similar to those used on background data and described in Section 2.3.2, but feature additional cuts to more effectively reject pile-up events since they occur more frequently during calibration runs than during physics runs due to the higher event rate, as well as those events due to the test pulser. Additionally, a cut on the uncalibrated Gauss energy of 400 a.u. removes events with low energy depositions. For more details on these cuts, see [55, 106].

The remaining events are binned into energy spectra, one for each detector. The bin width is fixed for each energy estimator and corresponds to approximately 0.3 keV, less than the expected width of the peaks. The upper range of the histograms is also fixed and corresponds to about 4 MeV, greater than the energy of the highest visible line in a single calibration, the 2.6 MeV line. Such a spectrum is shown in Figure 3.9.

A search is then performed for peaks in the spectrum, using ROOT's TSpectrum method. This algorithm searches for peaks with height greater than some threshold (5% of the height of the largest peak, in our case) and with an approximate width σ (2 bins in our case). The result is the number of peaks and their approximate positions. Each peak position is then determined more precisely by finding the position of the maximum in the ± 3 bins around the estimated peak position. The located peaks are indicated with red triangles in Figure 3.9.

γ ray lines observed with energy above 2.6 MeV are summation lines caused by the almost simultaneous emission of two γ rays as part of a cascading nuclear decay. Since these lines are of a too low intensity to be observed in a single calibration spectrum, the high intensity 2.6 MeV line can reliably be identified as the highest energy peak found. From
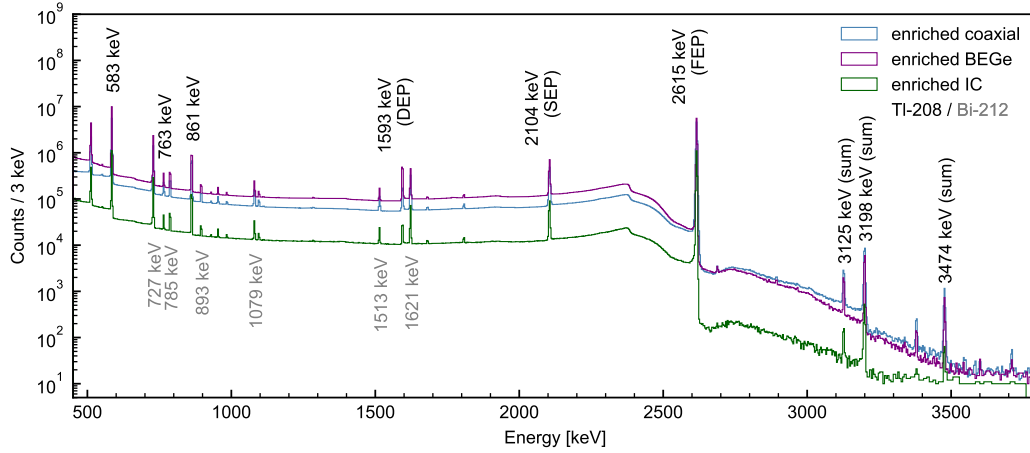
Figure 3.8: Energy spectra of ^{228}Th sources recorded with the germanium detectors of GERDA and prominent lines due to ^{208}Tl (black) and ^{212}Bi (grey). These are summed spectra over all calibrations and detectors, for each of the three detector types.

the location of this peak, T_{FEP}, a preliminary calibration for the energy estimator T is applied assuming a linear energy scale without offset:

$$E_0(T) = \frac{E_{\text{FEP}}}{T_{\text{FEP}}} \cdot T \,. \tag{3.13}$$

A candidate peak is confirmed if its preliminary estimated energy is within 6 keV of an energy in the literature values list, given in Table 3.2. The line at 510.8 keV is excluded, since this energy coincides with the annihilation peak at 511 keV, which is also affected by Doppler broadening.

The approximate energy threshold is located by looking for a sharp increase in the bin content, that is greater than 8 times the standard deviation of the first 100 bins. If the fitting region of a peak is within 20 bins of this threshold, the fit is not performed, since the shape of the threshold cannot easily be modelled. This minimum energy threshold is shown in purple in Figure 3.9, along with its estimated position in keV.

To determine the position and energy resolution of the γ line peaks, fits are performed locally around the identified peaks. The sizes of these asymmetric windows are configured individually for each peak to avoid interference from neighbouring peaks. The fitting windows vary from 10 keV to 20 keV.

Depending on the particular properties of a peak, such as the intensity, different fit functions are used to model the distribution of the energy spectrum.
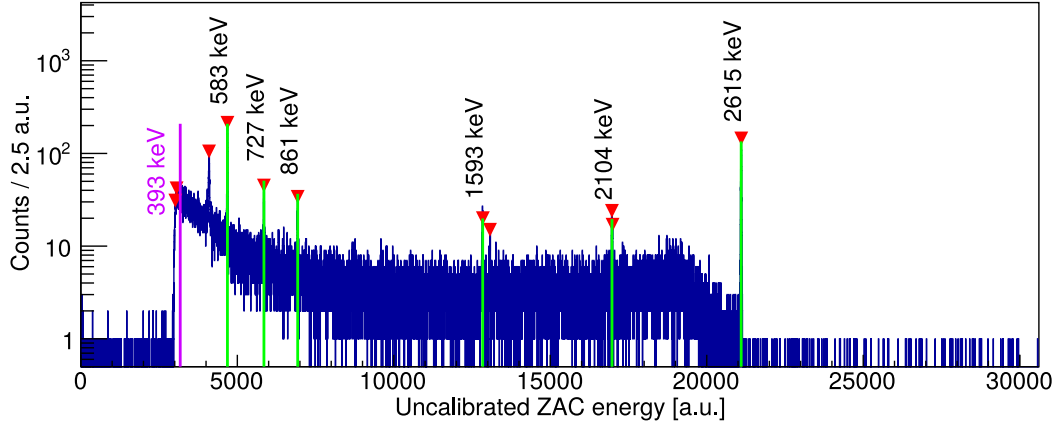
Figure 3.9: Example spectrum of the ZAC energy estimator, for the BEGe type detector GD91B from the calibration on 2nd February 2018. The minimum energy threshold for fitting, as determined by detecting the energy threshold is shown in purple, together with its estimated energy. The red triangles denote peaks found by the TSpectrum::Search method in ROOT. The vertical green lines indicate those peaks that were successfully identified with a literature value and fitted, and are labelled with their determined energies.

Isotope	Energy	Branching ratio	Fitting category
^{208}Tl	583.2 keV	84.5%	High statistics
	763.1 keV	1.81%	High statistics
	860.6 keV	13%	High statistics
	1592.5 keV	N/A	SEP/DEP
	2103.5 keV	N/A	SEP/DEP
	2614.5 keV	99.8%	High statistics
	3125.5 keV	N/A	Low statistics
	3197.7 keV	N/A	Low statistics
	3475.1 keV	N/A	Low statistics
^{212}Bi	727.3 keV	7%	High statistics
	785.4 keV	1.1%	Low statistics
	893.4 keV	0.38%	Low statistics
	1078.6 keV	0.6%	Low statistics
	1512.7 keV	0.3%	Low statistics
	1620.5 keV	1.5%	Low statistics

Table 3.2: ^{228}Th and ^{212}Bi peaks implemented in the calibration software, with branching ratios and the peak fitting category (see text).

As a minimum, a Gaussian function, g, is used to describe the signal, with a linear function, f_{lin}, describing the underlying background, defined as:

$$g(E|n, \mu, \sigma) = \frac{n}{\sqrt{2\pi}\sigma} \exp\left(-\frac{(E-\mu)^2}{2\sigma^2}\right),$$ (3.14)

$$f_{\text{lin}}(E|a,b) = a + b \cdot E, \tag{3.15}$$

where n, σ, and μ are the intensity, width, and position of the peak , and a and b give the level of the constant and linear background components respectively.

For high statistics peaks (as listed in Table 3.2), and the single- and double-escape peaks, a step function f_{step} is added to model the flat backgrounds occurring only above or below the peak from multiple Compton scatters:

$$f_{\text{step}}(E|\mu,\sigma,d) = \frac{d}{2}\text{erfc}\left(\frac{E-\mu}{\sqrt{2}\sigma}\right). \tag{3.16}$$

where d is the height of the step function.

Finally, for the high statistics peaks, a low energy tail is added to model the effects of incomplete charge collection:

$$h(E|\mu,\sigma,c,\beta) = \frac{c}{2\beta}\exp\left(\frac{E-\mu}{\beta} + \frac{\sigma^2}{2\beta^2}\right)\text{erfc}\left(\frac{E-\mu}{\sqrt{2}\sigma} + \frac{\sigma}{\sqrt{2}\beta}\right), \tag{3.17}$$

with additional fit parameters c and β parametrise the height and slope of the tail respectively. Examples of peak fits are depicted in Figure 3.10.

Peaks must then pass goodness of fit selection criteria or are excluded from further analysis. The resolution, as given by the FWHM, must be greater than 1.5 keV and less than 11 keV. The amplitude of the peak must also be at least ten counts, and greater than 2.5 times the underlying background level. Finally, the error on the Gaussian width must be less than the central value itself. The 2.6 MeV line is not required to pass these cuts to ensure at least an approximate calibration curve can be determined. Typically around 5–8 peaks per detector survive all selection criteria. γ rays below 500 keV do not typically form peaks in the calibration spectrum due to the calibration data acquisition energy threshold.

To determine the calibration curve, the peak positions in terms of the uncalibrated energy estimator T of identified peaks is plotted versus their physical energy according to literature E, and a linear function is fitted:

$$E(T) = p_0 + p_1 \cdot T. \tag{3.18}$$

This curve describes the peak positions within a few tenths of a keV. An example calibration curve for the ZAC energy estimator is shown in Figure 3.11.

Typically, the calibration curve is used to obtain an energy estimator for the physics data until the next calibration is taken. However, if a calibration is taken due to changes in the experimental setup, or instabilities in the detector array are observed, the calibration curves may be applied retrospectively to additionally calibrate the period after instabilities. The unstable period itself would be not be used for physics analysis.
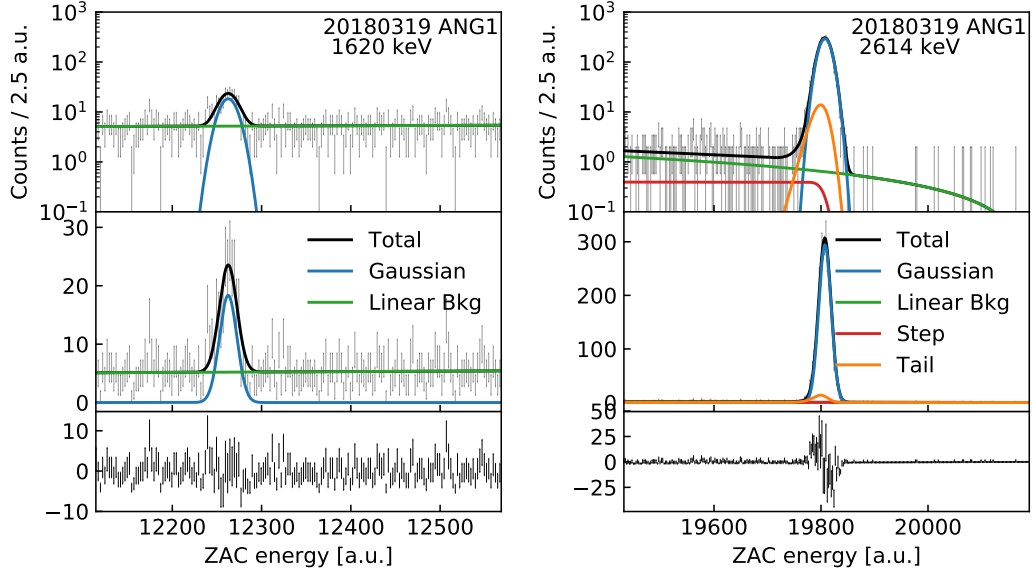
Figure 3.10: Examples of fits to peaks in the calibration spectrum for the Coaxial detector ANG1 on 19th March 2018. The left peak is the low statistics γ line at 1620 keV, and is fitted with the minimum fitting function of a Gaussian and linear background. The right peak is the high statistics γ line at 2615 keV, whose fitting function additionally includes a step function and low energy tail. The top (middle) panel shows the spectrum and fit with a logarithmic (linear) scale. The bottom panel shows the residuals of the histogram to the total fitted function.

3.3.1   *Quadratic correction*

After the 2018 upgrade, several detectors (the new IC detectors and one coaxial detector, ANG2) exhibited larger residuals in their calibration curves compared to the other detectors, up to 2.5 keV at 1.5 MeV, for ANG2. These effects could be largely accounted for by the incorporation of a quadratic correction to the calibration curves

$$E(T) = m_0 + m_1 \cdot E_0(T) + m_2 \cdot E_0^2(T), \qquad (3.19)$$

where E_0 is the energy estimator after the application of the linear calibration curve as described in Section 3.3.

The parameters m_0, m_1 and m_2 were determined by fitting the residuals of each detector's calibration curves, as shown in Figure 3.12. These parameters were observed to be stable, with the exception of a single jump for IC48A, IC50A and IC50B following operations in the clean room, as shown in Figure 3.13. Therefore a single correction for each detector's stable period was applied, using average parameters.

After the quadratic correction, the remaining residuals were within a few tenths of a keV as for the other detectors (see Section 3.7).
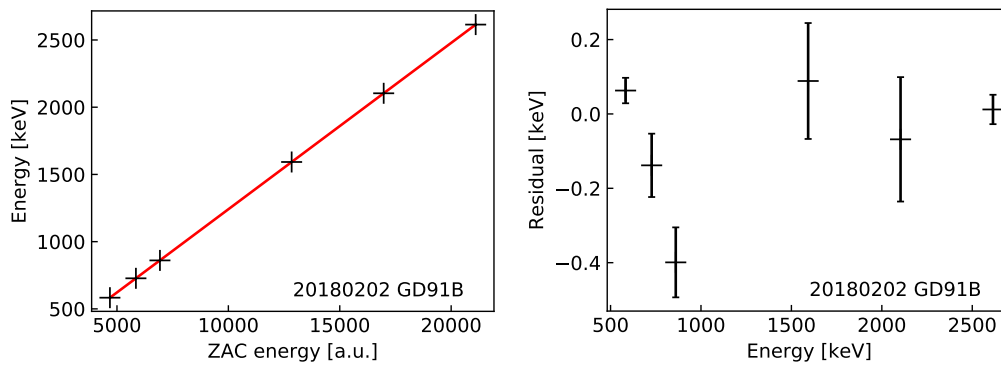
Figure 3.11: Calibration curve (left) and residuals (right) for the BEGe type detector GD91B, from the calibration taken on 2nd February 2018.
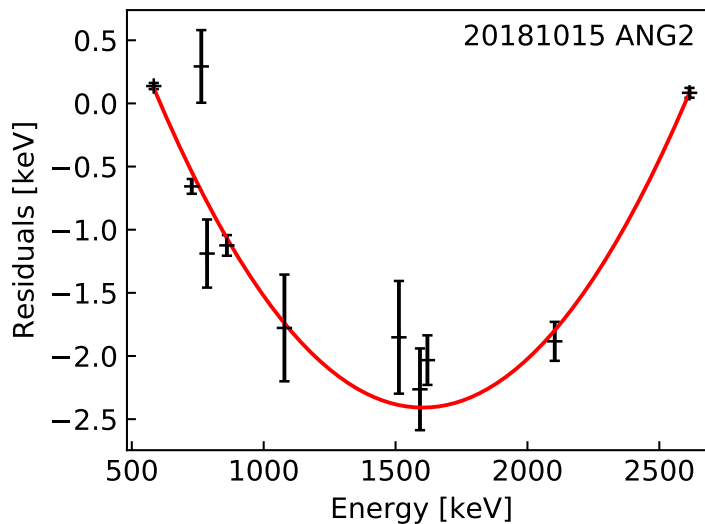

Figure 3.12: Fitting the residuals of the calibration curve with a quadratic function, as shown for detector ANG2 for the calibration on 15th October 2018.

3.4 MONITORING OF DETECTOR PERFORMANCE AND STABILITY

To consistently combine data over an extended period of time while preserving the excellent energy resolution of the germanium detectors, it is vital to monitor the stability of the energy scale and exclude periods with shifts and fluctuations which would degrade the peaks' widths. At the same time, as much data should be preserved for the $0\nu\beta\beta$ decay search analysis in order to reach the highest possible sensitivity.

As explained in Section 2.3.1, test pulses are regularly injected into the readout electronics to monitor the stability of the data acquisition system. Periods with significant ($> 1\,\text{keV}$) jumps or drifts in the output of the electronics chain are excluded from data analysis and a calibration is performed once the affected detectors stabilise.
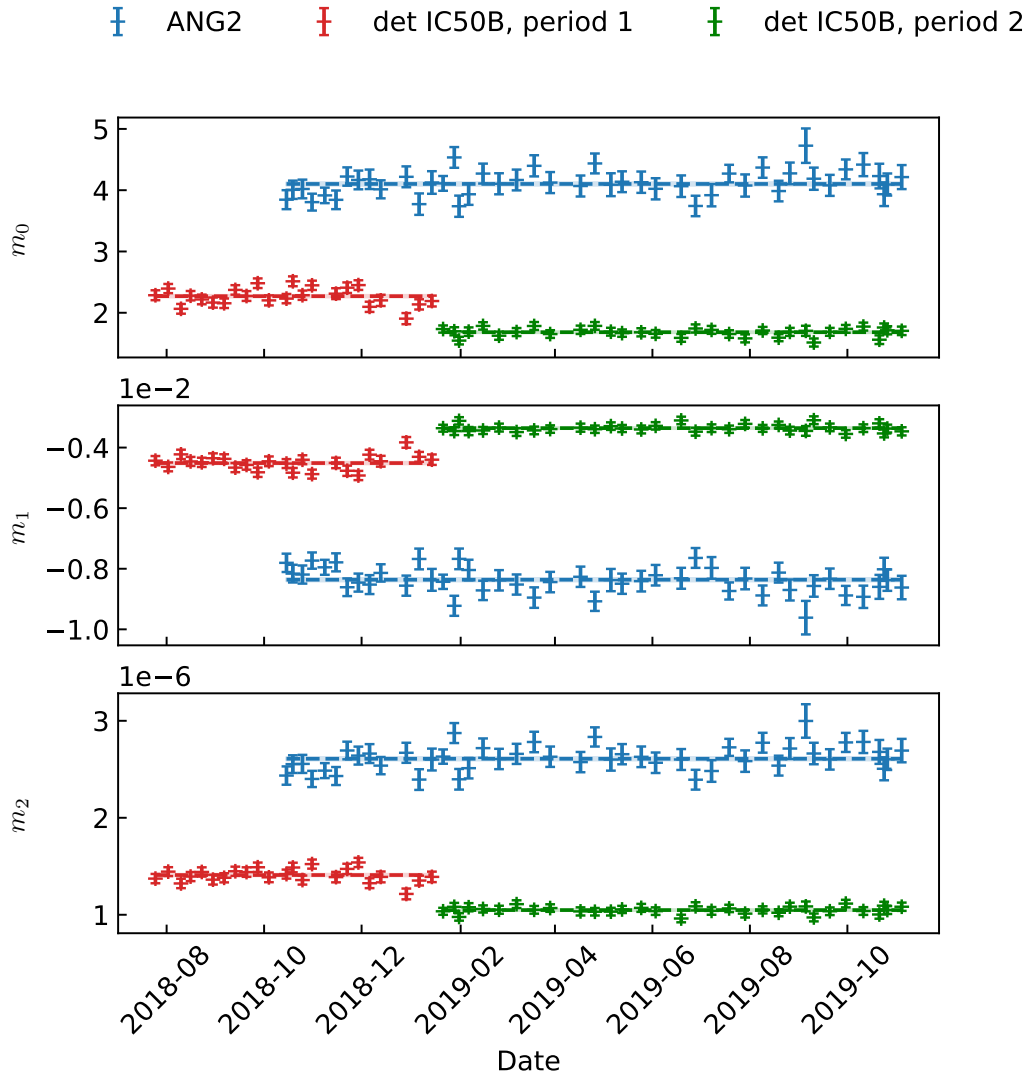
Figure 3.13: Stability of the quadratic components to the residual over time. While the parameters of the quadratic correction are stable for ANG2, IC50B exhibits a significant jump and therefore two corrections are applied. While IC74A is as equally stable as ANG2, the other IC detectors have a jump at the same time as IC50B and two corrections are applied (not shown). The lines and bands show the fitted central values used in the correction.

We observe the position and width of the high intensity 2.6 MeV γ line in the calibration spectrum, using the Gauss energy estimator. If the position of this line changes beyond 1 keV between successive calibrations without an identifiable reason (such as maintenance works or some specific incident such as the earthquake in August 2016), the data of the respective detector is discarded for that period of time. Smaller or temporary drifts may still affect the obtainable effective energy resolution and are discussed as a systematic uncertainty in Section 3.6.3.

The shift in energy scale is defined as the shift in the position of the 2.6 MeV γ line, approximated as

$$\Delta E = (T_1 - T_2) \cdot \frac{2614.5\,\text{keV}}{T_2}, \qquad (3.20)$$

where T_1 and T_2 label the position of the line in uncalibrated units for the two successive calibrations.

If the energy scale changes beyond what we consider tolerable between calibrations, around 1 keV, without an identifiable reason (maintenance, longer break, incident), data of the respective detector is discarded from the analysis dataset, and the detector is used only in anti-coincidence (AC) mode, i.e. only to determine the event multiplicity, and not contributing exposure to the $0\nu\beta\beta$ decay search analysis.

The energy resolution is monitored by comparing the width of the 2.6 MeV γ line between successive calibrations. As we use average resolutions derived from multiple calibrations (see Section 3.5) for each detector's partition (see Section 3.5.1) in the statistical analysis, the resolution must be sufficiently stable during the time period of each partition, so the average resolution is indeed representative. Smaller or temporary drifts may still affect the obtainable energy resolution and are discussed as a systematic uncertainty in Section 3.6.3.

Plots and tables detailing the shifts and resolution of the 2.6 MeV line for each detector channel are reported to the collaboration after each calibration, in addition to general comments on the calibration's stability. An example is shown in Figure 3.14. In Figure 3.15 the fluctuations in the energy scale are depicted over time, while in Figure 3.16 the stability of the detectors' resolutions is shown. Figure 3.17 shows the average stability performance, where each calibration's shift is estimated as the mean of all shifts for each detector type with the standard deviation shown as error bars. The estimated mean ($\pm$ standard deviation) shift is $(0.01 \pm 0.37)\,\text{keV}$, $(-0.03 \pm 0.45)\,\text{keV}$, and $(-0.01 \pm 0.35)\,\text{keV}$ for the BEGe, Coaxial and IC detector types, respectively.
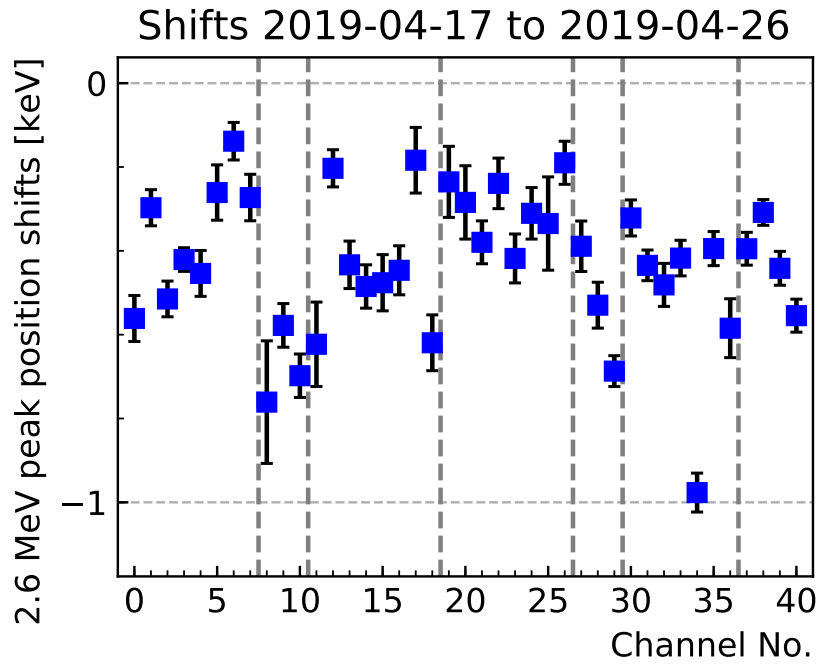
(a) Relative shifts of the 2.6 MeV γ line of detectors between the calibrations on 17th April 2019 and 26th April 2019.
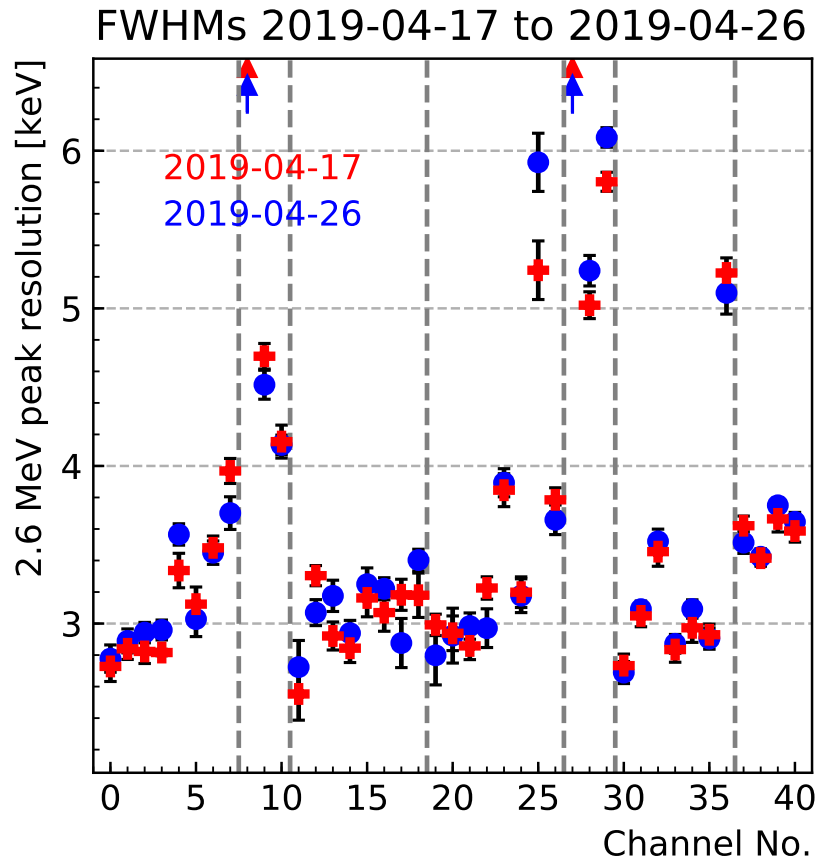
(b) Resolutions of the 2.6 MeV γ line of detectors on the calibrations on 17th April 2019 and 26th April 2019.

Figure 3.14: Monitoring plots as sent to the gerda-runteam email list for the calibration of 26th April 2019. The grey lines separate the detectors on different strings.
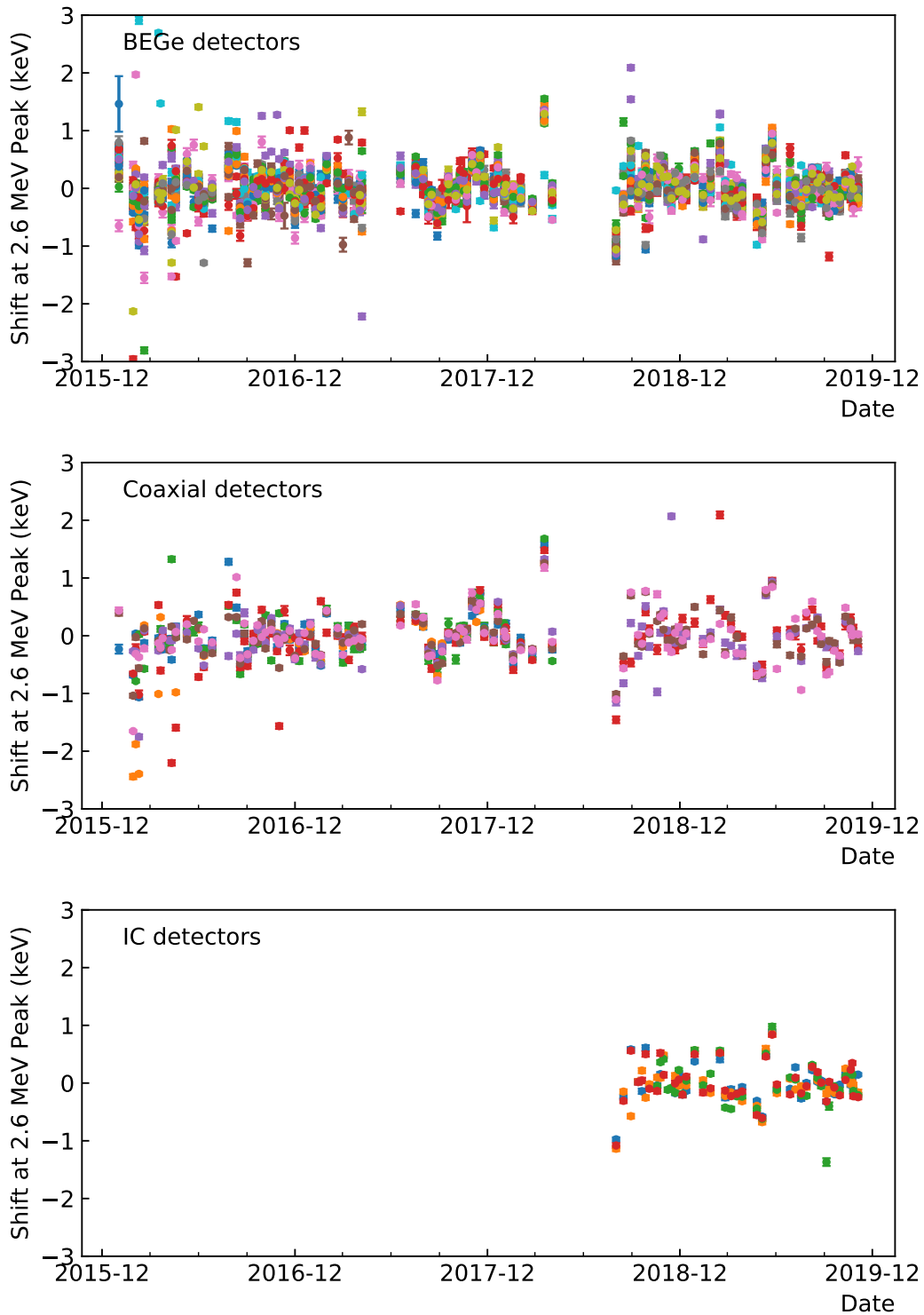
Figure 3.15: Shifts in energy scale (as defined in Eq. 3.20) between calibration for the three detector types. Each colour represents a different detector of a given detector type.
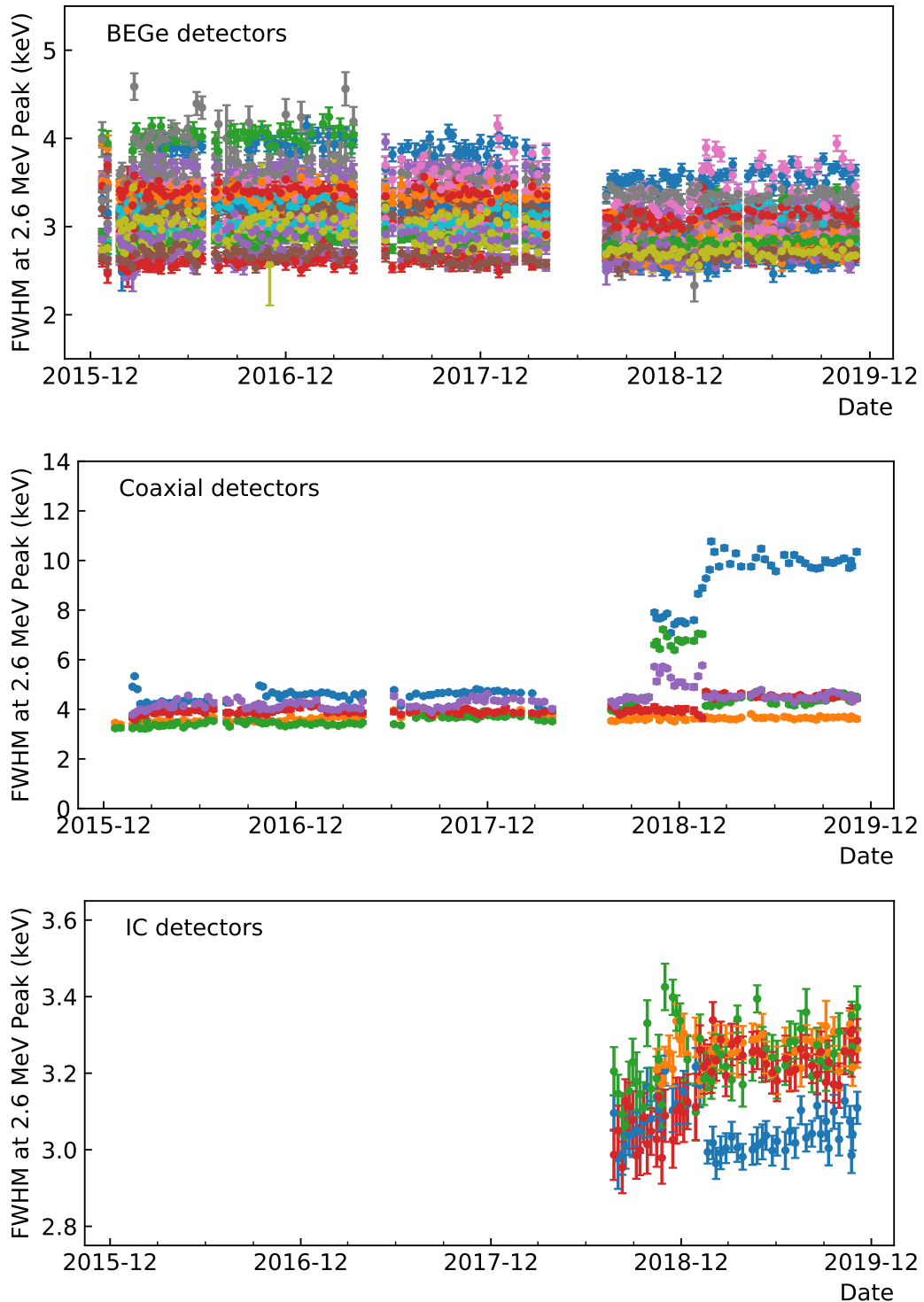
Figure 3.16: Resolution of the 2.6 MeV line over time for the three detector types. Each colour represents a different detector of a given detector type. Note the differing ranges of the y-axis in each case. While the resolution of the BEGe detectors generally improved after the mid-2018 upgrade, the resolution of the Coaxial detectors became more unstable after this point. In particular the resolution of the Coaxial detector ANG2 (shown in blue) at 2.6 keV eventually degraded to more than 10 keV.
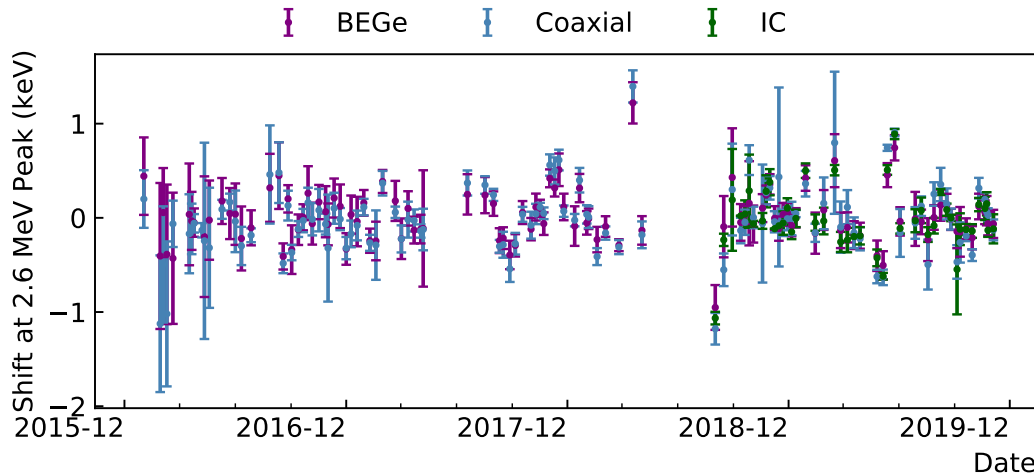
Figure 3.17: Stability of the 2.6 MeV line over time, averaged for each detector type. The centre point indicates the mean value, while the error bar indicates the RMS variation across detectors for that calibration.

3.5 ANALYSIS OF COMBINED CALIBRATION SPECTRA

As described in Section 2.3.4, the $0\nu\beta\beta$ decay analysis requires inputs for each of the 408 partitions, such as the signal efficiency and energy resolution. In addition, parameters such as the uncertainty on the energy resolution and energy reconstruction are required to determine the uncertainty on the limit. This section describes how the partitions are divided according to the stability of the detectors, and how the necessary values are evaluated.

In earlier GERDA $0\nu\beta\beta$ decay analyses, partitioning was not performed, and data from multiple detectors was combined to form a dataset for each detector type. Therefore effective values were calculated for the resolution and energy construction uncertainty for each dataset, by combining data from multiple detectors. The partitioning was introduced as a more fine-grained approach to take advantage of additional information about our detectors. However, this approach comes with an increase in complexity and required computing power. Since both approaches are valuable for describing modular experimental setups such as GERDA, MAJORANA and CUORE, they are each described here.

3.5.1 *Partitioning*

Due to hardware changes, the detectors may experience jumps in their energy resolution and energy scale over time. To more accurately reflect the properties of a detector at a certain time, for the final GERDA analysis [88],

we divide the full data taking period into stable sub-periods called partitions.

The stability is judged based on two parameters: the resolution at the FEP (2.6 MeV) and the residual at the SEP (2.1 MeV), defined as

$$\Delta E = E_{true} - E_{cal}, \tag{3.21}$$

where $E_{true} = 2103.512$ keV is the literature value for the SEP energy, and E_{cal} is the calibrated position of the peak, determined by fitting the calibrated energy spectrum. The former reflects the changes in the detector resolution, while the latter catches the changes in the energy bias at the energy peak closest to $Q_{\beta\beta}$, with an energy difference of 65 keV. Examples are shown in Figure 3.18.

All divisions are based on visual inspections with a rough guideline, e.g., resolution jumps $\gtrsim 0.3$ keV were generally considered in making a division. The majority of the detectors have only one division at the time of the upgrade that took place in mid-2018. Other times where a division was made coincide with hardware operations, as shown in Table 3.3, and the start time is given by the validity start of the following calibration.

After these divisions, each detector is divided into one to four periods, as shown in Figure 3.19. For the purposes of the statistical analysis, a partition is defined by a period where all detectors' parameters are stable. Therefore by this definition, 408 partitions are formed, split by detector and the times given on the y-axis of Figure 3.19. During the calibration analysis each detector is treated separately, thus in the following the word partition will be used to describe the stable sub-periods of each detector. We therefore count 85 partitions for which the resolution and other parameters must be evaluated.

3.5.2 *Combined calibration spectra*

We calculate the relevant parameters for the $0\nu\beta\beta$ decay search analysis for each partition from combined energy spectra of all calibrations in that partition. This needs to be performed on calibrated spectra with consistent binning to consistently sum same energy bins in the histogram and avoid deterioration of resolution or peak shape due to fluctuations of the uncalibrated energy scale over time.

As an improvement to the previous method of simply adding all calibration spectra, the combined spectra are now formed by first normalising each calibration to account for varying statistics. The statistics collected during a calibration vary for a number of reasons, including the decay of the sources with their half-life of 1.9 yr, replacement of the sources, and the variation in the length of the calibration runs themselves. A proxy for the degree of statistics collected is given by the number of events above 2.4 MeV, and is shown in Figure 3.20a.
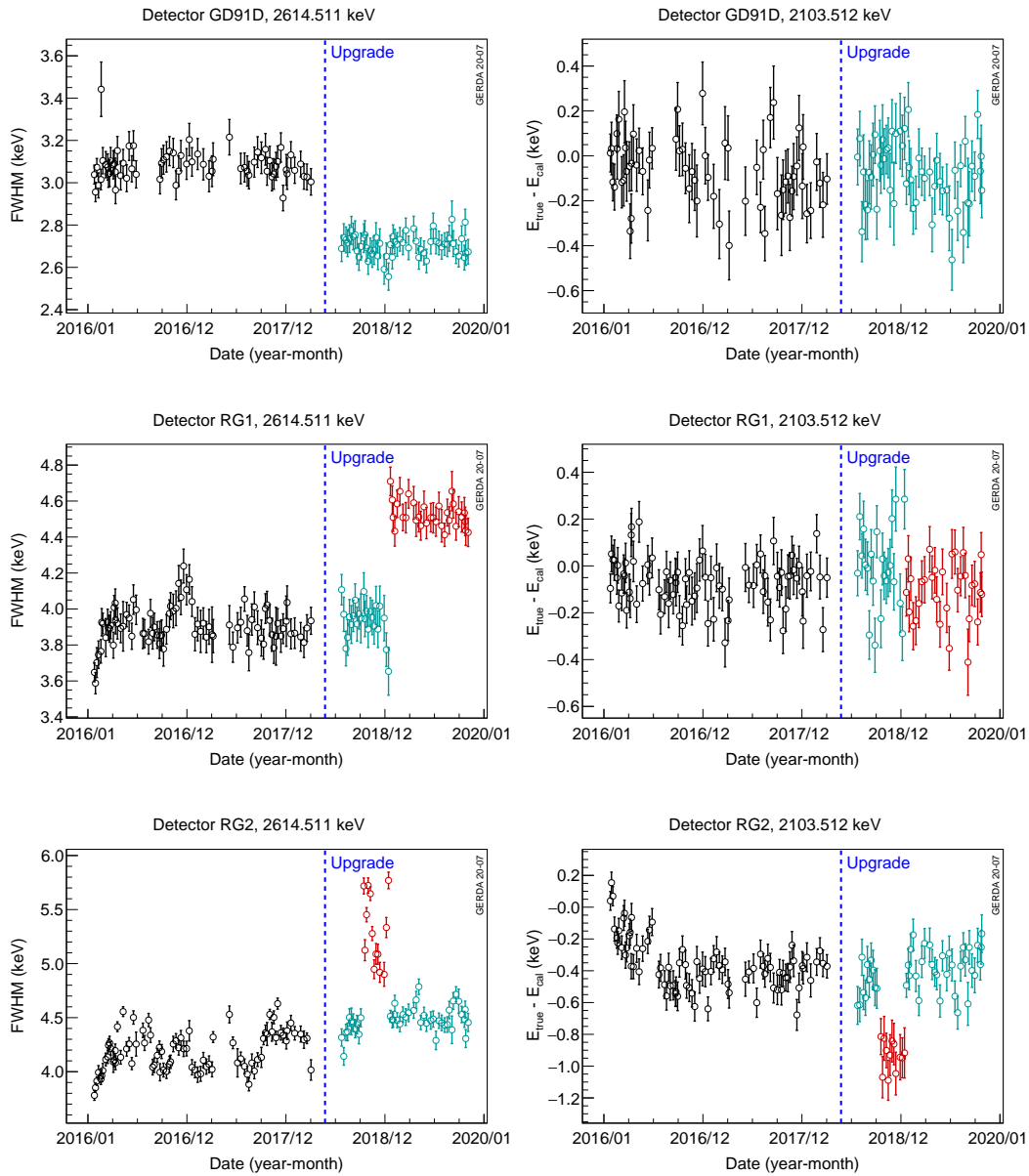
Figure 3.18: Examples of partitioning based on the stability of the resolution of the 2.6 MeV γ line and the residual of the SEP at 2.1 MeV. Different groups are shown in different colours. Most detectors are partitioned only at the time of the upgrade in mid-2018, as an improvement in the resolution of most BEGe detectors was observed, along with a degradation in the resolution of the Coaxial detectors.

Time in UTC	Calibration	Reason
2015-12-20 14:42:52	run0053, 20151223	start of data taking
2016-07-21 16:42:26	run0069, 20160722	residual change in GD02C
2016-09-23 08:35:06	run0072, 20160923	residual change in GD79C, resolution change in ANG2
2017-06-02 13:24:00	run0083, 20170606	water tank refilled, resolution change in ANG3
2017-07-03 13:07:18	run0084, 20170706	after HV filter change, resolution change in ANG4
2018-07-20 12:56:28	run0095, 20180725	start of data taking after upgrade
2018-10-15 07:27:35	run0098, 20181015	resolution change in ANG4 and RG2, some HV adjustments to other channels
2018-12-21 18:39:59	run0100, 20181229	after special calibration run, resolution change in GD00C
2019-01-05 18:47:28	run0101, 20190106	after power loss, resolution change in ANG2
2019-01-19 22:06:46	run0103, 20190121	after Ra calibration (same as quadratic correction split), resolution change in ANG4, RG2, and RG1
2019-01-31 13:04:32	run0104, 20190131	after power loss, resolution change in GD76B

Table 3.3: Timestamps used for splitting the data taking period in different detectors.
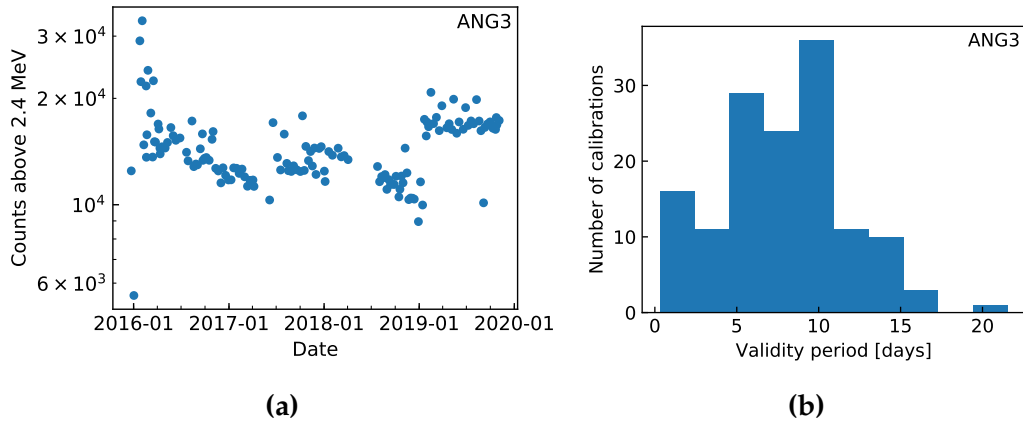
Figure 3.19: The division of the detectors' data into partitions. The majority of the detectors have only one split at the time of the upgrade that took place in mid-2018. Additional divisions are made for 9 detectors: ANG2, ANG3, ANG4, GD00C, GD02C, GD76B, GD79C, RG1 and RG2. Here the dark blue, bright blue, green and yellow colour blocks indicate the zeroth, first, second and third partitions respectively of each detector. White blocks indicate where a detector does not contribute data.

They are then weighted according to the period where the corresponding calibration curves were applied to physics data. For ANG3, this can vary between 0.29 days and 22 days, with an average of 7.9 days, as shown in Figure 3.20b.

This entire procedure for forming such a combined energy spectrum, or superspectrum, for each detector and partition, is therefore defined as:

$$\text{superspectrum}_{\text{det, partition}} = \Sigma_{\text{cals}}\, w_{\text{det, cal}} \cdot \text{spectrum}_{\text{det, cal}}, \tag{3.22}$$

where

$$w_{\text{det, cal}} \propto \frac{\text{physics duration}}{\text{events above } 2.4\,\text{MeV}} \tag{3.23}$$

The effect of this weighting is shown schematically in Figure 3.21. The combined spectrum for ANG3 for its first partition is shown in Fig. 3.22.

3.6 ENERGY RESOLUTION

3.6.1 *Resolution curves*

Once the calibration spectrum is formed, peaks can be located by their literature values, since this is now a calibrated spectrum. The fit procedure described in 3.3 is then applied to determine the width of each peak.

Lines are excluded with energy less than 500 keV which may be close to the data acquisition threshold, as well as summation peaks. Since Doppler

(a)   **(b)**

Figure 3.20: Left: the number of events above 2.4 MeV for each calibration run for ANG3. Right: the amount of time calibrations are applied to physics data for ANG3.
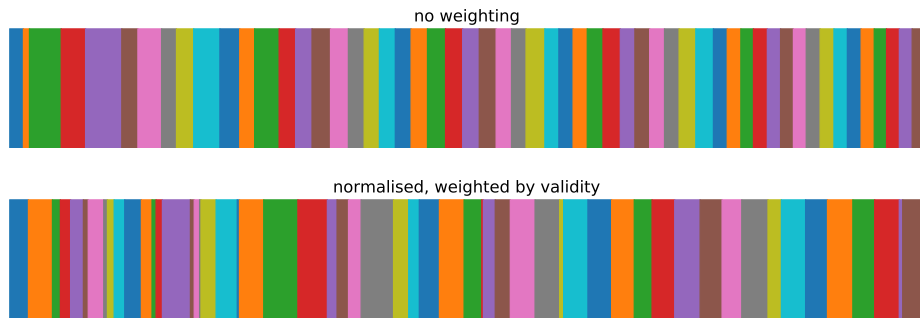
Figure 3.21: The effect of weighting calibration contributions to the combined spectrum for the first partition of ANG3. In the top image, each bar represents a calibration and the width is given by the amount of statistics gathered in each calibration. This shows the contribution each calibration would make to the combined spectrum if they were simply summed. In the bottom image the width is given by the exposure contribution of that calibration to the physics data. This shows the contribution of each calibration after the weighting procedure.
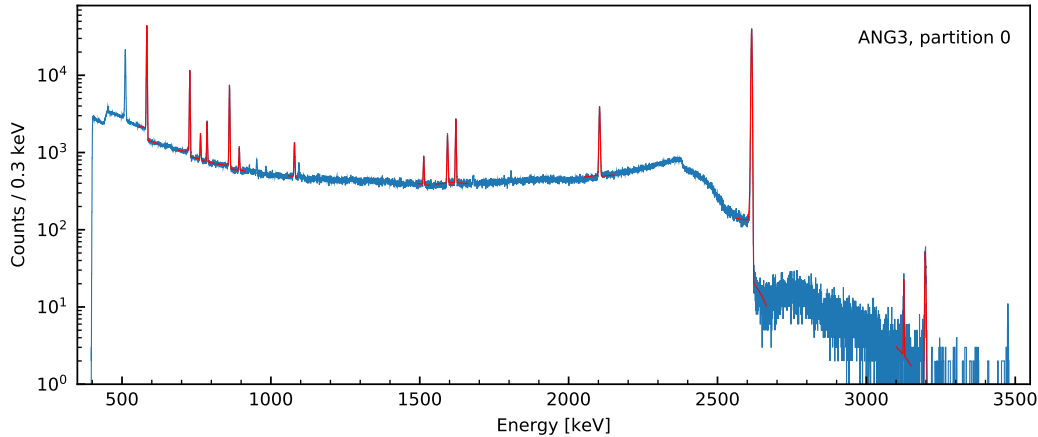
Figure 3.22: Combined ZAC energy spectrum for the first partition of ANG3. The red lines show the fits to peaks in the spectrum.

broadening is expected in the SEP at 2.1 keV, this is also excluded. Broadening is also observed in the double escape peak, hypothesised to originate due to the events occurring more frequently in the outer regions of the detectors and thus being more susceptible to incomplete charge collection [139]. This line is therefore excluded as well.

The remaining resolutions are then fitted with the semi-empirical formula

$$\text{FWHM} = 2.355\,\sigma = 2.355\sqrt{a + bE}, \tag{3.24}$$

with energy E and fit parameters a and b. Figure 3.23 shows the resolution curve obtained for the first partition of ANG3.

Resolutions at $Q_{\beta\beta}$ and best fit parameters for Eq. 3.24 are listed in Table 3.4. The uncertainties listed are purely statistical and derived from the fit. See Section 3.6.3 for a discussion of systematic uncertainties.

3.6.2 *Effective resolution of a dataset*

While resolution curves for detector partitions give the most fine-grained information about the behaviour of the germanium detectors, various analyses require the combination of multiple detectors' data, and therefore effective resolutions, possibly at numerous energies, describing the behaviour of that group are required. Effective resolutions are also convenient for describing the behaviour of the array as a whole, for example for presentation purposes.

The method used for calculating effective resolutions depends on the specific application. In the following, the resolution curves used for background modelling, and those previously used for the $0\nu\beta\beta$ decay search, are discussed.
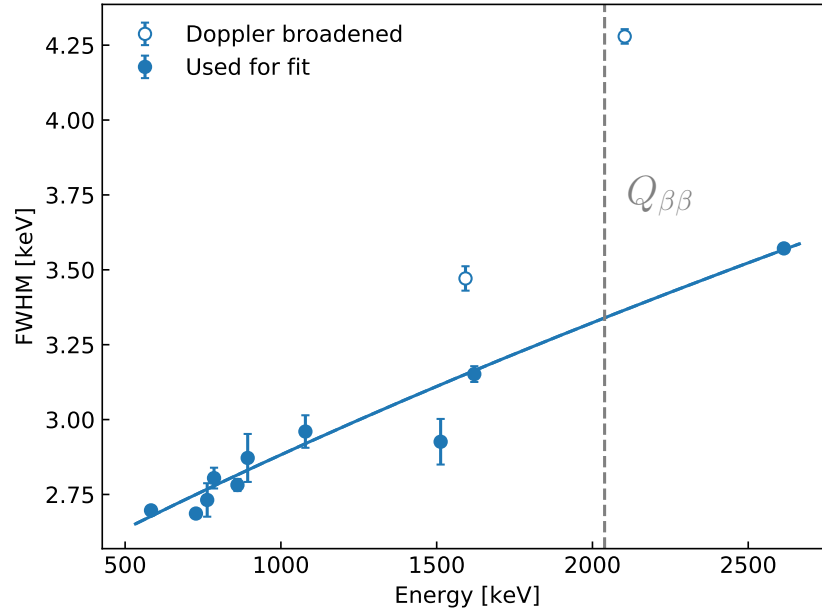
Figure 3.23: ZAC energy resolution of peaks of the combined calibration spectrum for the first partition of ANG3. The parameters in Equation 3.24 are determined from a fit, and the value at $Q_{\beta\beta}$ is then interpolated.

Detector	Partition	FWHM at $Q_{\beta\beta}$ [keV]	a [keV^2]	b [10^{-4} keV]
ANG1	0	3.425 ± 0.006	1.187 ± 0.008	4.56 ± 0.06
ANG2	0	4.014 ± 0.007	1.28 ± 0.01	7.96 ± 0.08
	1	4.168 ± 0.005	1.014 ± 0.006	10.39 ± 0.06
	2	6.78 ± 0.02	1.05 ± 0.03	35.5 ± 0.3
	3	8.81 ± 0.01	0.51 ± 0.02	66.1 ± 0.3
ANG3	0	3.340 ± 0.005	1.005 ± 0.007	4.94 ± 0.05
	1	3.615 ± 0.008	1.24 ± 0.01	5.47 ± 0.08
	2	3.406 ± 0.005	0.987 ± 0.007	5.42 ± 0.05
ANG4	0	3.129 ± 0.004	0.713 ± 0.007	5.16 ± 0.04
	1	3.431 ± 0.008	0.93 ± 0.01	5.84 ± 0.08
	2	3.878 ± 0.005	0.644 ± 0.009	10.14 ± 0.06
	3	6.00 ± 0.01	0.19 ± 0.02	30.8 ± 0.2
ANG5	0	3.288 ± 0.006	0.967 ± 0.006	4.82 ± 0.05
GD00A	0	3.03 ± 0.01	0.830 ± 0.009	4.0 ± 0.1
	1	2.334 ± 0.009	0.220 ± 0.005	3.74 ± 0.05
GD00B	0	2.988 ± 0.007	0.859 ± 0.008	3.68 ± 0.06
	1	2.484 ± 0.007	0.336 ± 0.005	3.81 ± 0.05
GD00C	0	2.631 ± 0.005	0.476 ± 0.004	3.79 ± 0.04
	1	2.50 ± 0.01	0.327 ± 0.006	3.93 ± 0.07
	2	2.786 ± 0.009	0.485 ± 0.009	4.49 ± 0.07
GD00D	0	2.787 ± 0.006	0.656 ± 0.007	3.65 ± 0.05
	1	2.514 ± 0.007	0.350 ± 0.005	3.87 ± 0.05
GD02A	0	2.391 ± 0.006	0.253 ± 0.003	3.81 ± 0.04

Detector	Partition	FWHM at $Q_{\beta\beta}$ [keV]	a [keV^2]	b [10^{-4} keV]
	1	2.414 ± 0.009	0.276 ± 0.005	3.80 ± 0.05
GD02B	0	2.91 ± 0.01	0.78 ± 0.01	3.7 ± 0.1
	1	2.55 ± 0.01	0.385 ± 0.008	3.85 ± 0.07
GD02C	0	2.67 ± 0.01	0.310 ± 0.008	4.79 ± 0.09
	1	2.688 ± 0.008	0.308 ± 0.005	4.88 ± 0.06
	2	2.681 ± 0.007	0.315 ± 0.005	4.81 ± 0.05
GD32A	0	3.34 ± 0.02	0.49 ± 0.02	7.4 ± 0.1
	1	2.56 ± 0.01	0.374 ± 0.008	3.97 ± 0.07
GD32B	0	2.692 ± 0.005	0.483 ± 0.003	4.04 ± 0.03
	1	2.554 ± 0.008	0.356 ± 0.005	4.02 ± 0.05
GD32C	0	2.760 ± 0.006	0.544 ± 0.005	4.07 ± 0.04
	1	2.493 ± 0.007	0.297 ± 0.006	4.04 ± 0.05
GD32D	0	3.020 ± 0.005	0.795 ± 0.006	4.17 ± 0.04
	1	2.645 ± 0.007	0.435 ± 0.006	4.05 ± 0.05
GD35A	0	3.121 ± 0.005	0.976 ± 0.007	3.83 ± 0.05
	1	2.665 ± 0.007	0.499 ± 0.006	3.83 ± 0.05
GD35B	0	2.600 ± 0.004	0.382 ± 0.003	4.11 ± 0.03
	1	2.473 ± 0.006	0.310 ± 0.006	3.89 ± 0.04
GD35C	0	2.338 ± 0.005	0.193 ± 0.003	3.89 ± 0.03
	1	2.409 ± 0.008	0.257 ± 0.004	3.87 ± 0.05
GD61A	0	3.347 ± 0.008	1.032 ± 0.008	4.84 ± 0.07
	1	2.809 ± 0.009	0.409 ± 0.008	4.97 ± 0.07
GD61B	0	2.997 ± 0.006	0.741 ± 0.009	4.31 ± 0.06
	1	2.732 ± 0.008	0.351 ± 0.005	4.88 ± 0.06
GD61C	0	3.265 ± 0.006	1.15 ± 0.01	3.79 ± 0.06
	1	2.600 ± 0.008	0.425 ± 0.007	3.90 ± 0.06
GD76B	0	3.30 ± 0.01	1.14 ± 0.02	4.0 ± 0.1
	1	2.44 ± 0.02	0.38 ± 0.01	3.4 ± 0.1
	2	2.65 ± 0.01	0.35 ± 0.01	4.5 ± 0.1
GD76C	0	2.562 ± 0.006	0.329 ± 0.004	4.19 ± 0.04
	1	2.398 ± 0.006	0.206 ± 0.003	4.07 ± 0.03
GD79B	0	2.936 ± 0.007	0.353 ± 0.005	5.89 ± 0.05
	1	2.86 ± 0.01	0.270 ± 0.008	5.89 ± 0.08
GD79C	0	3.55 ± 0.02	0.75 ± 0.02	7.4 ± 0.2
	1	3.53 ± 0.01	0.86 ± 0.01	6.8 ± 0.1
	2	3.110 ± 0.008	0.356 ± 0.006	6.81 ± 0.06
GD89A	0	3.185 ± 0.008	1.07 ± 0.01	3.71 ± 0.08
	1	2.427 ± 0.007	0.332 ± 0.005	3.58 ± 0.05
GD89B	0	3.84 ± 0.01	1.83 ± 0.01	4.0 ± 0.1
	1	2.536 ± 0.009	0.391 ± 0.007	3.77 ± 0.06
GD89C	0	3.149 ± 0.007	0.747 ± 0.009	5.11 ± 0.06
	1	2.790 ± 0.008	0.375 ± 0.006	5.04 ± 0.06
GD89D	0	2.671 ± 0.009	0.548 ± 0.007	3.62 ± 0.07
	1	2.385 ± 0.009	0.278 ± 0.007	3.67 ± 0.06
GD91A	0	2.390 ± 0.006	0.245 ± 0.004	3.85 ± 0.04

Detector	Partition	FWHM at $Q_{\beta\beta}$ [keV]	a [keV^2]	b [10^{-4} keV]
	1	2.409 ± 0.007	0.250 ± 0.005	3.91 ± 0.05
GD91B	0	3.48 ± 0.01	1.46 ± 0.02	3.6 ± 0.1
	1	3.169 ± 0.008	0.919 ± 0.009	4.37 ± 0.07
GD91C	0	3.70 ± 0.02	1.33 ± 0.02	5.6 ± 0.2
	1	3.026 ± 0.008	0.427 ± 0.006	6.01 ± 0.06
GD91D	0	2.856 ± 0.006	0.682 ± 0.007	3.87 ± 0.05
	1	2.444 ± 0.006	0.288 ± 0.005	3.87 ± 0.04
IC48A	0	2.744 ± 0.004	0.283 ± 0.004	5.27 ± 0.03
IC50A	0	2.944 ± 0.005	0.343 ± 0.005	5.98 ± 0.04
IC50B	0	2.874 ± 0.005	0.197 ± 0.004	6.34 ± 0.04
IC74A	0	2.841 ± 0.006	0.293 ± 0.005	5.70 ± 0.05
RG1	0	3.683 ± 0.006	1.194 ± 0.009	6.14 ± 0.06
	1	3.74 ± 0.01	1.49 ± 0.02	5.1 ± 0.1
	2	4.13 ± 0.01	1.02 ± 0.01	10.1 ± 0.1
RG2	0	3.861 ± 0.005	0.982 ± 0.008	8.36 ± 0.05
	1	4.122 ± 0.009	1.23 ± 0.01	9.0 ± 0.1
	2	4.69 ± 0.02	0.96 ± 0.02	14.8 ± 0.2

Table 3.4: Resolution at $Q_{\beta\beta}$ and parameters and errors of Eq. 3.24 for all enriched detectors and partitions

Gaussian mixture for background modelling

One application concerns the fitting and modelling of the GERDA background spectrum, as in [109]. Here, events are divided into three datasets depending on the event multiplicity and the detector geometry, namely BEGe detectors and Coaxial detectors. Simulations are used to model contributions to the energy spectra, where event energies are smeared with resolution curves to better describe the data.

When the data from different detectors are combined into a single dataset, Gaussian peaks in the individual spectra combine to become the sum of multiple Gaussian distributions with different centroids and resolutions: a Gaussian mixture. An example with constrasting properties of individual Gaussians is shown in Fig. 3.24. If instead the properties of the individual Gaussians are sufficiently similar, the resulting peak will be approximately Gaussian and can be modelled as such. The width of a Gaussian which models the Gaussian mixture is defined as the effective resolution.
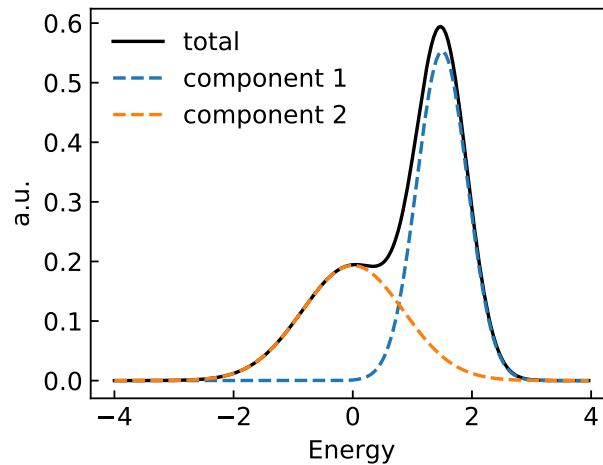
Figure 3.24: Schematic to show the combination of two gamma lines with different positions and resolutions to a Gaussian mixture (black).

The variance of a distribution $f(x)$ with mean μ is defined as:

$$\sigma^2 = E\left[(x - \mu)^2\right] = E\left[x^2\right] - E\left[x\right]^2.$$ (3.25)

A Gaussian mixture can be expressed as

$$f(x) = \sum_i w_i g(x|\mu_i, \sigma_i),$$ (3.26)

where $g(x|\mu_i, \sigma_i)$ is a normal distribution with mean μ_i and variance σ_i^2, and weights w_i. The moments of the Gaussian mixture can be easily computed:

$$
\begin{aligned}
E[x^{(k)}] &= \int x^{(k)} f(x) \, dx \\
&= \int x^{(k)} \sum_i w_i g(x|\mu_i, \sigma_i) \, dx \\
&= \sum_i w_i \int x^{(k)} g(x|\mu_i, \sigma_i) \, dx \\
E[x] &= \sum_i w_i \mu_i & (3.27) \\
E[x^2] &= \sum_i w_i (\sigma_i^2 + \mu_i^2) & (3.28)
\end{aligned}
$$

The variance of a Gaussian mixture is thus given by:

$$
\sigma^2 = \sum_i w_i \left(\sigma_i^2 + \mu_i^2 \right) - \left(\sum_j w_j \mu_j \right)^2. \tag{3.29}
$$

For a dataset comprised of individual detector partitions, these parameters stand for the individual detector partition's resolution σ_i, and peak position μ_i. The peak positions can be different due to independent systematic effects on the energy scale. The weights are the expected relative event count contributions of individual detectors. For peaks that are proportional to exposure $\mathcal{E}_i = m_i \cdot t_i$, with individual detector's mass m_i and runtime t_i, the relative contribution is:

$$
w_i = \frac{\mathcal{E}_i}{\mathcal{E}}, \tag{3.30}
$$

where $\mathcal{E} = \sum_j \mathcal{E}_j$ is the total exposure of the dataset.

Assuming the positions of the peaks to be the same, i.e., biases in energy scale to be negligible (see Section 3.7), Eq. 3.29 simplifies to:

$$
\sigma = \sqrt{\frac{1}{\mathcal{E}} \sum_i \mathcal{E}_i \sigma_i^2}, \tag{3.31}
$$

with total error δ_σ resulting from the errors of individual detector resolutions δ_{σ_i}:

$$
\delta_\sigma = \sqrt{\frac{1}{\mathcal{E}^2 \sigma^2} \sum_i (\mathcal{E}_i \sigma_i \delta_{\sigma_i})^2}, \tag{3.32}
$$

assuming negligible uncertainty in the weights.

As an example, Fig. 3.25 shows the Gaussian mixture model for two datasets: one for the IC detectors, and one for the Coaxial detectors after the mid-2018 upgrade. Red lines indicate Gaussian shaped peaks for individual detectors partitions, with the resolution taken at $Q_{\beta\beta}$, and the offset

given by the observed deviation of the single escape peak position from literature. These are then weighted by their exposures and summed to give the Gaussian mixture (black line). The blue line is the signal model used to model a peak at $Q_{\beta\beta}$, which is a simple Gaussian with zero offset with the FWHM as given by the effective resolution of the dataset. For the IC detectors, the Gaussian mixture model appears very close to a Gaussian shape, as the offsets are small and the detectors in each dataset have similar resolutions. However, for the Coaxial detectors, the resolution of ANG2 is much worse than the other detectors, and makes the simplifying assumption of a single effective resolution for the dataset ill advised. This motivates the partitioning approach for the $0\nu\beta\beta$ decay search.
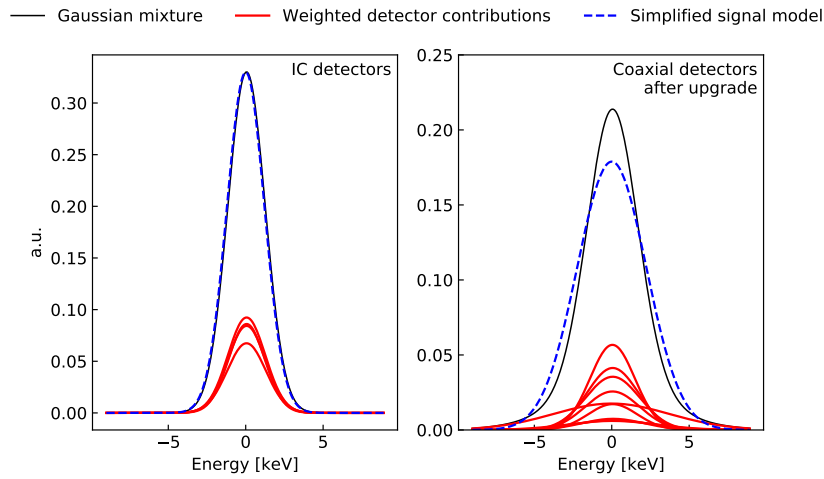
Figure 3.25: Comparison of simplified Gaussian signal model (dashed blue) to the more detailed Gaussian mixture signal model (solid black) for IC detectors (left) and Coaxial datasets before the mid-2018 upgrade (right). Red lines show individual partition's contributions.

To calculate the effective resolution curves, first, the individual detector partition resolutions for lines in their combined calibration spectra are determined as in Section 3.6.1. All lines excluded for the detector partition resolution curves, described in Section 3.6.1, are also excluded here, namely lines below 500 keV, the single- and double-escape peaks, and the summation lines. Additionally, all gamma lines for which not all detectors in a dataset observe that gamma line are excluded.

The remaining detector partition resolutions are combined to form effective resolutions for each dataset according to Eq. 3.31.Their energy dependence is then fitted with the function in Eq. 3.24.

Calculated effective resolution curves for the three detector types and using Eq. 3.31 are shown in Fig. 3.26. The parameters of the function for the different divisions of the datasets are shown in Tab. 3.5, along with the resolution at $Q_{\beta\beta}$.
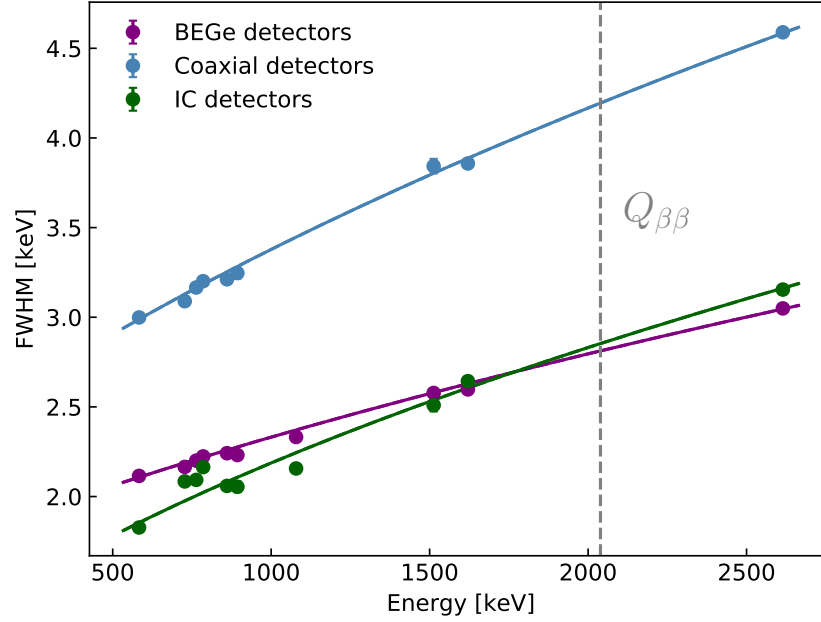
Figure 3.26: Effective resolution curves for the entire Phase II period and the three detector types.

Detector type	Period	a [keV^2]	b [10^{-4} keV]
BEGe	pre upgrade	0.681 ± 0.001	4.27 ± 0.01
	post upgrade	0.363 ± 0.001	4.32 ± 0.01
	all Phase II	0.551 ± 0.001	4.294 ± 0.009
Coaxial	pre upgrade	1.025 ± 0.002	6.47 ± 0.02
	post upgrade	0.898 ± 0.006	20.00 ± 0.06
	all Phase II	0.985 ± 0.002	10.73 ± 0.02
IC	all Phase II	0.280 ± 0.002	5.83 ± 0.02

Table 3.5: Parameters and errors of Eq. 3.24 for the various divisions of the Phase II period and the three detector types.

Weighted average for $0\nu\beta\beta$ decay search

Another application where input resolutions are required is the $0\nu\beta\beta$ decay search. As mentioned before, in earlier GERDA $0\nu\beta\beta$ decay analyses such as [67], partitioning was not performed, and data from multiple detectors was combined to form a dataset for each detector type. In this case, very few events (in fact, only one) are observed close to $Q_{\beta\beta}$, so using a signal model of a Gaussian with an effective resolution as in Section 3.6.2 is not appropriate. Instead, a simple weighted average of the partition resolutions at $Q_{\beta\beta}$ gives the expected resolution to be associated with a single event, i.e.:

$$\sigma = \sum_i w_i \sigma_i, \tag{3.33}$$

where the sum goes over the partitions with standard deviations σ_i and weights w_i. The spread (or here, exposure-weighted standard deviation) in resolutions across the partitions then gives the uncertainty. The resulting resolutions and uncertainties are reported in Table 3.6.

Detector type	Period	FWHM at $Q_{\beta\beta}$ [keV]
BEGe	pre upgrade	2.9 ± 0.3
	post upgrade	2.6 ± 0.2
	all Phase II	2.8 ± 0.3
Coaxial	pre upgrade	3.6 ± 0.3
	post upgrade	4.9 ± 1.9
	all Phase II	4.0 ± 1.3
IC	all Phase II	2.9 ± 0.1

Table 3.6: Energy resolutions at $Q_{\beta\beta}$ (FWHM) for the various divisions of the Phase II period and the three detector types. The uncertainty is given by the exposure weighted standard deviation.

As expected, the BEGe and IC detectors exhibit a better energy resolution than the Coaxial detectors. The Coaxial detectors' effective resolution degraded by 1.3 keV after the mid-2018 upgrade, largely due to the poor resolution of ANG2 (8.8 keV).

3.6.3 *Systematic uncertainties on the resolution at $Q_{\beta\beta}$*

The statistical uncertainty on the energy resolution at $Q_{\beta\beta}$ in Tables 3.4 and 3.5 decreases with rising statistics over time, and is on the order of only a few eV. As such, we are dominated by systematic uncertainties, which require dedicated analyses to study their various sources.

Possible sources of systematic uncertainty in the resolution at $Q_{\beta\beta}$ are considered, given here in decreasing order of their contribution: (i) resolution shifts over time; (ii) energy scale shifts over time; (iii) the choice

of the resolution fitting function.Due to the nature of these uncertainties, their magnitude will not decrease over time (but might change if the detector setup or analysis methods change). The total systematic uncertainty is obtained by quadratically summing individual contributions, thereby assuming no correlations. Table 3.7 lists the obtained contributions to and total uncertainty for each detector partition. In the following sections we explain how individual contributions were determined.

Resolution shifts over time

As seen in the left figures of Fig. 3.18, while partitioning accounts for large (> 0.3 keV) changes in the resolution, there are still variations in the resolution of the 2.6 MeV line among calibrations.

The variation is quantified by the RMS standard deviation in the resolution across a single partition σ_{FEP}, with respect to the partition resolution at 2.6 MeV, as determined from the partition resolution curves described in Section 3.6.1. This is then translated to the energy at $Q_{\beta\beta}$, by rescaling with respect to the resolution at $Q_{\beta\beta}$, $\text{FWHM}_{Q_{\beta\beta}}$:

$$\sigma_{Q_{\beta\beta}} = \frac{\sigma_{\text{FEP}}}{\text{FWHM}_{\text{FEP}}}\text{FWHM}_{Q_{\beta\beta}} \tag{3.34}$$

where $\sigma_{Q_{\beta\beta}}$ is the variation in the resolution at $Q_{\beta\beta}$ and FWHM_{FEP} is the resolution at the 2.6 MeV line.

The chosen method of rescaling is relatively agnostic with respect to the cause of the variation in the resolution. Equation 3.24 can be rewritten as:

$$\text{FWHM} = c\sqrt{d + E}, \tag{3.35}$$

where $c \equiv 2.355\sqrt{b}$ and $d \equiv a/b$. If we assume all changes in the resolution are due to changes in c, and d is constant,

$$\Delta\text{FWHM} = \Delta c\sqrt{d + E} = \frac{\Delta c}{c}\text{FWHM}, \tag{3.36}$$

recovering the relation in Equation 3.34. This assumption is supported by the high degree of correlation between the fit parameters a and b, with an average of -0.81 for the fitted partition resolution curves. Similarly, the MAJORANA collaboration finds a high degree of correlation ~ 1 between $\sqrt{a}$ and b [140]. The distribution of this component of the resolution uncertainty is shown in Figure 3.27. The mean value is 0.11 keV, with a standard deviation of 0.06 keV.

Energy scale shifts over time

Once the energy scale is determined via a calibration, its stability is assumed until the next calibration. Several parameters are monitored to ensure stability (see Section 3.4), but smaller fluctuations of the energy scale

Detector	Partition	Resolution shift [keV]	Pulser shift [keV]	Fitting function [keV]	Total [keV]
ANG1	0	0.07	0.04	0.02	0.09
ANG2	0	0.27	0.21	0.15	0.37
	1	0.18	0.20	0.11	0.29
	2	0.19	0.06	0.11	0.23
	3	0.37	0.05	0.12	0.39
ANG3	0	0.09	0.11	0.05	0.15
	1	0.07	0.11	0.07	0.15
	2	0.06	N/A	0.02	0.06
ANG4	0	0.09	0.17	N/A	0.19
	1	0.09	0.16	N/A	0.18
	2	0.18	0.20	0.05	0.27
	3	0.21	0.13	N/A	0.25
ANG5	0	0.16	0.14	N/A	0.21
GD00A	0	0.09	0.02	0.03	0.10
	1	0.06	0.02	N/A	0.06
GD00B	0	0.10	0.02	N/A	0.10
	1	0.12	0.12	N/A	0.17
GD00C	0	0.05	0.22	N/A	0.22
	1	0.10	0.04	0.06	0.12
	2	0.17	0.04	N/A	0.17
GD00D	0	0.06	0.07	N/A	0.09
	1	0.08	0.03	N/A	0.09
GD02A	0	0.06	0.12	N/A	0.13
	1	0.09	0.10	N/A	0.13
GD02B	0	0.10	0.02	0.04	0.11
	1	0.08	0.04	0.06	0.11
GD02C	0	0.11	0.03	0.10	0.15
	1	0.06	0.03	0.07	0.10
	2	0.07	N/A	0.09	0.12
GD32A	0	0.35	0.04	0.12	0.38
	1	0.08	0.27	N/A	0.28
GD32B	0	0.06	0.08	N/A	0.10
	1	0.08	0.13	N/A	0.16
GD32C	0	0.07	0.07	N/A	0.10
	1	0.07	0.12	N/A	0.14
GD32D	0	0.10	0.02	N/A	0.11
	1	0.06	0.04	N/A	0.07
GD35A	0	0.11	0.08	0.05	0.14
	1	0.09	0.10	N/A	0.13
GD35B	0	0.06	0.03	N/A	0.07

Detector	Partition	Resolution shift [keV]	Pulser shift [keV]	Fitting function [keV]	Total [keV]
	1	0.06	0.06	N/A	0.08
GD35C	0	0.07	0.12	N/A	0.14
	1	0.07	0.05	N/A	0.09
GD61A	0	0.10	0.01	0.06	0.12
	1	0.10	0.06	N/A	0.12
GD61B	0	0.08	0.32	N/A	0.32
	1	0.09	0.10	N/A	0.14
GD61C	0	0.07	0.25	0.02	0.26
	1	0.08	0.06	0.02	0.11
GD76B	0	0.13	0.25	0.03	0.29
	1	0.15	0.04	N/A	0.16
	2	0.17	0.04	N/A	0.17
GD76C	0	0.14	0.11	N/A	0.18
	1	0.08	0.07	0.02	0.11
GD79B	0	0.06	0.02	N/A	0.07
	1	0.06	N/A	N/A	0.06
GD79C	0	0.06	0.04	0.02	0.07
	1	0.12	0.04	0.18	0.22
	2	0.13	0.06	0.15	0.20
GD89A	0	0.07	0.03	0.04	0.09
	1	0.07	0.06	N/A	0.10
GD89B	0	0.08	0.03	0.01	0.08
	1	0.06	0.05	N/A	0.08
GD89C	0	0.06	0.18	N/A	0.19
	1	0.10	0.02	N/A	0.10
GD89D	0	0.08	0.03	N/A	0.09
	1	0.07	0.07	N/A	0.10
GD91A	0	0.07	0.04	N/A	0.08
	1	0.05	0.03	N/A	0.06
GD91B	0	0.16	0.07	0.11	0.21
	1	0.21	0.08	N/A	0.23
GD91C	0	0.18	0.02	N/A	0.18
	1	0.05	0.03	N/A	0.06
GD91D	0	0.07	0.07	N/A	0.10
	1	0.05	0.02	N/A	0.05
IC48A	0	0.06	N/A	N/A	0.06
IC50A	0	0.04	N/A	N/A	0.04
IC50B	0	0.08	N/A	0.05	0.09
IC74A	0	0.09	N/A	0.01	0.09
RG1	0	0.10	0.22	0.01	0.25

Detector	Partition	Resolution shift [keV]	Pulser shift [keV]	Fitting function [keV]	Total [keV]
	1	0.10	0.07	N/A	0.12
	2	0.07	0.06	0.06	0.11
RG2	0	0.16	0.16	0.03	0.23
	1	0.11	0.08	0.10	0.17
	2	0.31	0.07	0.14	0.35

Table 3.7: Contributions to the systematic uncertainty in the resolution at $Q_{\beta\beta}$ for all enriched detectors and partitions. The total uncertainty is given by the sum in quadrature of the three components, from resolution shifts, energy scale shifts, and the choice of resolution curve fitting function.
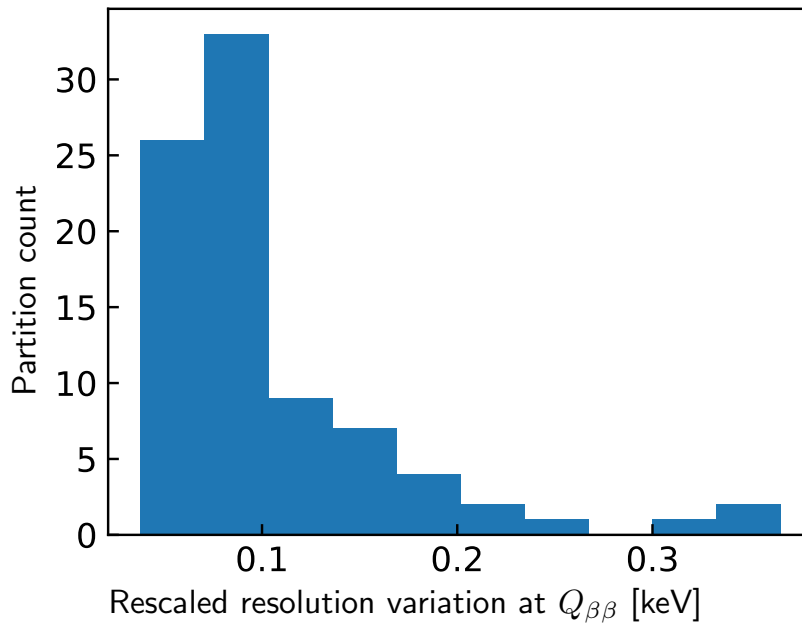
Figure 3.27: Distribution of FWHM uncertainty due to FEP variation per detector partition.

still can deteriorate the resolution for physics data compared to calibration data. Fluctuations on time scales below the typical calibration duration (1.5 h) will be present in the calibration data as well and contribute to the observed resolution in the resulting energy spectrum. However, fluctuations on larger time scales, up to weeks, can add additional uncertainty to the resolution in physics data compared to that obtained from calibration data.

One indicator for gain stability is the pulser position. By evaluating the fluctuations in the pulser position in the time between calibrations, the resulting contribution to the resolution can be estimated.

First, we divide the physics data into periods of 1.5 h, in order to average out fluctuations on time scales below this which are already included in calibration data. This amounts to 270 pulses, as one pulse is injected every 20 s. Additionally, the precision on the average position during each 1.5 h period is improved from about 1 keV for individual pulses to 0.1 keV, enabling sensitivity to fluctuations of this smaller magnitude. Periods where the input pulser itself is unstable are removed, as are periods where a detector does not contribute data to the physics analysis, e.g. it is set to AC mode. 1.5 h periods that do not contain exactly 270 pulser positions are also excluded.

The average pulser position in the first 1.5 h period after a calibration, E_0, is used as a reference point and shifts in the following positions, E_j, are defined as

$$\Delta E_j = E_j - E_0, \tag{3.37}$$

where ΔE_j is the residual with respect to the first pulser position. In Figure 3.28, this is shown for ANG3.
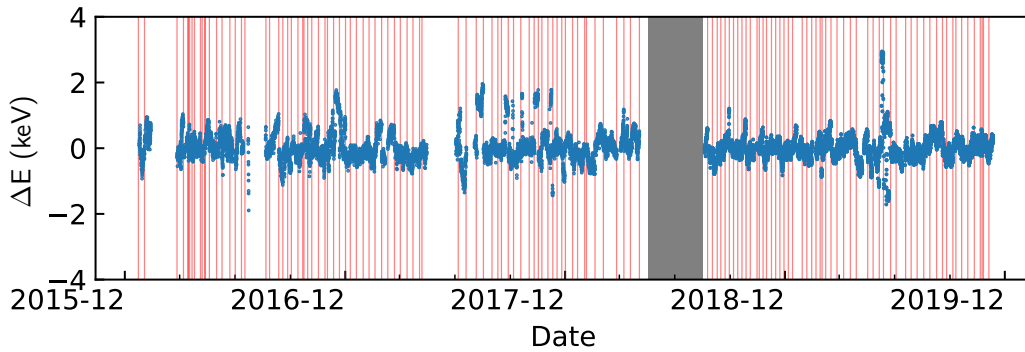
Figure 3.28: Residual of pulser position averaged over 1.5 h periods relative to the first period after a calibration. Calibrations are marked with red vertical lines. The period of the mid-2018 upgrade is indicated in grey.

To statistically evaluate the gain fluctuations we analyse the distribution of the residuals ΔE, normalised by their uncertainty. Were there no energy shifts between calibrations, these standard residuals would be distributed normally. Additional fluctuations beyond this will degrade the resolution and the width of this distribution, and are modelled with an additional uncertainty, σ_i, where i labels the detectors, that is added quadratically to the residuals.

$$\sigma_j \rightarrow \sigma_j' = \sqrt{\sigma_j^2 + \sigma_i^2} \tag{3.38}$$

This is assumed to be constant in time, other than a split before and after the mid-2018 upgrade. This size of this additional uncertainty can be eval-

uated as that required to reduce the standard deviation of the distribution of the standard residuals to one.

Concretely, we define α and σ_i such that

$$\text{std}\left(\frac{\Delta E_j}{\sigma_j}\right) \equiv \alpha \tag{3.39}$$

$$\text{std}\left(\frac{\Delta E_j}{\sigma'_j}\right) \equiv 1. \tag{3.40}$$

To simplify the calculations, the σ_j are replaced by the median value, σ_{med}. Then,

$$\begin{aligned}
\frac{\sigma'}{\sigma_{\text{med}}} &= \alpha \\
\sigma' &= \alpha\sigma_{\text{med}} \\
&= \text{std}\left(\Delta E_j\right).
\end{aligned} \tag{3.41}$$

Equation 3.38 can then be used to find σ_i:

$$\sigma_i^2 = \text{std}\left(\Delta E_j\right)^2 - \sigma_{\text{med}}^2 \tag{3.42}$$

This can equivalently be expressed as

$$\text{std}\left(\Delta E_j\right)^2 = \sigma_{\text{med}}^2 + \sigma_i^2, \tag{3.43}$$

i.e. the total resolution is given by the combination of statistical fluctuations and the additional component accounting for systematic energy shifts.

Determined values for σ_i are typically around 0.2 keV in standard deviation, or around 0.6 keV in FWHM.

To estimate the effect of this additional component to the resolution of a given partition, we evaluate the change in that partition's resolution after the contribution has been added quadratically:

$$\sigma_{\text{sys.}} = \sqrt{\text{FWHM}^2 + (2.355\sigma_i)^2} - \text{FWHM}. \tag{3.44}$$

The mean value for $\sigma_{\text{sys.}}$ is 0.08 keV, with a standard deviation of 0.07 keV.

Choice of resolution function

We use the square root of a linear function to model the resolution as a function of energy (Eq. 3.24). The simplest alternative to this function is to add a quadratic term under the square root:

$$\text{FWHM} = 2.355\sqrt{a + bE + cE^2}, \tag{3.45}$$

where c is bounded to be positive, as would be motivated physically. Both functions describe the data reasonably well between 500 keV and 2.6 MeV, as shown in Figure 3.29.

As an estimate for how much the resolution in $Q_{\beta\beta}$ varies throughout the different reasonable choices of functions for interpolation, we use difference in the values obtained for the two choices, the square root of linear (Eq. 3.24) and quadratic (Eq. 3.45) functions. For 40 of the 85 partitions, the best fit value for c is zero. Of the other partitions, the average difference in the resolution at $Q_{\beta\beta}$ is 0.05 keV, with a standard deviation of 0.05 keV.
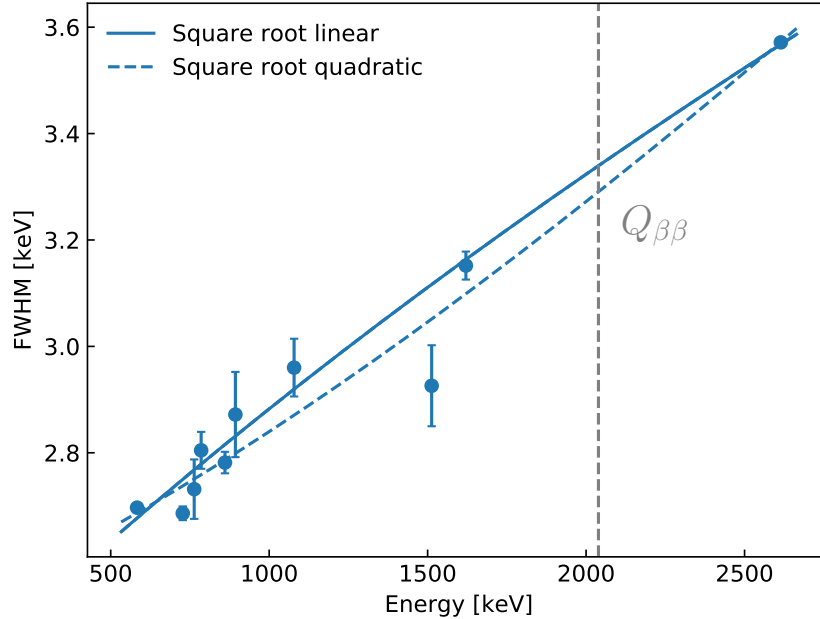
Figure 3.29: The resolution of peaks in combined calibration spectrum for the first partition of ANG3, with square root of linear and quadratic functions fit to them.

3.7 ENERGY BIAS

If we look at a certain event, its reconstructed energy will fluctuate statistically according to the resolution. However, it might also be systematically displaced due to static effects connected to the calibration procedure and assumptions therein. The size of these biases can be estimated by comparing the observed position of gamma lines in physics and calibration data to their literature positions. For calibration data, the statistics in combined calibration spectra are sufficient to reach sub 0.1 keV precision for the peak position.

To evaluate any remaining energy bias after the calibration procedure and quadratic correction, we look at the residual at the SEP, a proxy for events near $Q_{\beta\beta}$. While the average bias for all partitions is centred around 0, the standard deviation among partitions is 0.3 keV, as shown in Figure 3.30a. Since the $0\nu\beta\beta$ decay search is extremely sensitive to the energy of the events falling close to $Q_{\beta\beta}$, it was decided that as part of the sta-

tistical analysis, the energies of events in the region of interest would be corrected by adding the calculated bias.

(a)   **(b)**
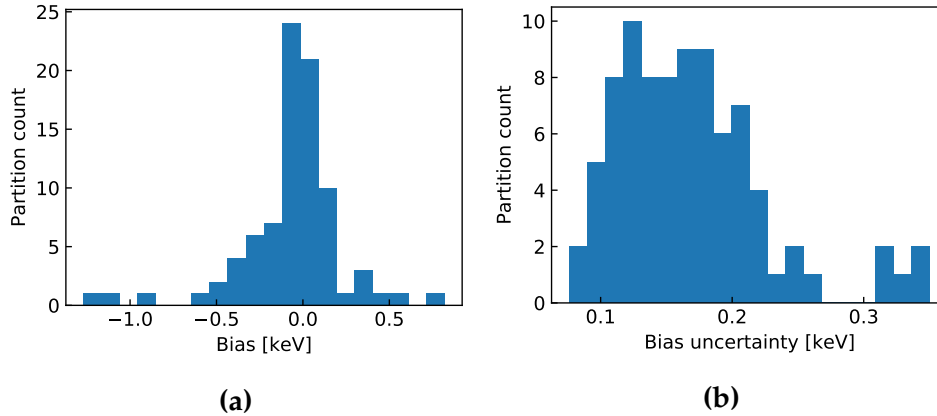
Figure 3.30: Left: observed energy bias at the SEP. Right: energy bias uncertainty.

This approach was justified by studying the ^{42}K peak (at 1525 keV) in the physics data and the DEP (at 1593 keV) in the calibration data, which are two closely located peaks with the former appearing in the physics data and the latter in the calibration data, similar to $Q_{\beta\beta}$ and the SEP. Based on the residual at DEP, one can correct for the energies of the events in the ^{42}K peak. This is shown in Figure 3.31. This correction reduces the mean residual at the ^{42}K line from -0.14 keV to 0.01 keV.
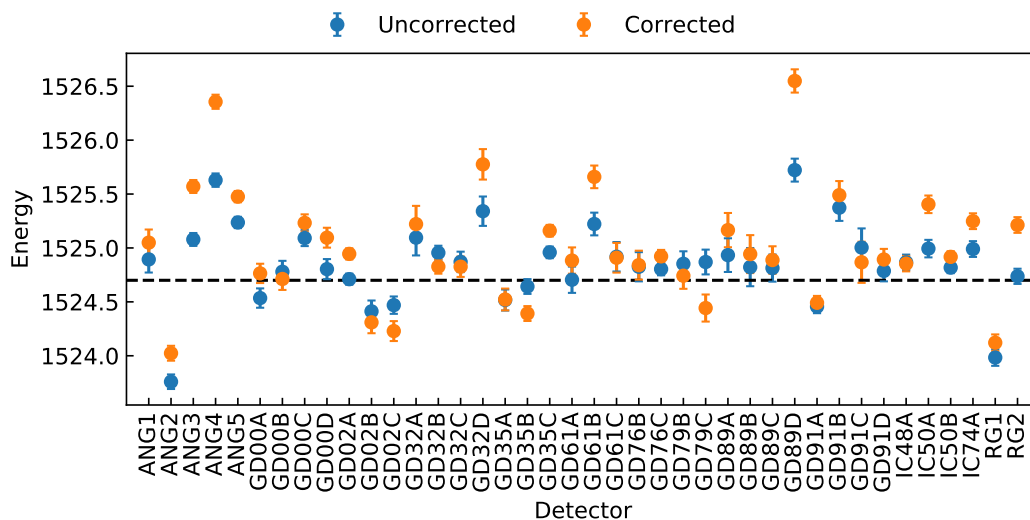
Figure 3.31: The position of the potassium lines before (blue) and after (orange) a correction is applied based on the residual at the DEP. The dashed black line indicates the literature position of the DEP.

For the energy reconstruction uncertainty, we consider the fluctuations in the residual of the SEP over time. The variation is quantified by the RMS

standard deviation in the residual at the SEP across a single partition, with respect to the partition residual at the SEP in the combined spectrum (see Section 3.5.2).

In addition, we add a systematic uncertainty of 0.02 keV accounting for the difference between the bias at the energy at the SEP and that at $Q_{\beta\beta}$. This was roughly evaluated by linearly interpolating between the mean residuals across all partitions at the DEP and the SEP. This is shown in Figure 3.32a.

(a)　　　　　　　　　　(b)
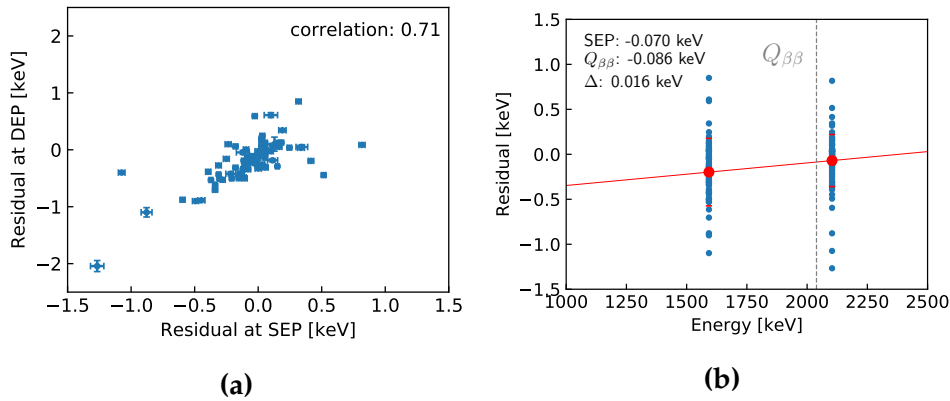
Figure 3.32: Left: correlation of bias between SEP and DEP. Right: interpolating residuals between DEP and SEP.

The distribution of the energy reconstruction uncertainty per partition is shown in Figure 3.30b.

3.8   COMPARISON WITH RESOLUTIONS IN PHYSICS DATA

The two strongest gamma lines in our physics data spectrum are those due to ^{40}K (1461 keV) and ^{42}K (1524 keV) decays, as shown in Figure 2.9. The measured resolution of these lines allows for a cross-check to those derived from calibration data (see Sect. 3.6.1). For every detector and partition, the energy spectrum around each line is fitted using a Gaussian for the signal and a linear function for the background. The background rate was constrained to be non-negative across the fitting window. Lines with low counting statistics, i.e. those whose best fit is compatible with zero counts, are excluded from further analysis.

Given their close energy proximity, the extracted resolution for each of the two lines is expected to be within 0.05 keV of each other. Indeed, the distribution in the resolution difference between the two lines across the detectors in keV, normalised by the uncertainty in keV, was found to have a mean of -0.07 ± 0.14 and a standard deviation of 1.29 ± 0.14, suggesting that only small systematic effects remain. The comparison is shown in Figure 3.33.
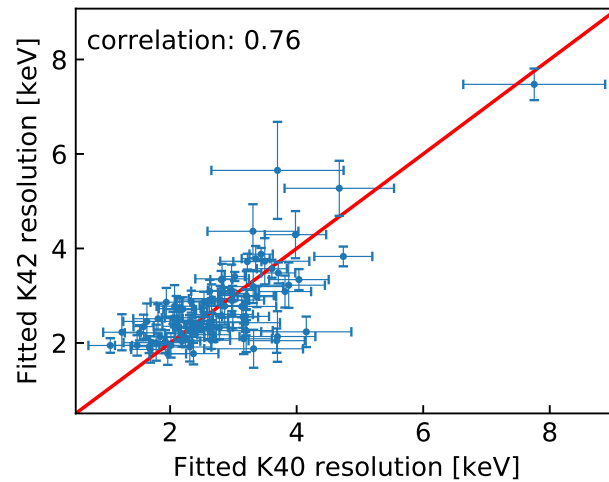
Figure 3.33: Comparison of the measured resolutions of the ^{40}K and ^{42}K lines.

The comparison between calibration and physics data for the higher-statistics ^{42}K line is shown in Fig. 3.34a. The systematic uncertainty for the calibration resolution is calculated in the same way as for as in Sect. 3.6.3. The measured resolutions and predicted values from calibration data show a high degree of correlation, with a Pearson correlation coefficient of 0.92, and with 66% compatible within one sigma. Similar results are obtained for the ^{40}K line.

(a)   (b)
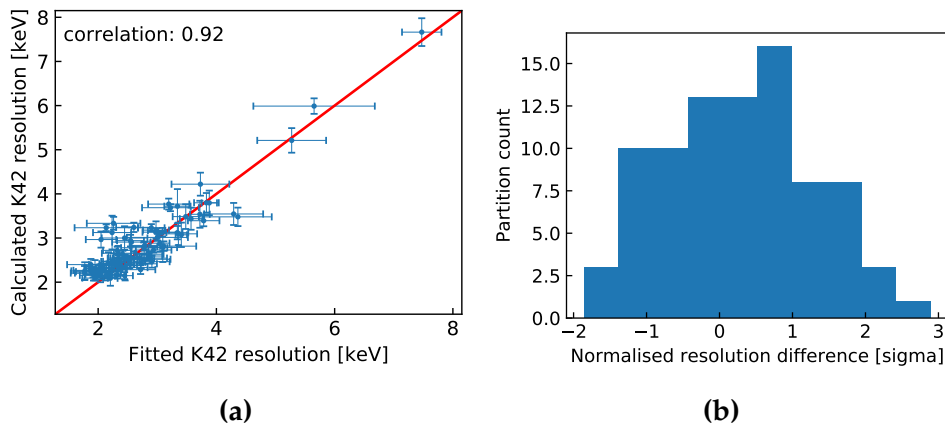
Figure 3.34: Left: measured resolutions of the ^{42}K line compared to predicted resolutions from calibration data. Right: distribution of the difference in measured and predicted resolutions, normalised by uncertainty.

3.9 CONCLUSION

A reliable and stable energy scale is crucial to all physics analyses performed with the GERDA experiment. The germanium detectors are cali-

brated weekly using ^{228}Th sources. The energy scale is then determined by identifying γ peaks in the recorded spectrum the energy scale. Between December 2015 and November 2019, 142 calibrations were analysed to provide energy estimates to events.

For each calibration, the stability of the energy scale and resolution is monitored via the FEP line from ^{208}Tl decays. Based on the stability of the energy scale and resolution, the detectors' data is divided into stable sub-periods called partitions.

For each partition, a combined calibration spectrum is produced to determine the energy dependence of the resolution. Over the entire Phase II, we obtain exposure-weighted average resolutions at $Q_{\beta\beta}$ for the BEGe/-Coaxial/IC detectors of (2.8 ± 0.3) keV, (4.0 ± 1.3) keV and (2.9 ± 0.1) keV respectively. Dedicated studies were performed to study various sources of systematic uncertainties to the resolution at $Q_{\beta\beta}$. The average total systematic uncertainty across all partitions is 0.13 keV.

Alternatively, effective resolution curves for modelling the signal due to combined datasets can be calculated by considering the signal as a Gaussian mixture.

The energy bias for the events near $Q_{\beta\beta}$ is estimated and corrected based on the residual of the SEP. The average bias is -0.1 keV with a standard deviation of 0.3 keV. The average uncertainty of these biases is 0.2 keV.

The energy scale, partitioning, resolutions and uncertainties discussed in this paper are essential in the search for $0\nu\beta\beta$ decay with GERDA described in [88].

THE LEGEND EXPERIMENT

The LEGEND (Large Enriched Germanium Experiment for Neutrinoless $\beta\beta$ Decay) collaboration has been formed with the aim of building the next generation of germanium based $0\nu\beta\beta$ decay experiments [84]. The collaboration was formed in October 2016, and will benefit from the combined experience of the GERDA and MAJORANA collaborations, as well as other groups. The proposed experimental program is divided into stages, with a 200 kg array (LEGEND-200) currently under construction, and an ultimate plan of building a ton-scale ^{76}Ge $0\nu\beta\beta$ decay experiment (LEGEND-1000).

The goal is to operate close to the background-free regime, reaching a half-life sensitivity of 10^{27} yr with LEGEND-200, and 10^{28} yr with LEGEND-1000. In both cases the sensitivity refers to both for setting a 90% C.L. half-life limit as well as for discovery of $0\nu\beta\beta$ decay defined as a 50% chance for a signal at 3σ significance [84].

LEGEND-200 will reuse much of the existing infrastructure of GERDA at LNGS, and uses the same general approach, operating the germanium detectors directly in LAr which is instrumented as an active veto. It will reach its sensitivity goal with an exposure of 1 t · yr and background index of 0.6 cts/(FWHM·t·yr). In turn, LEGEND-1000 aims to achieve an exposure above 10 t · yr and an even lower background of 0.03 cts/(FWHM·t·yr) [68]. The dependence of the sensitivity with exposure and background rate is shown in Figure 1.8. In comparison, GERDA reached a background of 1.5 cts/(FWHM·t·yr) in the IC detectors, and MAJORANA reached a background level of 4.0 cts/(FWHM·t·yr). Figure 4.1 shows the projected background contributions of both phases of LEGEND.

4.1 LEGEND-200

In February 2020 the use of the GERDA infrastructure was handed over to the LEGEND collaboration, and the commissioning of LEGEND-200 is now underway. Physics data taking should begin in mid-2021, and a run time of about 5 years is envisaged to reach the target exposure of 1 t · yr. To reach the targeted 200 kg of enriched detectors, the GERDA cryostat will be instrumented with 14 strings, each containing approximately seven to ten germanium detectors, arranged radially as shown in Figure 4.2a. To accommodate the longer strings, a new lock system is being produced. The 30 BEGe detectors (20.0 kg), and 5 IC detectors (9.5 kg) of GERDA and the 35 p-type point contact (PPC) [142] detectors of MAJORANA (29.7 kg) will be
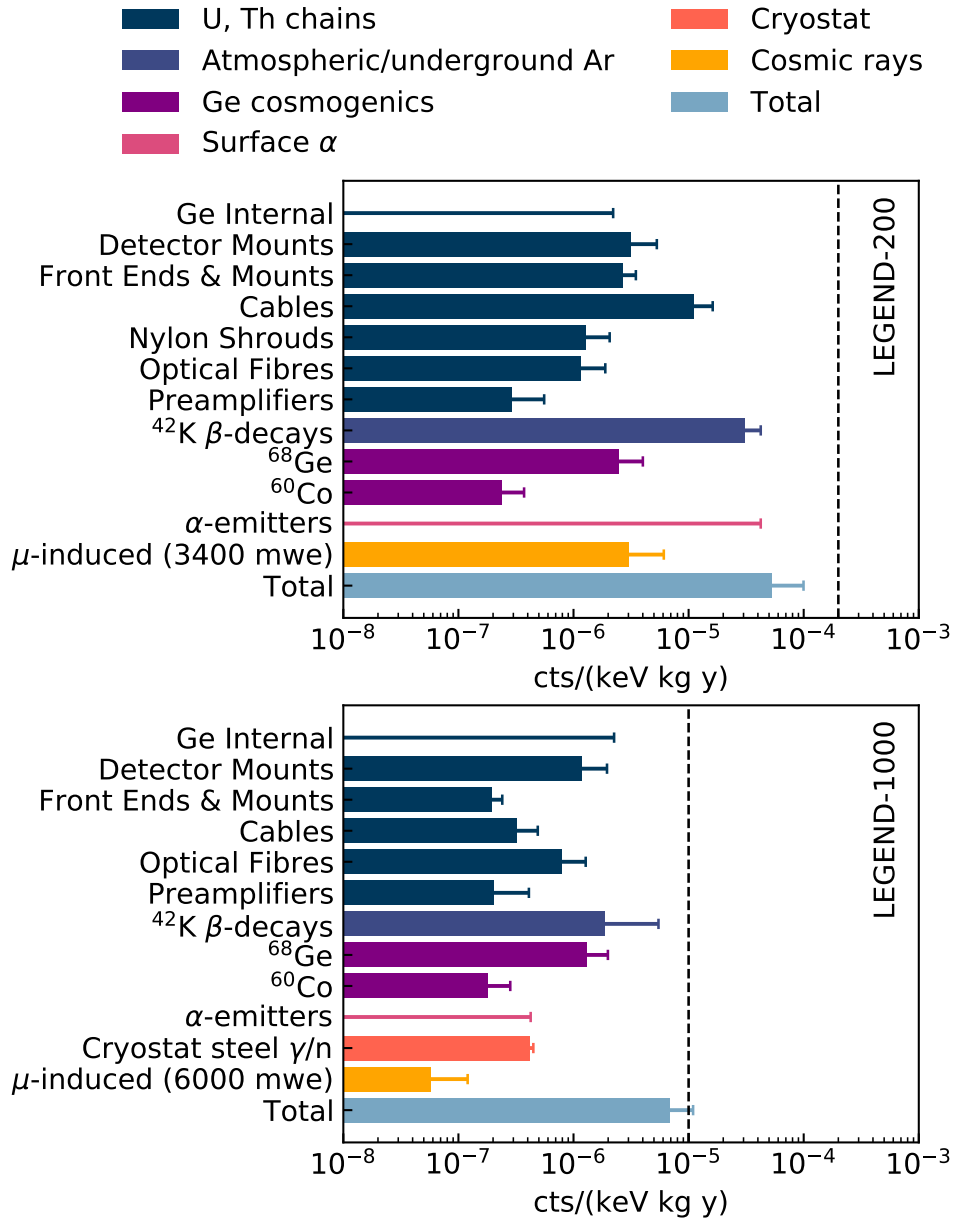
Figure 4.1: Projected background contributions at $Q_{\beta\beta}$ for LEGEND-200 (top) and LEGEND-1000 (bottom). The dashed black line indicates the background goals in both cases. Data from [141].

reused. The Coaxial detectors of GERDA may either be reused or recycled, and are estimated to contribute 11.2 kg.

The remaining ~130 kg of detectors will be IC detectors produced for LEGEND-200 by two detector vendors, ORTEC and Mirion. Current projections suggest that a total of around 140 kg to 150 kg of detectors will be ready for mounting in LEGEND-200 in 2021. The remaining detectors will be mounted later.

(a) Top view (not to scale).

(b) Cutaway view of LAr veto. The copper shroud is not shown.
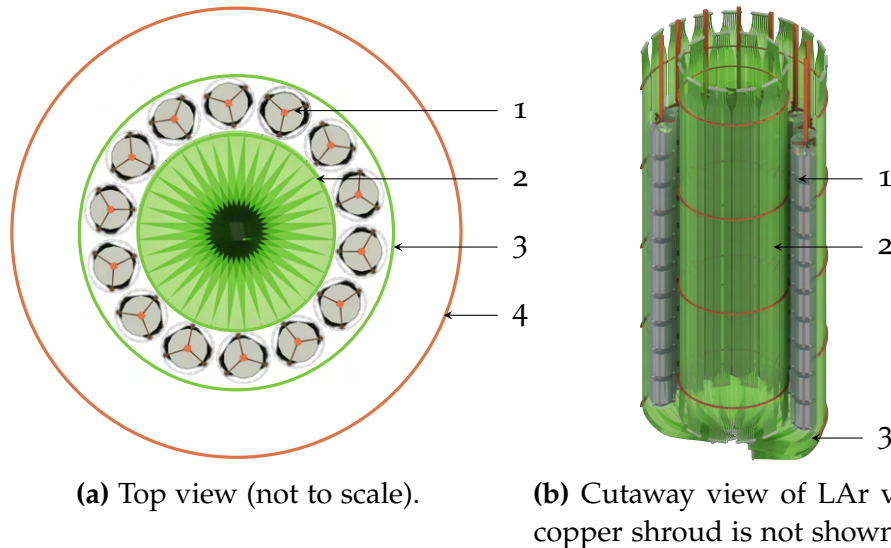
Figure 4.2: The LEGEND-200 detector array and LAr veto. The 14 detector strings (1) are arranged radially. Inner (2) and outer (3) fibre shrouds are coupled to SiPMs to read out LAr scintillation light. An outer copper shroud (4) acts as a WLS reflector. Figures adapted from [143].

In addition to the excellent resolution and PSD performance of the IC detectors, their higher mass reduces the total number of detectors needed. This in turn reduces the requirement for nearby material that contributes to the background.

The sensitivity goals of LEGEND-200 require a ~4-fold reduction in the background rate, compared to GERDA.

Despite the lack of an internal active veto system, the MAJORANA DEMONSTRATOR achieved a low background through careful selection of materials close to the detectors, such as the use of underground electroformed copper [144]. Building on this experience, radiopure low mass crystal holders will be produced for the detectors, using electroformed copper and base plates made of polyethylene naphthalate (PEN) [145]. PEN is a scintillating plastic, allowing background events originating in the plate to be rejected by the LAr veto. New TPB-coated nylon mini-shrouds are also being produced. Radioimpurities will also be reduced by producing new lower mass cables, connectors and other components.

A new liquid argon veto system is being developed, consisting of an outer and inner optical fibre shroud, and an outer electroformed copper

shroud, as shown in Figure 4.2b. The copper shroud is lined with TPB coated Tetratex, and acts as a WLS reflector. The outer fibre shroud curves under the detector strings to increase the efficiency of the LAr veto, and is read out by SiPMs on both ends of the fibres. The inner fibre shroud cannot be read out at both ends of the fibres due to the activity of the SiPMs structure and cabling, so each fibre bends 180° at the bottom and is only read out at the top.

MAJORANA reached the milestone of the best resolution in the field of (2.53 ± 0.08) keV (FWHM at $Q_{\beta\beta}$) [146], through the development of low noise readout electronics [147, 148]. The readout electronics design for LEGEND-200 will be a hybrid design of the MAJORANA front end boards close to the detectors, and the GERDA preamplifiers, located 33 cm away from the top detectors. Low noise will result in improved PSD power and energy resolution.
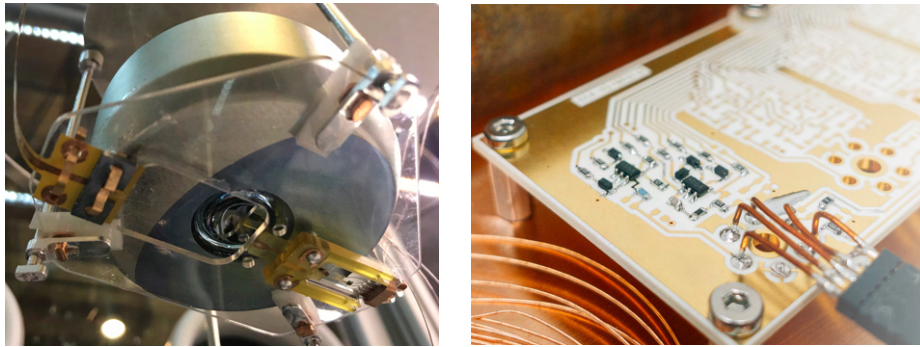
Figure 4.3: Readout electronics for LEGEND-200. Left: Prototype detector mount with BEGe detector and front end board. Right: Prototype preamplifier. Figures from [149].

After the transfer of the GERDA infrastructure to LEGEND in February, a series of R&D activities for LEGEND, the post-GERDA tests (PGT), took place, and were completed in August. Four detector strings, including BEGe and IC detectors from GERDA, PPC detectors from MAJORANA, and new IC detectors from ORTEC and Mirion, were installed using the new LEGEND-200 holders, shown in Figure 4.4.

The electronics chain for GERDA was disassembled and replaced, including the high-voltage modules and cables for biasing the detectors, and the readout electronics (preamplifiers, front end boards and digitisers). A new Source Insertion System (SIS), able to deploy multiple sources at once was also successfully tested. This system is described in more detail in Section 5.1.1. Both background and calibration (shown in Figure 4.4) data was taken.
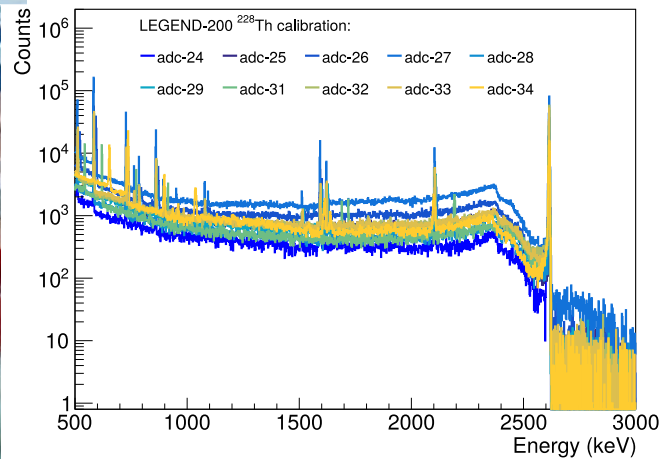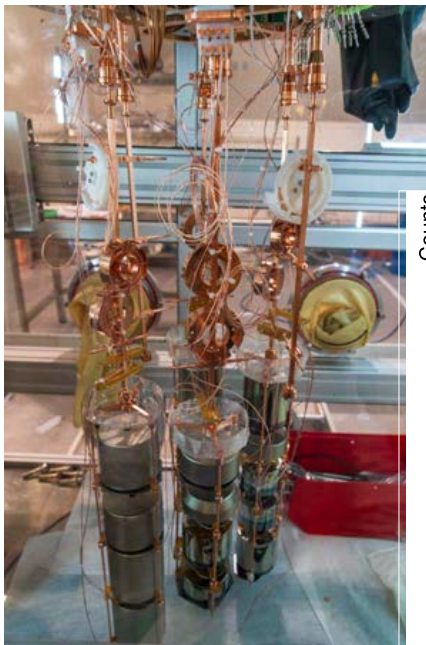
Figure 4.4: Left: four detector strings deployed as part of the PGT. Right: ^{228}Th calibration spectra acquired during the PGT.

4.2 LEGEND-1000

The second stage of LEGEND, LEGEND-1000 will operate about 1 t of germanium detectors for a run time of about 10 yr to reach the target exposure of 10 t · yr. After a site is chosen, and funding is secured, the earliest start date of LEGEND-1000 would be in 2026. In order to start data taking as soon as possible, the detectors would be installed in four independent 250 kg modules, as shown in Figure 4.5. The modular approach would allow for uninterrupted data taking of the already installed modules. Although not required to reach the background aim of LEGEND-1000, the development of even larger detectors, with double the mass of the LEGEND-200 detectors, would mean fewer detectors are needed in total, and therefore also less background-contributing material.

The ambitious goal of LEGEND-1000 is to achieve close to background-free conditions with a background index of 0.03 cts/(FWHM·t·yr). To achieve this, LEGEND may have to move to a site deeper than LNGS to reduce the backgrounds caused by activation via cosmogenic muons, such as ^{77m}Ge, although the location has not yet been determined. Possible sites include the Sanford Underground research Facility (SURF) [150], SNOLAB [151, 152] and China JinPing Laboratory (CJPL) [153]. A delayed coincidence cut exploiting the short half-life (53.7 s) of ^{77m}Ge may reduce this background to the point where locating LEGEND-1000 at LNGS can still reach the background requirements [154].

Contributions due to natural radioactivity will be minimised by increasing the efficiency of the LAr veto, perhaps by doping the argon with small concentrations of xenon [155]. The LAr itself may be replaced by depleted argon obtained from underground sources [156], eliminating the contribution due to ^{42}K decays. This would also allow a lower energy threshold
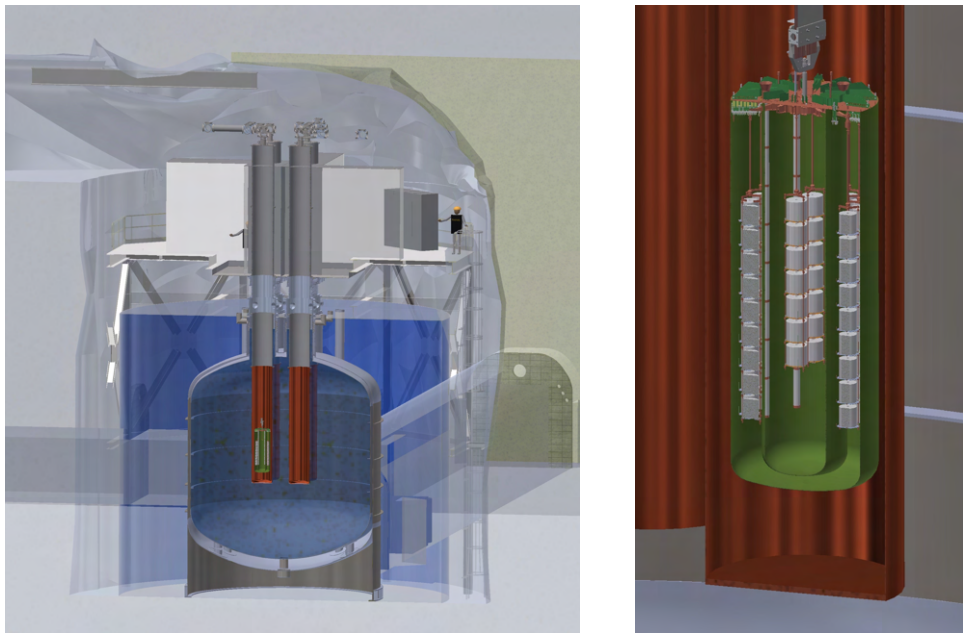
Figure 4.5: Baseline design for LEGEND-1000. Four modules of about 250 kg are contained in a large LAr cryostat (left). Each module consisting of a detector array and LAr veto instrumentation (right) is self-contained by a copper cylinder containing underground LAr. From [68].

and thus low energy physics searches for solar axions, bosonic dark matter and others, as were made using the MAJORANA DEMONSTRATOR [140].

Material selection and minimisation would continue to play a role. Inactive materials could be replaced with PEN as with the detector base plates of LEGEND-200.

MONTE-CARLO SIMULATIONS FOR THE LEGEND-200 CALIBRATION SYSTEM

5.1 INTRODUCTION

For LEGEND-200, as was the case for GERDA, regular calibrations of the germanium detectors and liquid argon veto system with radioactive sources will be necessary. As the LEGEND-200 experiment will operate in the GERDA cryostat, an approach similar to that of GERDA can be taken to expose the germanium detectors to sources. However, the increased number of detector strings relative to GERDA, required in order to reach the targeted 200 kg of enriched germanium detectors, entails an increased number of calibration sources.

The calibration work for LEGEND is primarily performed by the UZH and Los Alamos National Laboratory (LANL) groups.

The rest of this section outlines the current design of the calibration system for LEGEND-200. Section 5.2 describes the goals of the simulations performed, and Section 5.3 describes how the geometry was implemented and the simulations performed. Section 5.4 describes the conclusions drawn from the simulations.

5.1.1 *Calibration system design*

The altered geometry of LEGEND-200 as described in Section 4.1 will require a total of four Source Insertion Systems (SIS), i.e., an increase by one relative to GERDA, to adequately expose the detectors such that enough events are gathered for a precise energy calibration in a reasonable period of time.

A calibration system has to fit in the overall detailed design which determines entry ports, available pathways, and the storage location. The locations of the LAr veto and the detector electronics fixes the possible radius of the sources at 150 mm from the centre of the detector array, as shown in Figure 5.3. In addition, the longer strings of LEGEND-200 relative to GERDA (up to 90 cm [157] compared to GERDA's 40 cm) require a taller lock system to be installed. This has reduced the amount of vertical space available for the SIS. For reference, the SIS for GERDA (developed at UZH) is briefly described in Section 3.2.2.

For LEGEND-200 the SIS design has been modified to accommodate multiple sources attached to each steel band, as shown in Figure 5.1. This is achieved by spot welding adaptors on the steel band, into which the source capsules themselves can be mounted, as shown in Figure 5.2 (technical
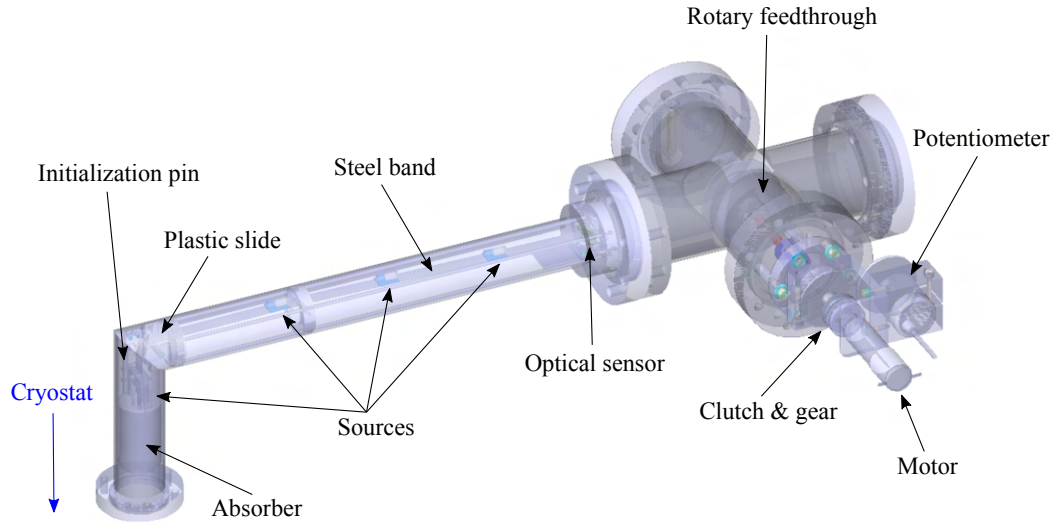
Figure 5.1: The design of the calibration source insertion system for LEG-END-200. The sources are lowered down to the levels of the detectors by the steel band when a calibration is performed.

drawings of the steel band, adaptors and source capsules can be found in Appendix A). This will permit multiple detectors to be calibrated simultaneously, decreasing the amount of time required for calibrations.

Software has been developed jointly between UZH and INFN, to remotely control the deployment of the SIS, and enable exactly reproducible calibrations. In contrast, the GERDA SIS control system required the manual triggering of each source movement via a LabView interface.

5.1.2 *Calibration sources*

Both GERDA and MAJORANA have used ^{228}Th sources as the standard calibration source with source activities between 10 kBq to 20 kBq. As discussed in Section 3.2.1, ^{228}Th has many beneficial properties, including its wide range of γ rays covering $Q_{\beta\beta}$ and convenient single- and double-escape peaks with differing event topologies. For LEGEND-200 energy calibrations, ^{228}Th will be used as the standard source, produced at LANL following the custom design developed at UZH for GERDA [158]. Sources composed of different isotopes, such as ^{226}Ra, may be used to calibrate the energy scale below 235 keV (the lowest observable peak of ^{228}Th) to enable physics searches reliant on an accurate energy scale in the low energy region.

By tuning activity and distribution of the source material in the calibration assembly, we aim to calibrate the detector array within a few hours. Ideally, the activity of the source would be as high as possible to perform calibrations as quickly as possible, resulting in only a small loss of run time
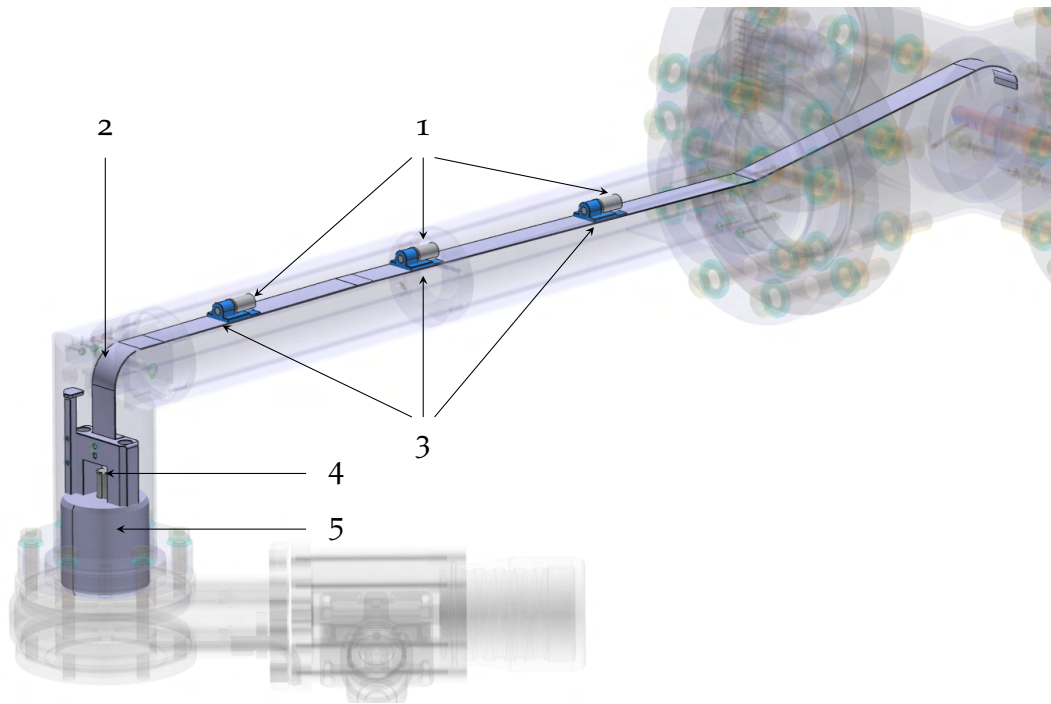
Figure 5.2: Three source capsules (1) are attached to a steel band (2) via adapters (3) spot-welded onto the steel band. The last (4) is attached to a tantalum absorber (5).

for physics data. A precise calibration would require that the uncertainty on the position of peaks is not limited by statistics. In Section 3.7, residual biases and associated uncertainty were both determined to be on the order of 0.1 keV. For a peak with a FWHM of 3 keV, and assuming a purely Gaussian shape, an energy precision of 0.09 keV could be reached with 200 events.

Two limitations prevent the use of high activity sources: the data acquisition system (DAQ) and signal readout. The DAQ is designed such that six detector channels are read out via one digitiser card, each of which can accommodate 1000 Hz at one time with a dead time of 0.1%. A high count rate can also result in events that sit on a baseline that has not been completely restored after the previous event (a pile-up event). The recovery of the baseline is limited by the decay constant of the preamplifier which is around 1 ms. In order to guarantee that the majority of events start after the baseline has settled, a rate of less than 300 Hz per detector is favourable.

5.2 GOALS OF THE MC SIMULATIONS

Some parameters of the calibration system, such as the source type, and the radius at which they can be deployed, can be determined a priori considering the experimental requirements. However, more detailed studies with Monte Carlo (MC) simulations are required to determine the optimal

- number of sources,

- their activities,

- their separation on the steel band, and

- number and location of stopping points by the germanium detectors.

From these parameters, the minimum time required to perform a precise energy scale determination within the constraints set by the DAQ can thus be calculated, as described in Section 5.4.2. MC simulations can also determine the number of events that will be observed in the double escape peak (DEP) of ^{208}Tl, which is used for the optimisation of PSD cuts. The distribution of the events in the detectors can also be studied.

5.3   GEOMETRY IMPLEMENTATION AND SIMULATIONS

The GERDA, MAJORANA and LEGEND collaborations perform simulations using the MaGe [159] framework, based on Geant4 [160].

The implementation of the detector is shown in Figure 5.3. 14 strings, each of which has eight detector units, arranged radially at a distance of 235 mm from the centre. For these initial simulations, the detectors are all identical IC type detectors, as shown in Figure 5.4. Future simulations will require the implementation of a more realistic geometry, including the arrangement of the existing BEGe and PPC detectors.
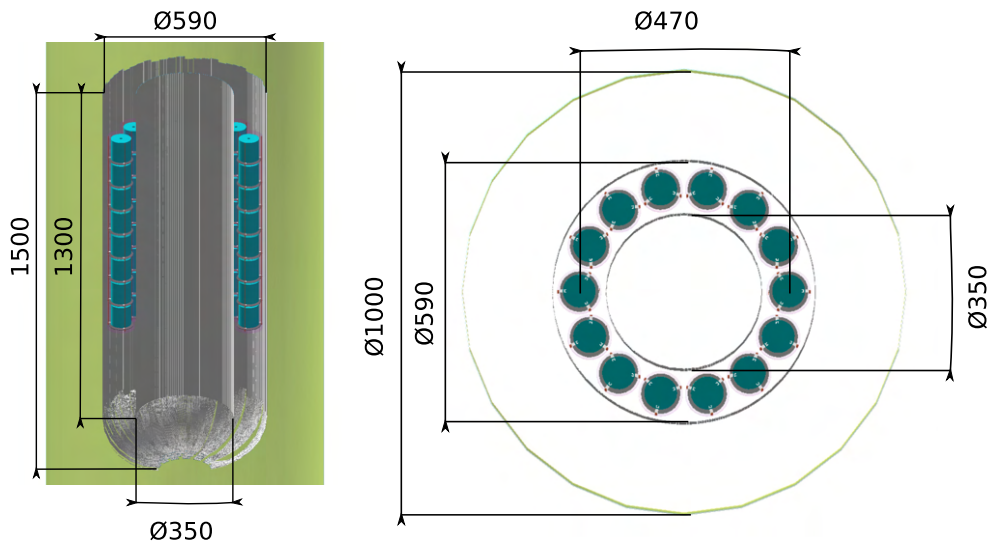
Figure 5.3: The Geant4 implementation of the LEGEND-200 geometry. The left figure shows a side cutaway view of the experiment, with detector strings (cyan) surrounded by nylon mini-shrouds (pink). The inner and outer fibre shrouds are in grey, with the WLS reflector in green. The right figure shows a top view. Dimensions are given in mm.
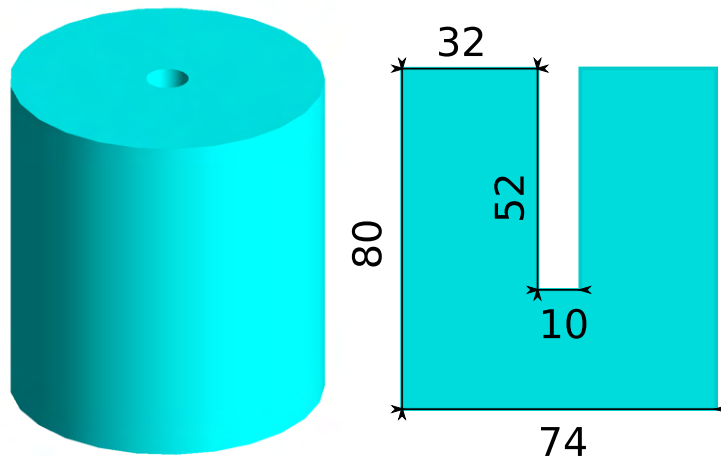
Figure 5.4: The Geant4 implementation of the ideal LEGEND-200 IC detector, in solid (left) and cutaway (right) views. Dimensions are given in mm.

The calibration source is implemented in three parts, as shown in Figure 5.5. During a simulated calibration, ^{228}Th nuclei decay uniformly within the inner gold volume.
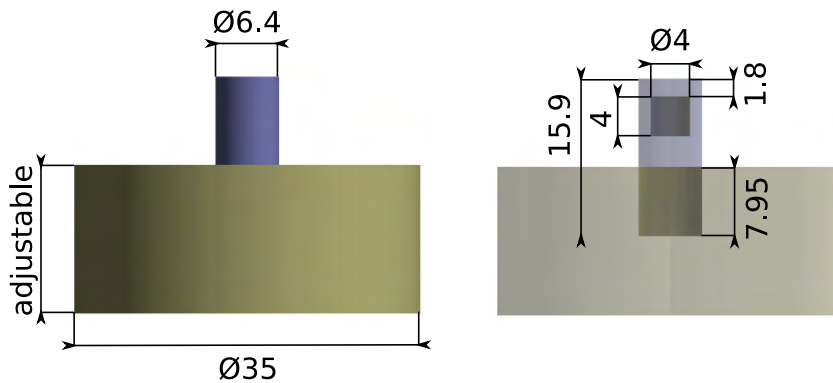
Figure 5.5: The Geant4 implementation of the LEGEND-200 calibration source, in solid (left) and transparent (right) views. The source is composed of the inner gold foil (grey), outer steel encapsulation (blue), and a tantalum absorber (gold). ^{228}Th nuclei decays are simulated uniformly within the inner gold volume. Dimensions are given in mm. When configurating the simulation, one can adjust the height of the absorber, or remove it entirely (see Section 5.4.1).

In Figure 5.6, the four proposed source positions are shown, just within the inner fibre shroud. The four-fold symmetry can be exploited to reduce the number of simulations to only the positions at S1 and S2.

From here onwards, source heights are given with respect to the centre of the topmost detectors. Simulations were performed at source positions S1 and S2 and vertical heights ranging from -1250 mm to 300 mm in increments of 10 mm with respect to the centre of the topmost detectors (i.e. 156 heights in total), with $5 \cdot 10^5$ events per height and source position. Each
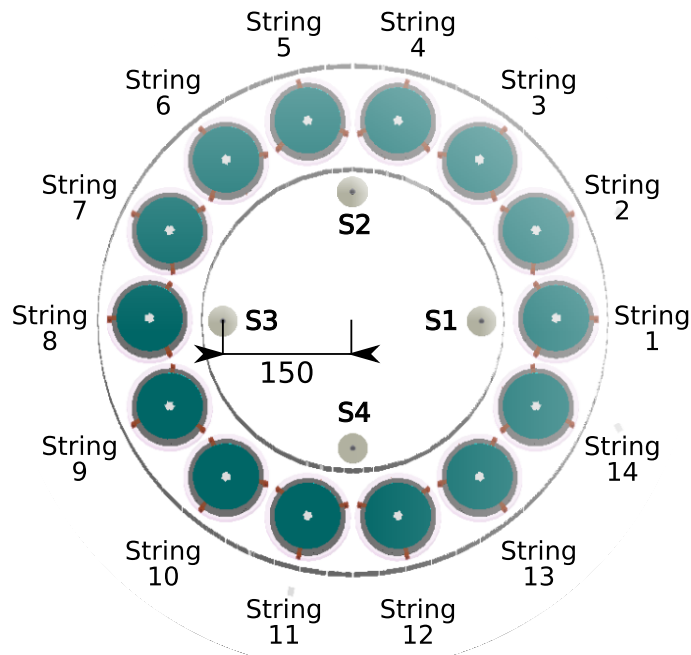
Figure 5.6: Top view of the 14 detector strings and four calibration source positions S1-S4. Dimensions are given in mm.

event is then processed to sum the energy deposits in each detector. In addition, for each event and detector, the location of the first energy deposit is saved. Figure 5.7 shows the distribution of the first energy deposit of each event for a simulation with a source located in position 2 at a height of $-360\,\mathrm{mm}$.
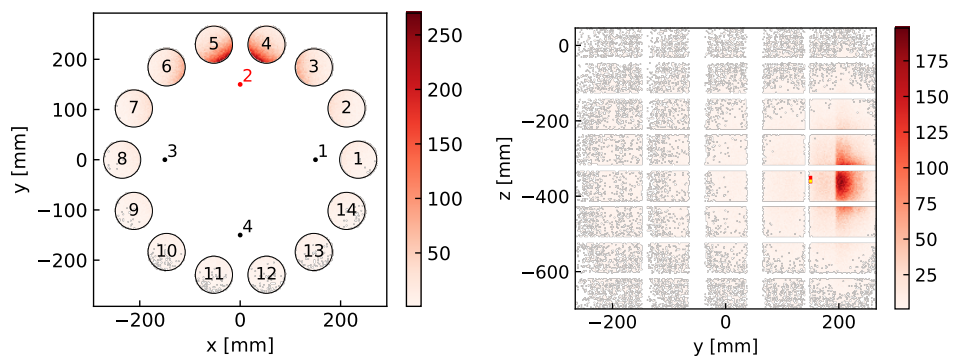
Figure 5.7: Distribution of energy deposits for a source located at position 2 and at a height of $-360\,\mathrm{mm}$. For visualisation purposes, this particular simulation was performed with 10 times the standard statistics. The colour scale indicates the number of events in each bin.

Following the procedure in [134], to model the detector response, including a finite energy resolution and a low-energy tail modelling the effects

of ballistic deficit or incomplete charge collection, the energies are smeared according to:

$$E \rightarrow E + \Delta E, \tag{5.1}$$

where E is the initial event energy, and ΔE is generated randomly. With 97% probability, ΔE is drawn from a Gaussian function, with a mean of zero and a FWHM given by the resolution curve determined for the IC detectors in Section 3.6.2,

$$\mathrm{FWHM}(E) = 2.355\,\sigma = 2.355\sqrt{a + bE}, \tag{5.2}$$

where $a = 0.280\,\mathrm{keV}^2$ and $b = 5.83 \cdot 10^{-4}\,\mathrm{keV}$. With 3% probability, ΔE is drawn from a function f describing a low energy tail as in Eq. 3.17, with parameters defined by the average of those for the tail of the 2.6 MeV line in the combined GERDA Phase II IC detectors spectra:

$$f(\Delta E) = \exp\left(\frac{\Delta E}{\beta} + \frac{\sigma_{\mathrm{FEP}}^2}{2\beta^2}\right) \mathrm{erfc}\left(\frac{\Delta E}{\sqrt{2}\sigma_{\mathrm{FEP}}} + \frac{\sigma_{\mathrm{FEP}}}{\sqrt{2}\beta}\right), \tag{5.3}$$

where σ_{FEP} is determined from Eq. 5.2 with $E = 2614.5\,\mathrm{keV}$, and $\beta = 2.66\,\mathrm{keV}$.

Figure 5.8 shows both the smeared energy spectra for all detectors and the smeared energy spectrum with the greatest number of events in a single detector, with Figure 5.9 showing the same data zoomed into the regions around the FEP, SEP and DEP. These results are from the same simulation used to generate data shown in Figure 5.7.

5.4 DISCUSSION

For each source position and each detector, the following was calculated: the number of total events, the number of events above 200 keV (an approximate energy threshold to calculate event rates), and the total number of events within 0.1 keV of the energies of the FEP and DEP respectively. Uncertainties are purely statistical and are calculated assuming Poissonian statistics.

5.4.1 *Source separation*

Figure 5.10 shows the rates of events above 200 keV for a single 5 kBq source in either positions 1 or 2, in detectors in the closest string (string 1 for position 1, and string 4 for position 2). As to be expected, the event rate in each detector is maximised when the centres of the inner sources and detector align.

If the SIS lowers four sources at a time, the eight detectors of the string can be calibrated by holding the source assembly at two different positions.
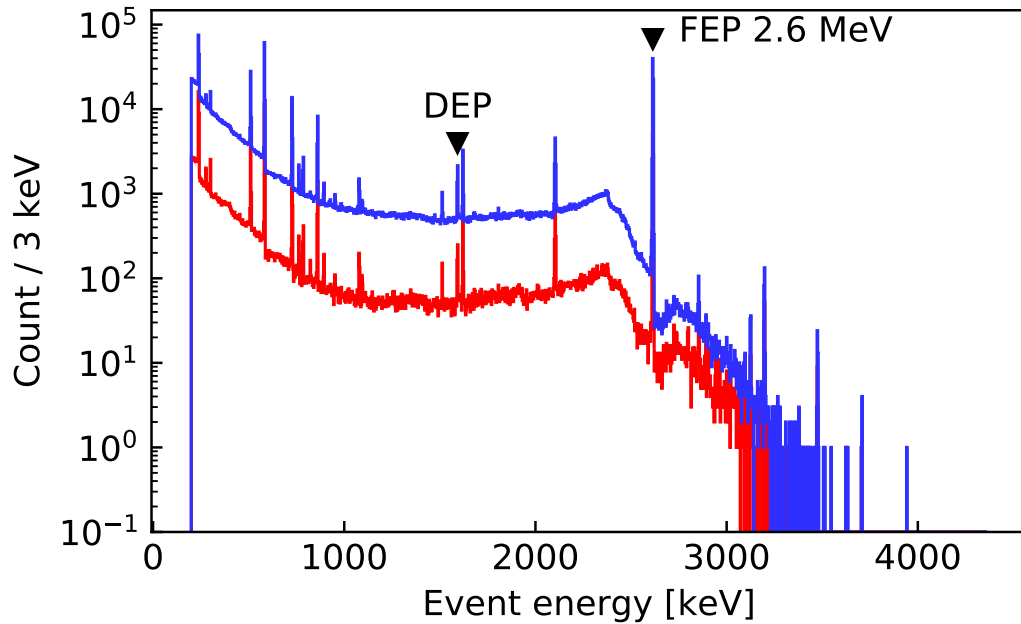
Figure 5.8: Summed energy spectrum for all detectors (blue) and the 5th detector in string 4 (red), with prominent γ lines labelled.

The ideal separation between the sources is then given by the spacing between the centres of the detector units, 10 cm.

The bottommost source lowered by the SIS is not attached to the steel band, but is instead mounted on a tantalum absorber. Figure 5.11 again shows the rates of events above 200 keV for a source in position 1 in detectors in string 1, with and without a tantalum absorber of height 60 mm. The addition of the tantalum absorber shifts the event rate maximum by (16.3 ± 1.8) mm and reduces the event rate by 8.5%. Therefore the effect of the tantalum absorber can be compensated for by increasing the activity of the source by 9% and by increasing the separation between the bottommost source and the lowest one on the steel band by 16 mm.

Due to the height restrictions on the SIS, the vertical size of the absorber may be reduced. Additional simulations were also made with absorber heights ranging from 1 mm to 55 mm. As shown in Figure 5.12, the shift in location of the rate maximum and intensity reduction are stable as long as the absorber height remains at 7 mm or higher, or about twice the radiation length of tantalum of 4.094 mm [161].

5.4.2 *Exposure times*

We can calculate the time required to perform a precise energy calibration by considering the rates of FEP and DEP events observed in each detector.

Again, by symmetry, we can consider only the strings 1 to 4. Strings 1 and 4 are closest to the sources, so strings 2 and 3 will be the limiting cases.
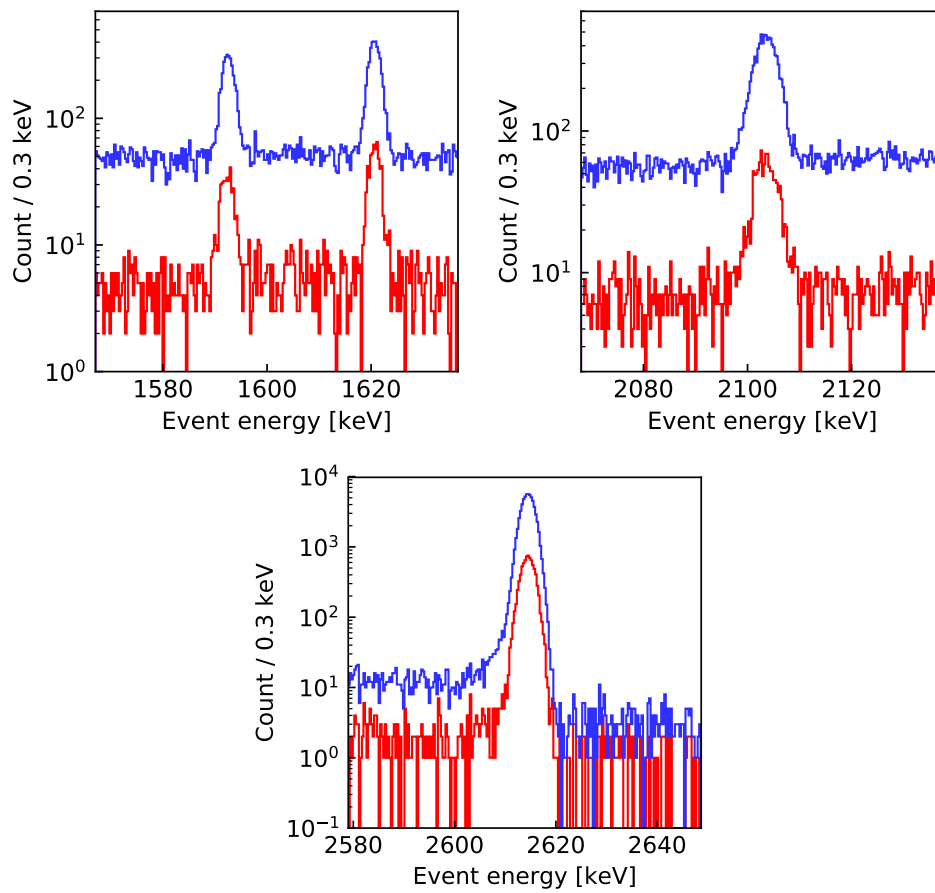
Figure 5.9: Zooms of Figure 5.8 to the regions around the DEP/SEP/FEP are shown from the top left to bottom respectively. The 1621 keV γ line of ^{212}Bi is visible to the right of the DEP.
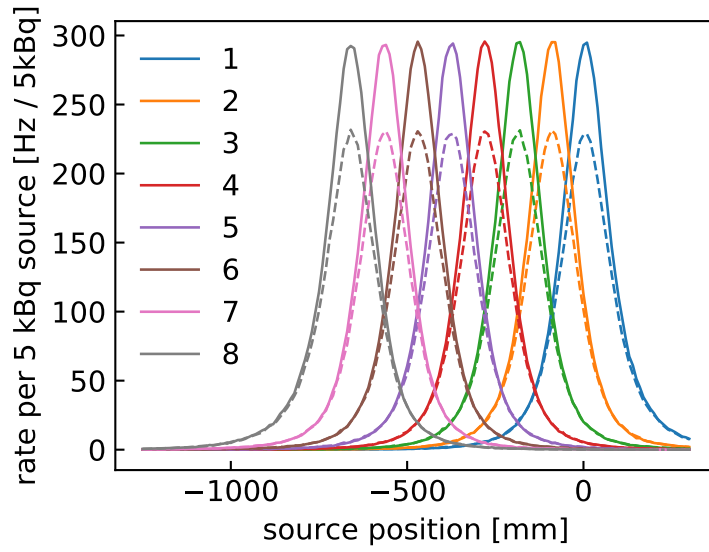
Figure 5.10: Event rates above 200 keV for a source in position 1 (solid lines) and position 2 (dashed lines). In each case the event rate in detectors of the closest string are shown, labelled by their position in the string.
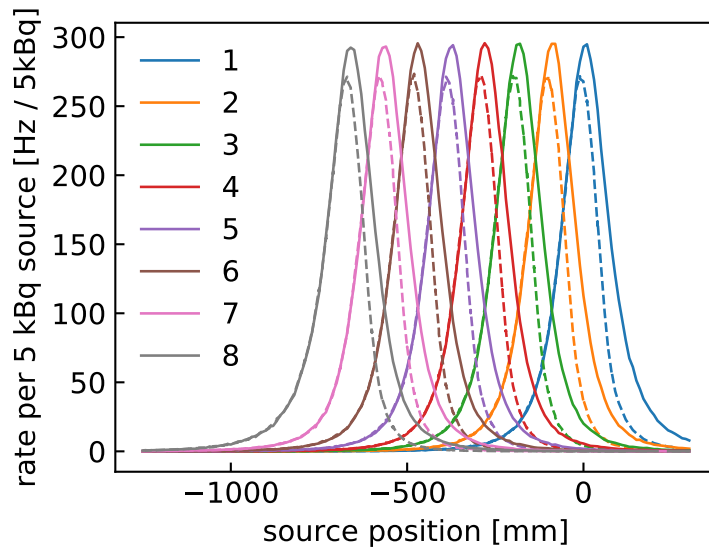
Figure 5.11: Event rates above 200 keV for a source in position 1 without (solid lines) and with (dashed lines) a 60 mm tantalum absorber.
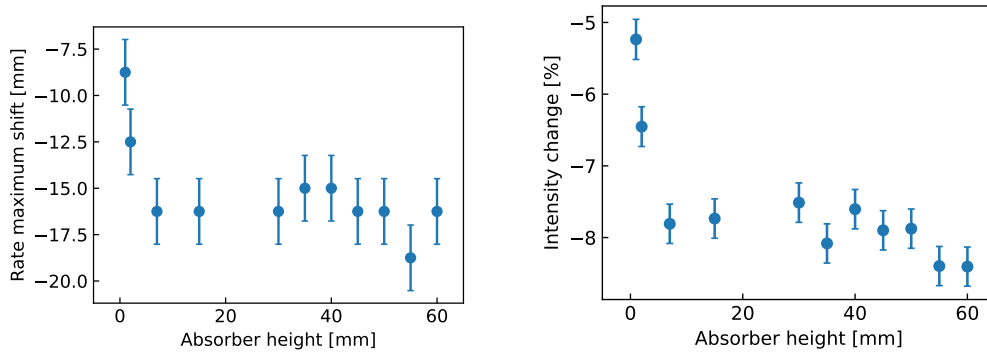
Figure 5.12: Rate maximum shift (left) and intensity reduction (right) for absorbers of various heights.

| Source | Stopping | FEP event rate [Hz] | | | |
| | | String 2 | | String 3 | |
position	point	Det 1	Det 8	Det 1	Det 8
1	Top	8.41 ± 0.51	0.09 ± 0.04	3.43 ± 0.34	0.11 ± 0.05
	Bottom	0.15 ± 0.07	8.20 ± 0.50	0.12 ± 0.07	3.20 ± 0.33
2	Top	2.29 ± 0.29	0.05 ± 0.04	5.21 ± 0.41	0.09 ± 0.05
	Bottom	0.10 ± 0.05	2.06 ± 0.27	0.07 ± 0.03	4.57 ± 0.38

Table 5.1: FEP event rates in the top and bottom detectors of strings 2 and 3 for the top and bottom stopping points of a standard source string.

Table 5.1 shows the FEP event rates in the top and bottom detectors of strings 2 and 3 when a source string formed of four 5 kBq sources is either in the top or bottom stopping position. This is henceforth referred as the standard source string. The rates of Table 5.1 are produced by summing the single source FEP rates over each source height where the source centres align with one of the top (or bottom) four detectors.

The time required for a calibration will be minimised by adjusting the stopping times for each source position i and stopping position j, t_{ij}, such that the events acquired in these detectors is equalised. The times can be calculated by inverting the matrix M formed by the rates in Table 5.1. The above can be expressed as

$$
M \begin{pmatrix} t_{1T} \\ t_{1B} \\ t_{2T} \\ t_{2B} \end{pmatrix} \propto \begin{pmatrix} 1 \\ 1 \\ 1 \\ 1 \end{pmatrix},
$$

$$
\begin{pmatrix} t_{1T} \\ t_{1B} \\ t_{2T} \\ t_{2B} \end{pmatrix} \propto M^{-1} \begin{pmatrix} 1 \\ 1 \\ 1 \\ 1 \end{pmatrix}, \tag{5.4}
$$

where T and B label the top and bottom stopping positions. We then find that

$$
\begin{pmatrix} t_{1T} \\ t_{1B} \\ t_{2T} \\ t_{2B} \end{pmatrix} \propto \begin{pmatrix} 0.693 \\ 0.712 \\ 1.203 \\ 1.393 \end{pmatrix}
\tag{5.5}
$$

To achieve 200 events in the DEP of the above detectors would require a total of 47 min of source exposure, split according to Equation 5.5, as detailed in Table 5.2. The minimum number of FEP events in any detector would then be 6200, allowing for a determined position precision of 0.02 keV. The total time required for a calibration would be given by 47 min $\times$ 2 = 94 min for additionally moving the sources at positions 3 and 4, as well as the time required to move the sources through these positions.

5.4.3   *Event rates*

DAQ requirements are such that the maximum event rate in a single detector is 300 Hz. Table 5.3 gives the event rates above 200 keV for source strings formed of four 5 kBq sources. The maximum event rate observed in one detector is 522.15 Hz, for string 1, detector 6, when the source in position 1 is at its lower stopping point. Figure 5.13 shows the event rate in that detector for varying energy thresholds. An energy threshold of 345 keV would satisfy the maximum event rate of 300 Hz.

The DAQ also requires that the maximum event rate in a single digitiser card, reading out six detector channels, is 1000 Hz. We make the simplifying assumption that increasing the energy threshold to 345 keV reduces the event rate in all detectors by the same ratio. Table 5.4 then gives the total event rate (for eight detectors) above 345 keV in each string for each source position and stopping position. None of these rates exceeds 1000 Hz, so

Source position	Stopping point	Stopping time [minutes]
1	Top	8.14
	Bottom	8.36
2	Top	14.1
	Bottom	16.4
3		Same as source 1
4		Same as source 2
	Total	94.0

Table 5.2: Times required for each source string and at each stopping point for a standard source string, for a minimal calibration reaching 200 DEP events in all detectors.

Source position	Stopping point	Detector	Event rate above 200 keV [Hz] String			
			1	2	3	4
1	Top	1	419.71	222.48	88.02	40.48
		2	505.69	278.21	111.36	52.34
		3	516.38	284.89	109.66	50.88
		4	432.17	231.11	89.35	42.99
		5	131.59	95.43	48.53	27.08
		6	26.79	26.36	19.47	13.43
		7	7.76	8.37	6.90	6.34
		8	3.07	3.39	3.10	2.47
	Bottom	1	3.47	3.31	3.50	3.17
		2	8.68	9.31	7.90	6.14
		3	29.99	28.31	21.06	13.55
		4	139.71	98.51	49.65	27.19
		5	422.60	223.79	88.58	42.16
		6	522.15	289.19	114.35	52.03
		7	518.88	285.80	113.77	50.76
		8	413.36	222.16	86.97	40.27
2	Top	1	30.78	58.09	139.12	344.27
		2	37.08	72.94	175.07	420.82
		3	36.98	73.93	177.85	429.66
		4	30.18	59.37	141.65	355.83
		5	21.14	35.83	69.21	121.80
		6	10.79	16.23	24.02	26.84
		7	5.70	7.02	8.18	8.00
		8	2.38	2.79	3.20	2.99
	Bottom	1	2.67	2.69	3.36	3.79
		2	5.62	7.72	8.91	9.24
		3	11.38	16.62	24.63	30.05
		4	20.09	35.86	70.52	126.64
		5	30.93	59.38	136.79	347.64
		6	38.01	73.87	179.44	435.35
		7	37.88	73.64	179.85	432.97
		8	30.84	56.56	134.89	341.27

Table 5.3: Event rates above 200 keV in strings 1 to 4 for a standard source string at source positions 1 and 2.
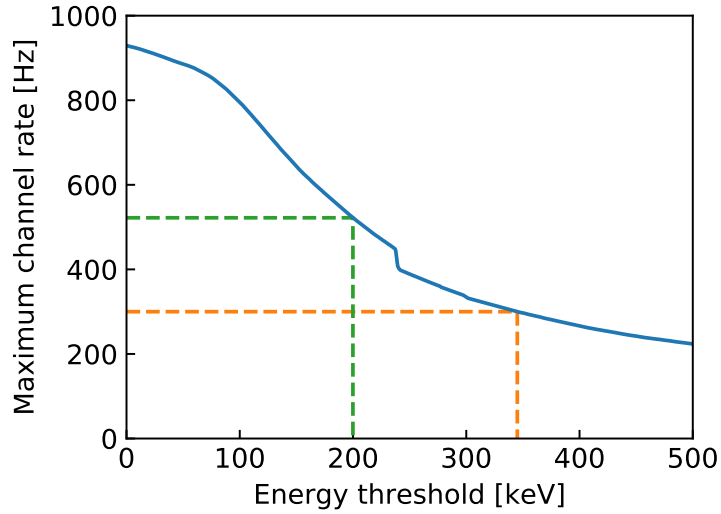
Figure 5.13: Event rate versus energy threshold, for string 1, detector 6, when the source in position 1 is at its lower stopping point. The green (orange) dashed line indicates that a threshold of 200 keV (345 keV) results in an event rate of 522 Hz (300 Hz). The kink observed at 238.6 keV is due to the strong γ line at that energy due to ^{212}Pb decays.

Source position	Stopping point	String event rate above 345 keV [Hz]			
		String 1	String 2	String 3	String 4
1	Top	782.6 ± 3.0	440.6 ± 2.4	182.5 ± 1.6	90.4 ± 1.1
	Bottom	788.6 ± 3.0	444.5 ± 2.4	186.1 ± 1.6	90.1 ± 1.1
2	Top	67.0 ± 1.0	124.9 ± 1.3	282.8 ± 1.9	655.1 ± 2.8
	Bottom	68.0 ± 1.0	125.0 ± 1.3	282.8 ± 1.9	661.5 ± 2.8

Table 5.4: Total string event rates above 345 keV for a standard source string at source positions 1 and 2.

combining groups of six detectors to each digitiser board should not pose any problems.

5.4.4 *Distribution of DEP and SEP events*

In Section 3.6.1, we hypothesised that the broadening observed in the Double Escape Peak (DEP) was caused by these events being more likely to originate towards the edge of the detector. In [134], the Full Charge Collection Depths (FCCD) for the GERDA IC detectors was determined to be $\mathcal{O}(1\,\text{mm})$. Events taking place closer to the detector edge than the FCCD, (i.e. not in the active region) are more likely to be affected by incomplete charge collection.

Figure 5.14 shows the distribution of the energy deposits for the FEP, DEP, SEP, and other events with energies outside these peaks. Table 5.5 shows the mean event radius for these classes of events, where the detector radius is 37 mm, and the fraction of events occuring outside of the active region. DEP events are on average reconstructed (2.47 ± 0.18) mm further towards the detector edge than other events. Additionally, a higher fraction of the DEP events occur within 1 mm of the detector edge, outside of the active region of the detector.
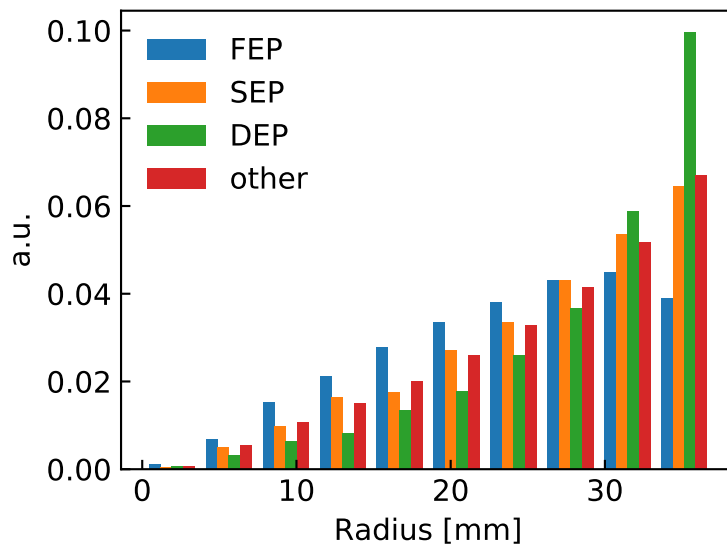
Figure 5.14: Distribution of the energy deposits in FEP, DEP, SEP and other events. Here, other events refers to those with energies outside of the FEP, SDEP and SEP peaks. DEP events are more likely to be in the outer region of the detector, since the two annihilation γs must escape.

Event type	Mean event radius [mm]	Fraction outside active region [%]
FEP	24.03 ± 0.03	2.94(7)
DEP	28.82 ± 0.15	10.85(68)
SEP	26.40 ± 0.09	5.64(28)
other	26.35 ± 0.01	7.76(3)

Table 5.5: Mean event radii for FEP, DEP, SEP and other events, and the fraction of events occuring outside of the active region (here defined as within 1 mm of the detector edge).

5.5   CONCLUSIONS

The purpose of the simulations described in this chapter was to determine the parameters of the source strings and calibration procedure.

In Section 5.4.1, we saw that for detector strings each formed of eight identical detectors, the ideal source separation of a source string of four sources is given by the detector unit separations, 10 cm in these simulations.

We also saw that the effect of adding a tantalum absorber to a source was to shift the location of the peak event rate by 16 mm and to reduce the event rate by 8.5%. These conclusions were valid for an absorber with height between 7 mm and 60 mm. The effect of adding an absorber to the lowest source on the string can be therefore compensated by increasing the separation of the lowest two sources by 16 mm and by increasing the activity by 9%.

The nominal activity of each source was taken to be 5 kBq (with an assumed 9% increase for the bottommost source on the string). The new sources are being produced at LANL. The activity of previous sources for GERDA [134] varied by more than a factor of two, with even the two closest activities differing by 11%. We therefore do not suggest attempting to tune the activities of the sources in production, but to, for example, place the sources with the highest activity with the absorbers.

Section 5.4.2 calculated the time required to perform a precise (0.1 keV position precision on the DEP) calibration. By optimising the exposure times for each source position and stopping point, a calibration can be achieved within 94 min, with the addition of the time required for moving the sources. This is based on moving each of the source strings individually.

The implementation of a more realistic detector geometry will alter the above conclusions. In particular, the BEGe and PPC type detectors will require longer exposure to the calibration sources, due to their smaller mass, which is on average ∼30% of a IC detector.

Section 5.4.3 considered the total event rates that would be observed during a calibration, both for a single detector and for each string of detectors. By using an event threshold of 345 keV, the maximum event rate in a single detector can be kept below 300 Hz, and the total event rate in a string will not exceed 1000 Hz.

Finally, Section 5.4.4 showed that DEP events are more likely to be occur closer to the edge of the detector. The broadening observed in this peak discussed in Section 3.6.1 could therefore be due to effects related to incomplete charge collection in this region. The rise time of a waveform depends on the location of the event in the detector. Therefore, a correction to the energy based on the rise time, as was performed by MAJORANA [162], could improve the resolution of this peak substantially.

CONCLUSIONS

The observation of neutrinoless double-beta decay ($0\nu\beta\beta$), a hypothetical lepton-number violating process, would demonstrate the Majorana nature of the neutrino. This thesis was completed in the context of the GERDA and LEGEND collaborations, both of which search for $0\nu\beta\beta$ using high-purity enriched ^{76}Ge detectors. These detectors exhibit an excellent energy resolution of $\mathcal{O}(0.1)\%$, better than any other technology employed by $0\nu\beta\beta$ experiments, which benefits the experimental sensitivity to the half-life of this decay.

Phase II of the GERDA experiment acquired data between December 2015 and November 2019. The following results are from the final $0\nu\beta\beta$ analysis of GERDA, derived from data corresponding to 103.7 kg yr of exposure [88]. In the region of interest, between 1930 keV and 2190 keV, a background level of $5.2^{+1.6}_{-1.3} \cdot 10^{-4}$ counts/(keV kg yr) was achieved. The best fit of the data is achieved for a null signal strength, with a derived lower limit on the $0\nu\beta\beta$ half-life in ^{76}Ge given by $> 1.8 \cdot 10^{26}$ yr at 90% C.L.. This corresponds to a limit of $m_{\beta\beta} < (80 - 182)$ meV. These are the most stringent half-life limit and lowest background level obtained by any $0\nu\beta\beta$ experiment.

A reliable and precise determination of the energy scale and energy resolution of the germanium detectors is vital for achieving this final result. This was achieved by the weekly exposure of the array to three ^{228}Th sources. In total, 142 calibration runs were used to determine the energy scale of the detectors during GERDA Phase II. The observed pattern of γ lines in the energy spectrum is then used to calibrate the detectors. The positions of the strong ^{208}Tl γ line at 2.6 MeV and of injected pulser events are used to monitor the stability of the energy scale between calibrations.

A major development of the final $0\nu\beta\beta$ analysis was the division of the data from each detector into stable sub-periods called partitions. The divisions were determined by monitoring the stability of two parameters: the resolution of the ^{208}Tl full-energy peak at 2.6 MeV, and the residual of the corresponding single-escape peak at 2.1 MeV.

For each partition, the effective energy resolution at $Q_{\beta\beta}$ was determined from combined calibration spectra. The exposure-weighted average resolutions ($\pm$ the standard deviation) at $Q_{\beta\beta}$ across the partitions for the BEGe/Coaxial/IC detectors are given by (2.8 ± 0.3) keV, (4.0 ± 1.3) keV and (2.9 ± 0.1) keV respectively. Dedicated studies were performed to study various sources of systematic uncertainties to the resolution at $Q_{\beta\beta}$, with the average total uncertainty given by 0.13 keV. The energy bias for the events near $Q_{\beta\beta}$ is approximated as the residual of the SEP in the com-

bined spectra. The average bias is $-0.1\,\text{keV}$ with a standard deviation of $0.3\,\text{keV}$.

The LEGEND collaboration aims to build the next generation of $^{76}\text{Ge}\ 0\nu\beta\beta$ decay experiments. LEGEND-200 is currently being constructed at LNGS, reusing much of the GERDA infrastructure. 14 strings of detectors will be deployed, reaching a total mass of 200 kg. Various measures, including the installation of a new LAr veto system and the reduction in the use of passive components, should allow LEGEND-200 to reach its goal background level of 0.6 cts/(FWHM·t·yr). With $1\,\text{t}\cdot\text{yr}$ of exposure, the half-life (discovery and limit) sensitivity of LEGEND-200 should exceed $10^{27}\,\text{yr}$.

For the energy calibration of the germanium detectors, LEGEND-200 will operate Source Insertion Systems that are able to deploy multiple sources each, instead of just a single one as in GERDA. Some parameters of these systems, such as the source isotope, and the radius at which they will be deployed, are determined according to the experimental requirements. Monte Carlo simulation studies have determined the optimal source separations on the steel band, and the number and location of stopping points by the germanium detectors. The effect of adding an absorber to the lowest source on the string can be compensated by increasing the separation of the lowest two sources by 16 mm and by increasing the activity by 9%. Assuming a nominal source activity of 5 kBq, an energy threshold of 345 keV will satisfy the DAQ maximum event rate of 300 Hz. The time required to perform a precise energy scale determination has then been calculated at 94 min, excluding the time required to move the sources.

After LEGEND-200, the LEGEND-1000 experiment aims to achieve an exposure above $10\,\text{t}\cdot\text{yr}$ and an even lower background of 0.03 cts/(FWHM·t·yr). LEGEND-1000 aims to achieve a half-life sensitivity exceeding $10^{28}\,\text{yr}$, and is currently in the planning stage. A modular approach is envisioned, where multiple payloads would be installed over the course of several years. This approach would allow for continuous data taking while the experiment continues to scale up to full size. LEGEND-1000 and other future ton-scale experiments will be sensitive to Majorana masses in the entire parameter space allowed for the inverted ordering.
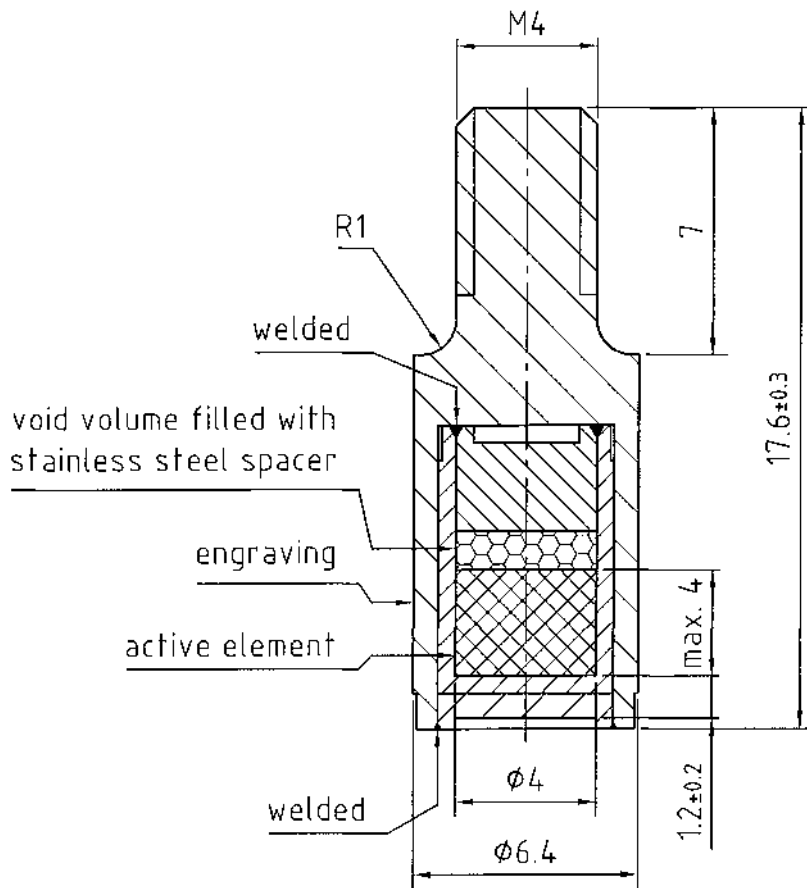
Figure A.1: Schematic of a source capsule. The dimensions are given in mm. The M4 thread serves to screw the source into either the tantalum absorber or adaptors welded to the steel band of the SIS. Figure from [134].

Figure A.2

Figure A.3: Schematic of a source adaptor. Dimensions are given in mm.
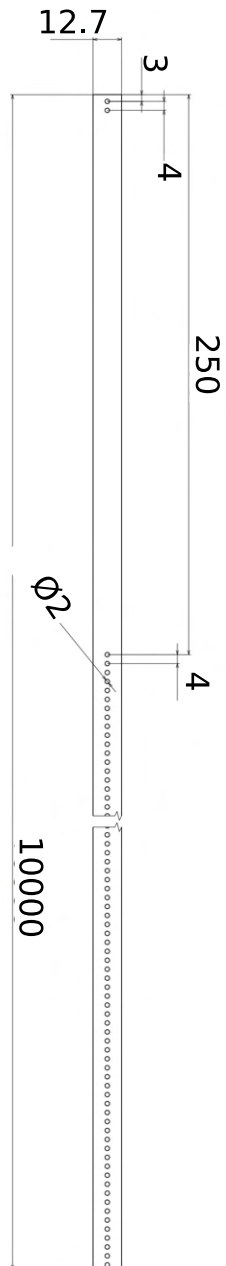
Figure A.4: Schematic of the SIS steel band. Dimensions are given in mm.

CHARACTERIZATION OF A PMT WITH A MGF$_2$ WINDOW

B.1 INTRODUCTION

Photomultiplier tubes (or PMTs), are light detectors designed to be sensitive to very low light intensities. In GERDA, PMTs formed part of the liquid argon (LAr) veto system, detecting the 128 nm LAr scintillation light stimulated by background events. The 3″ PMTs used are of the R11065-20 Mod type, produced by Hamamatsu. Since, like most materials, their quartz window is opaque to 128 nm wavelengths, the PMTs are coated with a layer of wavelength shifting TPB.

One material transparent to 128 nm light is MgF$_2$, as shown in Figure B.2. Hamamatsu has produced a version of the R11065 PMT with a MgF$_2$ window, shown in Figure B.1. This PMT could therefore be directly sensitive to LAr scintillation light, without the use of additional wavelength shifting materials close to the germanium detectors.
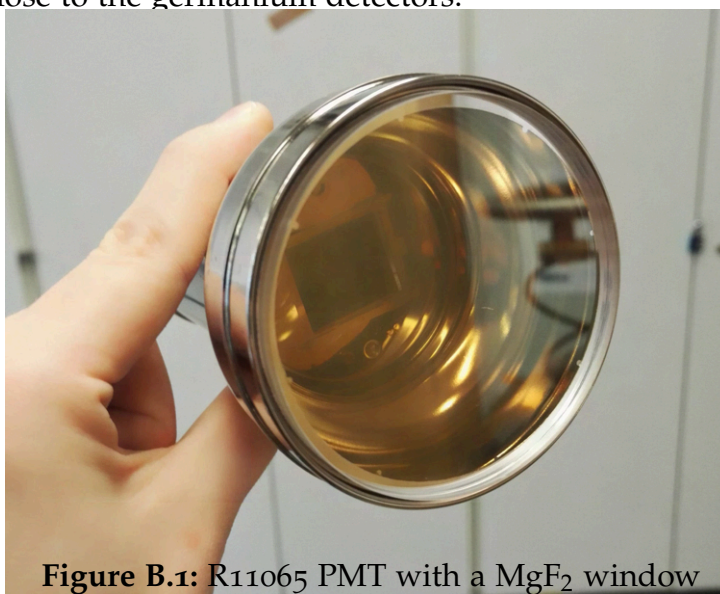
Figure B.1: R11065 PMT with a MgF$_2$ window

This remainder of this section describes the operation of PMTs. In the following sections, the experimental setups are introduced, and characterisation of one such MgF$_2$ PMT is described.

The basic structure and operating principle of a PMT is shown in Figure B.3. It consists of a vacuum tube containing a number of electric dynodes, which are supplied with high voltage to create a voltage gradient between the photocathode and the anode. A photon incident on the faceplate of the PMT will pass through the window and interact with the pho-
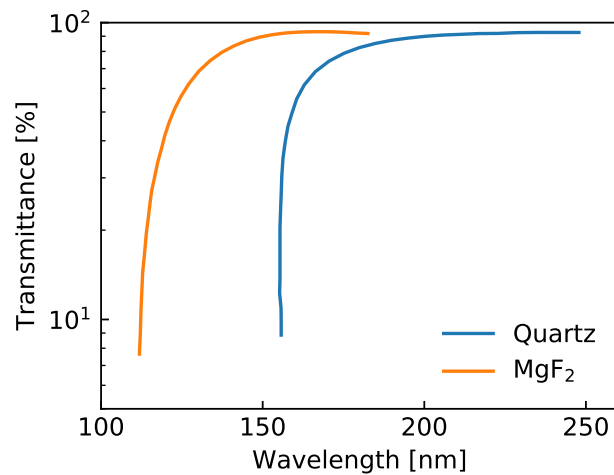
Figure B.2: Transmittance of quartz and MgF$_2$. Data from Hamamatsu.

tocathode. Via the photoelectric effect, an electron will be emitted from the photocathode. The electron accelerates towards the first dynode due to the electric field, where additional electrons are emitted. These electrons are then accelerated towards the next dynodes, each time being further amplified. The final dynode is connected to the anode where the signal is read out. The MgF$_2$ R11065 PMT has a round three-inch diameter bialkali photocathode and 12 dynode stages.
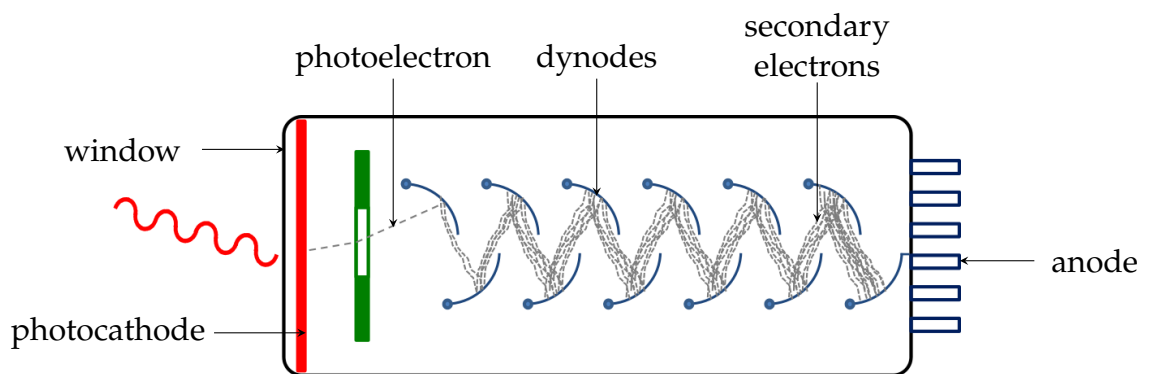
Figure B.3: Schematic of PMT. Adapted from [163].

The probability that an incident photon produces a photoelectron at the cathode is called the quantum efficiency (QE). This depends on the window and photocathode materials, as well as the wavelength of the photon. The quantum efficiency of this PMT was measured by Hamamatsu, and is shown in Figure B.4. The maximum QE is 38% at 185 nm. The QE at the wavelength of LAr scintillation light, 128 nm, is 23%.
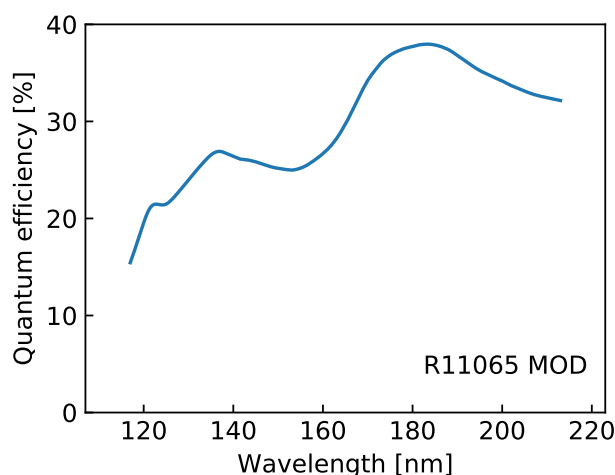
Figure B.4: Quantum efficiency of the R11065 PMT with a MgF_2 window. Data from Hamamatsu.

B.2 EXPERIMENTAL SETUPS

B.2.1 *Test facilities*

Room temperature measurements of the MgF_2 PMT were performed in Sandbox. SandBox is a PMT characterisation facility developed at UZH [164, 165]. It consists of a light-tight black box, wherein a PMT and a light source (here a 470 nm LED) can be placed facing each other. Feedthroughs are installed to provide a bias voltage to the PMT and read out its signal, and to power the LED. The facility is shown in Figure B.5.

Figure B.5: Sandbox, the light-tight black box PMT testing facility.

The Liquid Argon Setup (LArS) at UZH was first developed to test wavelength shifting materials for the development of the GERDA liquid argon veto [166]. It consists of a vessel which can be filled with either argon or nitrogen, and is equipped with two temperature sensors, a liquid levelme-

ter, and a 470 nm LED. A combination of liquid nitrogen flow and a small heater are used to regulate the temperature. The PMT is installed facing downwards. The facility is shown in Figure B.6.
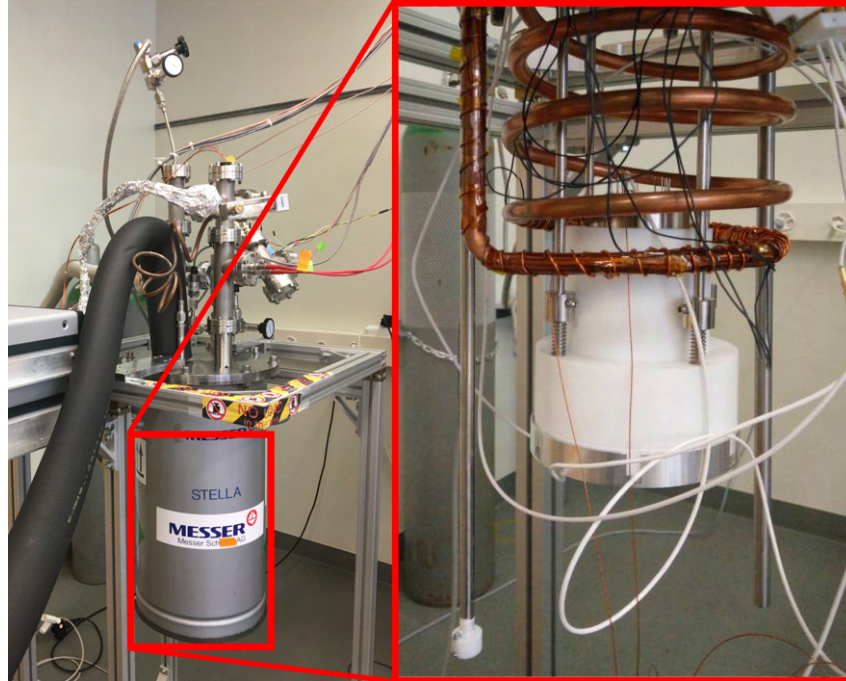
Figure B.6: An external (left) and internal (right) view of LArS. On the right, the copper cooling coils and PTFE PMT mount are visible.

B.2.2 *Signal processing*

A voltage divider base provides the voltage to each dynode from a single high voltage supply. The anode signal is also read out from the base. The base used for measurements of this PMT is the same as that used for the R11410 PMTs used in the XENON1T experiment [167], and is shown in Figure B.7.
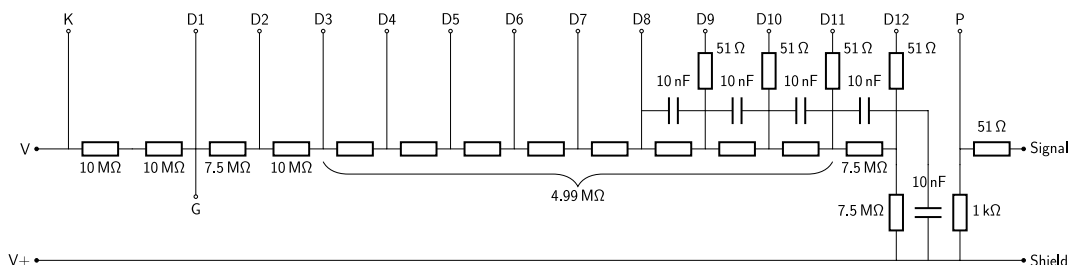
Figure B.7: Base voltage divider circuit. K labels the photocathode, G the focusing grid, D-12 the dynode and P the anode. Figure from [168].

To digitise the PMT signals, either a CAEN v1720 flash ADC (12 bit resolution, 250 MHz sampling frequency), CAEN v1724 flash ADC (14 bit

resolution, 100 MHz sampling frequency) or a CAEN v1730 flash ADC (14 bit resolution, 500 MHz sampling frequency) was used, depending on the measurement. The signal may also be optionally amplified by a ten-fold 776 Philips amplifier prior to digitisation. Where an LED is used, the LED and ADC are simultaneously triggered by a Telemeter TG55011 pulse generator.

Once PMT signals are digitised, they are processed using software developed at UZH, WARP [169]. This software calculates the baseline of the waveform. It also locates peaks in a waveform, and calculates parameters including their position, amplitude, area, etc. An example waveform is shown in Figure B.8.
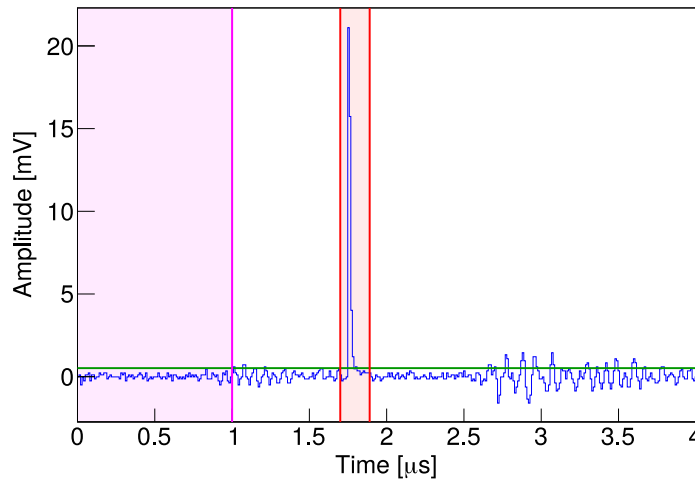
Figure B.8: An example waveform processed with WARP. The baseline (green line) is calculated based on the waveform samples in the first 1 μs (pink shaded area). A single peak is detected above a threshold of three times the baseline (red shaded area), from which parameters such as the amplitude and area can be calculated. Figure adapted from [169].

B.3 CHARACTERISATION

This section describes the measurements that were taken to characterise this MgF_2 PMT.

B.3.1 *Gain*

The mean signal (secondary electrons collected at the anode) observed for a signal photoelectron is called the gain G, which for typical PMTs of this size will be on the order of a few million. It is given by the product of the secondary emission ratios δ_i of each dynode i,

$$G = \prod_i \delta_i. \tag{B.1}$$

Empirically, the secondary emission ratio can be expressed as

$$\delta_i = a\Delta V_i^k, \tag{B.2}$$

where ΔV_i is the total voltage difference between the ith and $(i-1)^{\text{th}}$ dynode, and a and k are constants depending on the dynode material. Where ΔV_i is constant for all n dynodes, the gain can be expressed as

$$G = \prod_i a\Delta V_i^k = a^n \left(\frac{V_{\text{bias}}}{n+1} \right)^{kn} = cV_{\text{bias}}^\alpha, \tag{B.3}$$

where V_{bias} is the voltage difference between the photocathode and anode, and c and α are constants.

The gain of a PMT is extracted from a Single Photoelectron (SPE) spectrum. To acquire this, the LED intensity is adjusted to produce predominantly single photons. The LED power and the PMT data acquisition are then simultaneously triggered via an external pulse generator. An example of a resulting PMT waveform is shown in Figure B.9.

For each applied bias voltage, 500 000 events were acquired. This data was taken with the PMT installed with the Sandbox facility, using the CAEN v1724 ADC.
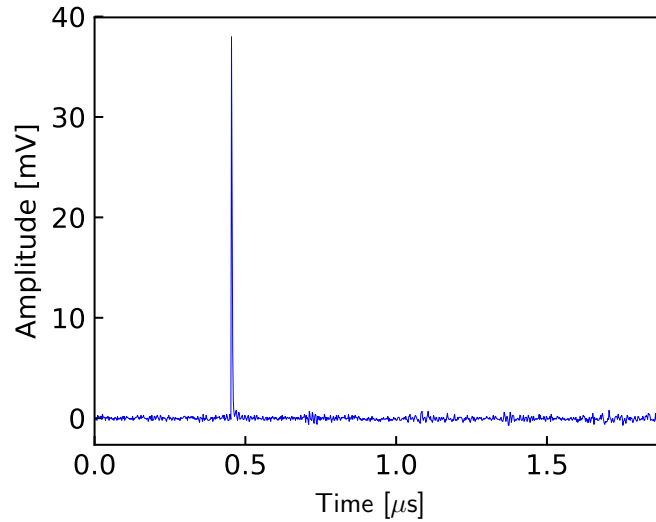
Figure B.9: Example PMT waveform obtained during a gain measurement

From each waveform, the area of each pulse (i.e. the number of signal electrons from the PMT) is calculated using WARP (see Section B.2.2. The distribution of these areas then gives a SPE spectrum, shown in Figure B.10. Such a spectrum consists of a noise peak and then successive peaks for each number of photoelectrons produced. The fit function of the SPE spectrum is thus given by

$$f(x) = A_0 \exp \left(-\frac{(x-\mu_0)^2}{2\sigma_0^2} \right) + \sum_i A_i \exp \left(-\frac{(x-i\mu)^2}{2i\sigma^2} \right) \tag{B.4}$$

where A_0, μ_0 and σ_0 label the amplitude, mean and standard deviation of the noise peak, A_i label the amplitudes of the photoelectron peaks, and μ and σ label the mean and standard deviation of the first photoelectron peak. The centroid of the first photoelectron peak, μ, gives the mean number of signal electrons produced by the PMT after a single photoelectrode has been emitted from the photocathode, i.e. the gain.
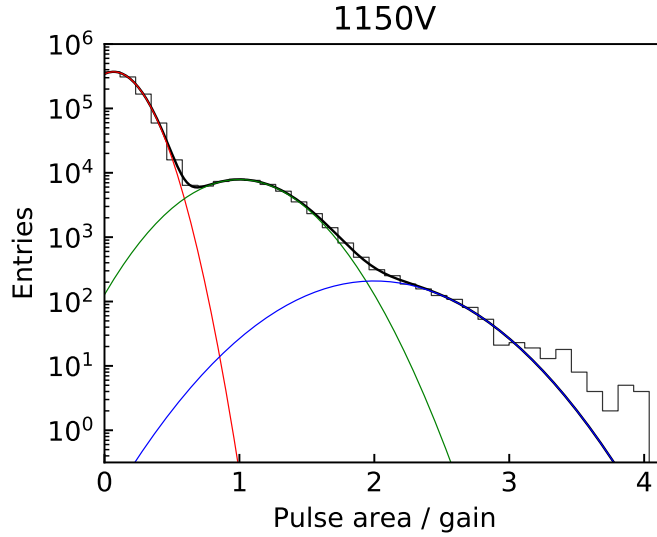
Figure B.10: Example of normalised SPE spectrum for a bias voltage of 1150 V. The spectrum consists of a noise peak (red), the SPE peak (green) and the double photoelectron peak (blue). Here, the pulse areas are normalised by the centroid of the SPE peak, i.e. the gain.
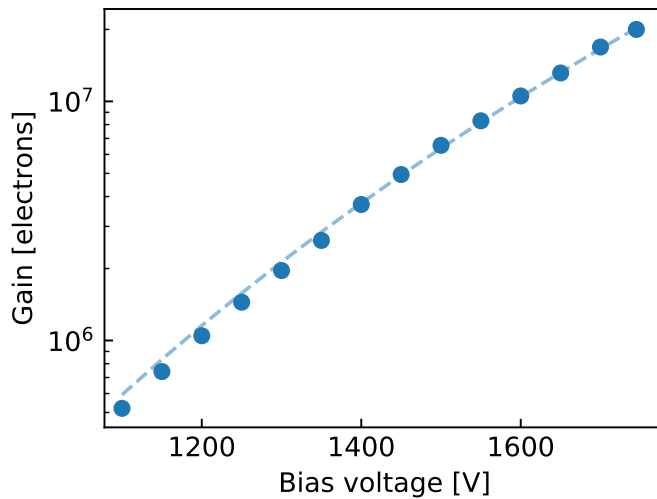
Figure B.11: PMT gain as a function of bias voltage

Figure B.11 shows the measured gain relative to the bias voltage applied to the MgF$_2$ PMT. The best fit values for equation B.3 are given by $c =$
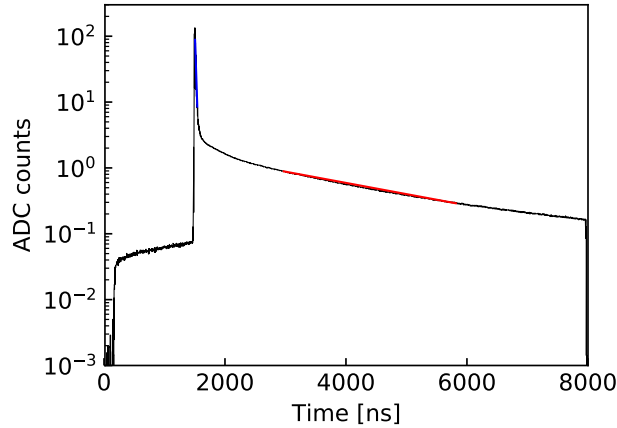
Figure B.12: The mean collected PMT waveform when exposed to a ^{241}Am source in LArs, filled with liquid argon. The exponentially decreasing amplitude due to the short (long) components of LAr scintillation light is shown in blue (red).

$3.1 \cdot 10^{-18}$ and $\alpha = 7.7$. The gain at the nominal operating voltage of $1500\,\text{V}$ is given by $6.5 \cdot 10^6$ electrons/photoelectron.

B.3.2 *Observation of LAr scintillation light*

In order to confirm the response of the PMT to liquid argon scintillation light, an alpha-emitting ^{241}Am source was placed with the PMT inside LArS, which was filled with liquid argon. ^{241}Am emits α particles with energy $5.5\,\text{MeV}$ during its decay to ^{237}Np. The source was produced for testing the wavelength shifting foils used in GERDA [166, 170], via electrodeposition on a stainless steel substrate. This is then mounted on an aluminium plate installed below the PMT.

The mean collected waveform is shown in Figure B.12 It displays the characteristic exponentially decreasing amplitude from the short ($\mathcal{O}(10\,\text{ns})$) and long ($\mathcal{O}(1.5\,\mu\text{s})$) components due to the two excited states of of LAr scintillation light, confirming its sensitivity at these wavelengths.

B.3.3 *Dark current*

An important characteristic of a PMT concerns its noise output. Thermal fluctuations may result in the spontaneous emission of an electron from the photocathode. This electron will then be amplified as it passes through the dynodes, and will be measured at the anode. The rate of these unwanted noise events is called the dark count (DC) rate.

To measure this, instead of digitising the signals, the unamplified PMT signal is connected to a CAEN N845 discriminator, which is then fed to

a CAEN v260 scaler. The result of this is to count the number of signals above some threshold set in the discriminator. The discriminator threshold is set to 0.3 times the average amplitude of a single PE signal.

An increase in the DC rate was observed during cooldown in an argon environment, see Figure B.13. At room temperature, the dark count rate is around 1.2 kHz. At around 90 K, (c.f. the boiling temperature of argon of 87.3 K), a sharp increase in the dark count rate is observed to a maximum of 9 kHz.

However, in cooldown in a nitrogen environment, no such increase was observed, see Figure B.14. At room temperature, the dark count rate is again around 1.2 kHz. This rate sharply drops when cooled, stabilising at around 0.3 kHz below a temperature of approximately 200 K.

These observations further indicate that the PMT is observing liquid argon scintillation light, stimulated due to cosmic and/or atmospheric muons.
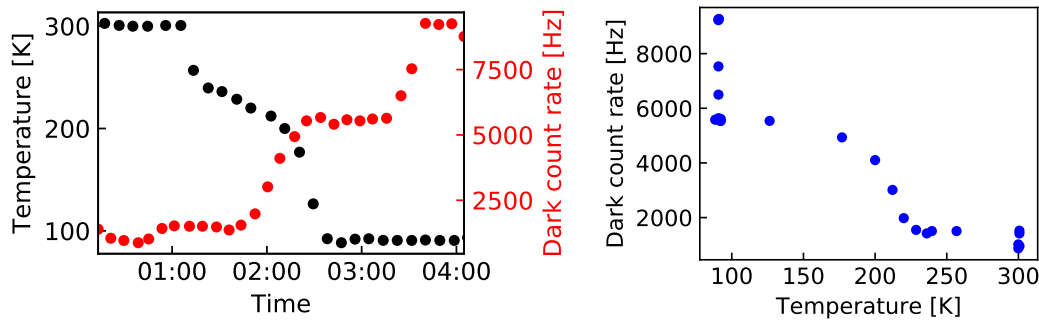
Figure B.13: Top: the temperature (black) and dark count rate (red) during cooldown in LArS in a liquid argon environment. Bottom: the relationship between the dark count rate and temperature.
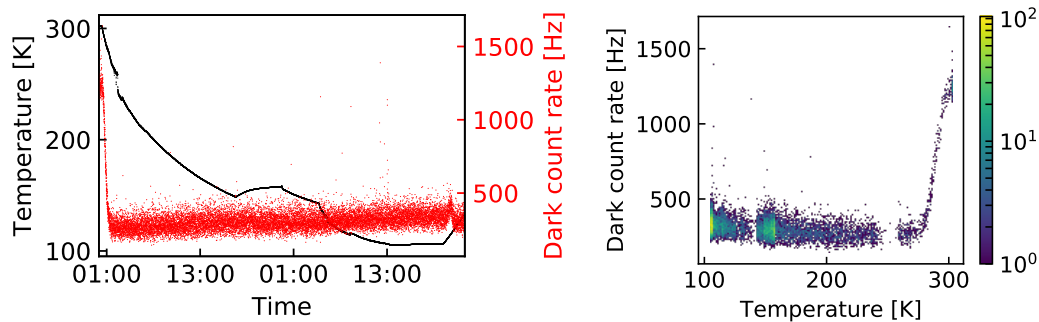
Figure B.14: Top: the temperature (black) and dark count rate (red) during cooldown in LArS in nitrogen. Bottom: the relationship between the dark count rate and temperature.

B.3.4 *Afterpulses*

Afterpulses are peaks that are observed after a trigger peak in a PMT. They are caused by photoelectrons ionising residual gas molecules inside the vacuum chamber between the photocathode and first dynode. The positive ions then drift back in the electric field towards the photocathode, and cause further production of photoelectrons, which are later observed after they have been amplified by the PMT.

It is possible to estimate the delay between an afterpulse and the main trigger pulse by making an assumption for the field between the photocathode and the first dynode. A simple assumption is a quadratic field dependence, where the voltage at a distance x from the first dynode can be expressed as

$$V(x) = V_0 \left(1 - \frac{x}{L}\right)^2, \tag{B.5}$$

where V_0 is the voltage at the first dynode and L is the distance between the photocathode and first dynode.

The total delay time between the triggering event and the secondary afterpulse peak is given by the sum of the drift time of the ion to the photocathode, and the drift time of the stimulated electrons back to the first dynode. Since the ions are much heavier than the electrons, the drift time of the electrons is negligible. Therefore the delay between the main pulse and the afterpulse is given by

$$\Delta t = \int_{s_0}^{L} \frac{1}{v} \, \mathrm{d}s \tag{B.6}$$

$$= \sqrt{\frac{m}{2q}} \int_{s_0}^{L} [V(s_0) - V(s)]^{-1/2} \, \mathrm{d}s \tag{B.7}$$

$$= \sqrt{\frac{m}{2qV_0}} \int_{s_0}^{L} \frac{L}{\sqrt{(L - s_0)^2 - (L - s)^2}} \, \mathrm{d}s \tag{B.8}$$

$$= \frac{L\pi}{2} \sqrt{\frac{m}{2qV_0}}, \tag{B.9}$$

where s_0 is the distance between the ionisation position and the first dynode, and m and q are the mass and charge respectively of the ion. The time delay scales with mass, and is independent of the ionisation position s_0.

The dependence of the afterpulse delay on the mass-to-charge ratio of the ion, m/q, allows for ion identification in the resulting afterpulse spectrum. The average time delay of a particular peak in the afterpulse spectrum can be converted into a mass-to-charge ratio. Let M be the mass of the ion in units of proton mass, and Q the charge of the ion in units of electron charge:

$$\frac{M}{Q} = \frac{8V_0}{(\pi L)^2} \frac{q_p}{m_p} (\Delta t)^2 = C_0 \cdot (\Delta t)^2, \tag{B.10}$$

C_0 can be calculated theoretically using:

$$C_0 = \frac{8V_0}{(\pi L)^2} \frac{q_p}{m_p} \, , \tag{B.11}$$

but it can also be calculated empirically by looking in an afterpulse spectrum for ions that are expected in the chamber, for example hydrogen.

Hamamatsu has indicated that during the production of these PMTs, the MgF_2 does not always tightly form to the vacuum tube, and therefore the vacuum may become contaminated. This increase in gas molecules would be observed as an increase in the ion-induced afterpulse rate, and thus repeated afterpulse measurements were taken in 2015 and 2016. In 2015, a CAEN v1720 ADC (12 bit, 100 MHz) directly collected the PMT signal, whereas in 2016, a CAEN v1730 ADC (14 bit, 500 MHz) collected the PMT signal which had been amplified $\times 10$.

In 2015, the afterpulses following dark count signals were studied, with waveform collection triggered by the LED signal exceeding a certain threshold. For the 2016 data, the PMT was flashed with an LED light source ($\lambda = 470$ nm), and the ADC triggered on the pulse generator used to power the LED. The waveforms were processed with WARP.
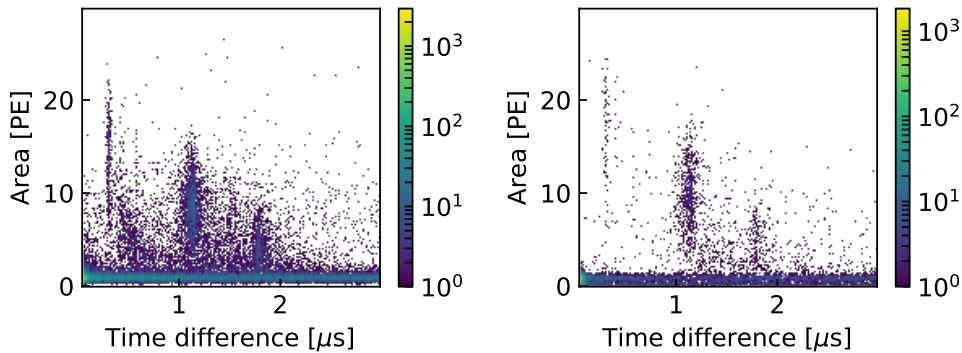
Figure B.15: Area in units of photoelectrons and time delay with respect to initial peak of afterpulse peaks. Left: 2015 data, Right: 2016 data.

Figure B.15 shows the area in units of photoelectrons and the time delay with respect to the initial peak of afterpulse peaks. Areas of high density are associated with afterpulses due to ions of particular mass-to-charge ratios. A time-uniform pedestal is observed for afterpulses with area corresponding to less than about 3 photoelectrons, which are not due to molecule ionisation, but other processes, such as electrons scattering off dynodes.

Figure B.16 shows the result of selecting those afterpulses with area greater than 3 photoelectrons, and projecting them onto the time delay axis. The afterpulse rates are calculated for each shaded region in Figure B.16.
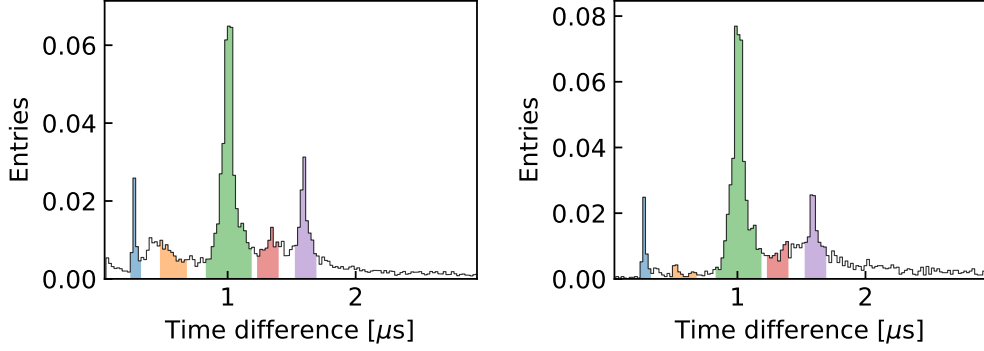
Figure B.16: Normalised distribution of afterpulse time delays. Left: 2015 data, Right: 2016 data.

The rates are normalised to the number of photoelectrons in the initial peak that triggers the electrons, i.e.,

$$\text{Rate} = \frac{\text{Number of afterpulse peaks}}{\text{Average number of photoelectrons per trigger pulse}}. \quad \text{(B.12)}$$

This normalisation accounts for the difference in the average number of photoelectrons per trigger pulse for the two datasets: 1.03 in 2015, and 1.31 in 2016, and makes the assumption that an event where two photoelectrons are emitted from the photocathode is twice as likely to produce afterpulses and an event where only one photoelectron is emitted from the photocathode. The individual afterpulse rates for the various ion peaks are shown in Table B.1. The ranges for each peak are the same in both datasets. The estimated mass-to-charge ratios are calculated by assuming the first peak to be due to hydrogen, and assuming a quadratic electric field between the photocathode and the first dynode.

Average time delay [μs]	M/Q	Identified ion	Events per trigger PE [10^{-4}]	
			2015	2016
0.30	1.00 (by def.)	H^+	0.91	0.80
0.59	4.00	He^+	1.25	0.39
1.02	11.96	CH_4^+	7.28	8.83
1.32	20.02	Ar^{++}	1.68	1.68
1.62	30.16	N_2^+	2.46	2.72

Table B.1: Afterpulse rates due to different ion peaks for waveforms from 2015 and 2016

The total afterpulse rates were measured to be 0.35 % in 2015, and 0.34 % in 2016. The comparable results between the two datasets, and the lack of increase in nitrogen or argon afterpulses, suggests that there has been no

considerable degradation of the vacuum and therefore that no significant leak has developed.

B.4 CONCLUSIONS

The PMT produced with a MgF_2 window by Hamamatsu is directly sensitive to liquid argon scintillation light with a wavelength of 128 nm. This was confirmed by the increase in dark count rate when the PMT was cooled in a liquid argon environment, which was not observed in a nitrogen environment. Furthermore, the mean waveform observed when an α emitting ^{241}Am source was placed with the PMT in liquid argon exhibited the two characteristic exponentially decaying components.

The gain of the MgF_2 PMT was measured and is comparable to other R11065-20 PMTs [166], with a gain of $6.5 \cdot 10^6$ electrons/photoelectron at an operating voltage of 1500 V.

Since Hamamatsu had indicated that this PMT may be susceptible to leaks into the vacuum tube, the afterpulse rate was measured twice, a year apart. No increase in afterpulse rate was observed, including for nitrogen and argon.

LIST OF TABLES

LIST OF FIGURES

BIBLIOGRAPHY

[1] D. Galbraith and C. Burgard. "Standard Model of Particle Physics.", 2012. URL http://davidgalbraith.org/portfolio/ux-standard-model-of-the-standard-model/, "CERN, Webfest".

[2] O. v. Baeyer, O. Hahn, and L. Meitner. "Magnetische Spektren der Beta-Strahlen des Radiums." *Phys. Zeit*, 12, pp. 1099–1101, 1911.

[3] J. Chadwick. "Intensitätsverteilung im magnetischen Spectrum der β-Strahlen von radium B+ C." *Verhandl. Dtsc. Phys. Ges.*, 16, p. 383, 1914.

[4] W. Pauli. "Offener Brief an die Gruppe der Radioaktiven bei der Gauverein-Tagung zu Tübingen.", 1930. URL http://www.dokspeicher.de/120295/, Zurich.

[5] F. L. Wilson. "Fermi's Theory of Beta Decay." *Am. J. Phys.*, 36, pp. 1150–1160, 1968. doi:10.1119/1.1974382.

[6] K. C. Wang. "A Suggestion on the Detection of the Neutrino." *Physical Review*, 61, p. 97, 1942.

[7] F. Reines and C. Cowan Jr. "A proposed experiment to detect the free neutrino." *Physical Review*, 90, p. 492, 1953.

[8] C. L. Cowan, F. Reines, F. B. Harrison, H. W. Kruse, and A. D. McGuire. "Detection of the Free Neutrino: a Confirmation." *Science*, 124, pp. 103–104, 1956. doi:10.1126/science.124.3212.103.

[9] C. D. Anderson and S. H. Neddermeyer. "Cloud Chamber Observations of Cosmic Rays at 4300 Meters Elevation and Near Sea-Level." *Phys. Rev.*, 50, pp. 263–271, 1936. doi:10.1103/PhysRev.50.263.

[10] J. Street and E. Stevenson. "New Evidence for the Existence of a Particle of Mass Intermediate Between the Proton and Electron." *Phys. Rev.*, 52, pp. 1003–1004, 1937. doi:10.1103/PhysRev.52.1003.

[11] F. Rasetti. "Disintegration of Slow Mesotrons." *Phys. Rev.*, 60, pp. 198–204, 1941. doi:10.1103/PhysRev.60.198.

[12] R. B. Leighton, C. D. Anderson, and A. J. Seriff. "The energy spectrum of the decay particles and the mass and spin of the mesotron." *Physical Review*, 75, p. 1432, 1949.

[13] G. Danby, J. Gaillard, K. A. Goulianos, L. Lederman, N. B. Mistry, M. Schwartz, and J. Steinberger. "Observation of High-Energy Neutrino Reactions and the Existence of Two Kinds of Neutrinos." *Phys. Rev. Lett.*, 9, pp. 36–44, 1962. doi:10.1103/PhysRevLett.9.36.

[14] K. Kodama *et al.* "Observation of tau neutrino interactions." *Phys. Lett. B*, 504, pp. 218–224, 2001. doi:10.1016/S0370-2693(01)00307-0. hep-ex/0012035.

[15] B. Cleveland, T. Daily, J. Davis, Raymond, J. R. Distel, K. Lande, C. Lee, P. S. Wildenhain, and J. Ullman. "Measurement of the solar electron neutrino flux with the Homestake chlorine detector." *Astrophys. J.*, 496, pp. 505–526, 1998. doi:10.1086/305343.

[16] F. Close. "Is the Sun still shining?" *Nature*, 284, pp. 507–508, 1980. doi:10.1038/284507a0.

[17] J. Farine. "Measurement of the rate of $\nu_e + d \rightarrow p + p + e^-$ interactions produced by B-8 solar neutrinos at the Sudbury Neutrino Observatory." *Phys. Atom. Nucl.*, 65, pp. 2147–2155, 2002. doi:10.1134/1.1530292.

[18] Z. Maki, M. Nakagawa, and S. Sakata. "Remarks on the unified model of elementary particles." *Prog. Theor. Phys.*, 28, pp. 870–880, 1962. doi:10.1143/PTP.28.870.

[19] B. Pontecorvo. "Mesonium and anti-mesonium." *Sov. Phys. JETP*, 6, p. 429, 1957.

[20] I. Esteban, M. Gonzalez-Garcia, A. Hernandez-Cabezudo, M. Maltoni, and T. Schwetz. "Global analysis of three-flavour neutrino oscillations: Synergies and tensions in the determination of θ 23, δ CP, and the mass ordering." *Journal of High Energy Physics*, 2019, pp. 1–35, 2019.

[21] S. Bilenky and C. Giunti. "Neutrinoless double-beta decay: a probe of physics beyond the standard model." *International Journal of Modern Physics A*, 30, p. 1530001, 2015.

[22] A. Smirnov. "The Mikheyev-Smirnov-Wolfenstein (MSW) Effect." In "International Conference on History of the Neutrino: 1930-2018," 2019. 1901.11473.

[23] X. Qian and P. Vogel. "Neutrino Mass Hierarchy." *Prog. Part. Nucl. Phys.*, 83, pp. 1–30, 2015. doi:10.1016/j.ppnp.2015.05.002. 1505.01891.

[24] F. Kaether, W. Hampel, G. Heusser, J. Kiko, and T. Kirsten. "Reanalysis of the GALLEX solar neutrino flux and source experiments." *Phys. Lett. B*, 685, pp. 47–54, 2010. doi:10.1016/j.physletb.2010.01.030. 1001.2731.

[25] J. Abdurashitov *et al.* "Measurement of the solar neutrino capture rate with gallium metal. III: Results for the 2002–2007 data-taking period." *Phys. Rev. C*, 80, p. 015807, 2009. doi:10.1103/PhysRevC.80.015807. 0901.2200.

[26] K. Abe, Y. Hayato, T. Iida, M. Ikeda, C. Ishihara *et al.* "Solar neutrino results in Super-Kamiokande-III." *Physical Review D*, 83, p. 052010, 2011.

[27] B. Aharmim *et al.* "Combined Analysis of all Three Phases of Solar Neutrino Data from the Sudbury Neutrino Observatory." *Phys. Rev. C*, 88, p. 025501, 2013. doi:10.1103/PhysRevC.88.025501. 1109.0763.

[28] G. Bellini, J. Benziger, D. Bick, S. Bonetti, G. Bonfini *et al.* "Precision measurement of the Be 7 solar neutrino interaction rate in Borexino." *Physical Review Letters*, 107, p. 141302, 2011.

[29] G. Bellini *et al.* "Measurement of the solar 8B neutrino rate with a liquid scintillator target and 3 MeV energy threshold in the Borexino detector." *Phys. Rev. D*, 82, p. 033006, 2010. doi:10.1103/PhysRevD.82.033006. 0808.2868.

[30] G. Bellini *et al.* "Neutrinos from the primary proton–proton fusion process in the Sun." *Nature*, 512, pp. 383–386, 2014. doi:10.1038/nature13702.

[31] A. Gando *et al.* "Reactor On-Off Antineutrino Measurement with KamLAND." *Phys. Rev. D*, 88, p. 033001, 2013. doi:10.1103/PhysRevD.88.033001. 1303.4667.

[32] D. Adey *et al.* "Measurement of the Electron Antineutrino Oscillation with 1958 Days of Operation at Daya Bay." *Phys. Rev. Lett.*, 121, p. 241805, 2018. doi:10.1103/PhysRevLett.121.241805. 1809.02261.

[33] G. Bak *et al.* "Measurement of Reactor Antineutrino Oscillation Amplitude and Frequency at RENO." *Phys. Rev. Lett.*, 121, p. 201801, 2018. doi:10.1103/PhysRevLett.121.201801. 1806.00248.

[34] M. G. Aartsen *et al.* "Determining neutrino oscillation parameters from atmospheric muon neutrino disappearance with three years of IceCube DeepCore data." *Phys. Rev. D*, 91, p. 072004, 2015. doi:10.1103/PhysRevD.91.072004. 1410.7227.

[35] K. Abe *et al.* "Atmospheric neutrino oscillation analysis with external constraints in Super-Kamiokande I-IV." *Phys. Rev. D*, 97, p. 072001, 2018. doi:10.1103/PhysRevD.97.072001. 1710.09126.

[36] P. Adamson *et al.* "Measurement of Neutrino and Antineutrino Oscillations Using Beam and Atmospheric Data in MINOS." *Phys. Rev. Lett.*, 110, p. 251801, 2013. doi:10.1103/PhysRevLett.110.251801. 1304.6335.

[37] K. Abe *et al.* "Combined Analysis of Neutrino and Antineutrino Oscillations at T2K." *Phys. Rev. Lett.*, 118, p. 151801, 2017. doi:10.1103/PhysRevLett.118.151801. 1701.00432.

[38] M. Acero *et al.* "New constraints on oscillation parameters from ν_e appearance and ν_μ disappearance in the NOvA experiment." *Phys. Rev. D*, 98, p. 032012, 2018. doi:10.1103/PhysRevD.98.032012. 1806.00096.

[39] B. Abi *et al.* "Long-baseline neutrino oscillation physics potential of the DUNE experiment." 2020. 2006.16043.

[40] K. Abe *et al.* "Hyper-Kamiokande Design Report." 2018. 1805.04163.

[41] K. Abe *et al.* "Physics potential of a long-baseline neutrino oscillation experiment using a J-PARC neutrino beam and Hyper-Kamiokande." *PTEP*, 2015, p. 053C02, 2015. doi:10.1093/ptep/ptv061. 1502.05199.

[42] M. K. Gaillard, P. D. Grannis, and F. J. Sciulli. "The Standard model of particle physics." *Rev. Mod. Phys.*, 71, pp. S96–S111, 1999. doi:10.1103/RevModPhys.71.S96. hep-ph/9812285.

[43] C. Wu, E. Ambler, R. Hayward, D. Hoppes, and R. Hudson. "Experimental Test of Parity Conservation in β Decay." *Phys. Rev.*, 105, pp. 1413–1414, 1957. doi:10.1103/PhysRev.105.1413.

[44] R. Marshak and E. Sudarshan. "Nature of the Four-Fermion Interaction." In "Padua-Venice International Conference, 1957," volume 109, p. 1860. 1958.

[45] E. Sudarshan and R. Marshak. "Chirality invariance and the universal Fermi interaction." *Phys. Rev.*, 109, pp. 1860–1860, 1958. doi:10.1103/PhysRev.109.1860.2.

[46] R. P. Feynman and M. Gell-Mann. "Theory of the Fermi interaction." *Physical Review*, 109, p. 193, 1958.

[47] M. Goldhaber, L. Grodzins, and A. Sunyar. "Helicity of Neutrinos." *Phys. Rev.*, 109, pp. 1015–1017, 1958. doi:10.1103/PhysRev.109.1015.

[48] M. Drewes. "The Phenomenology of Right Handed Neutrinos." *Int. J. Mod. Phys. E*, 22, p. 1330019, 2013. doi:10.1142/S0218301313300191. 1303.6912.

[49] B. Kayser. "Are neutrinos their own antiparticles?" volume 173, p. 012013. 2009. doi:10.1088/1742-6596/173/1/012013. 0903.0899.

[50] P. Minkowski. "$\mu \to e\gamma$ at a Rate of One Out of 10^9 Muon Decays?" *Phys. Lett. B*, 67, pp. 421–428, 1977. doi:10.1016/0370-2693(77)90435-X.

[51] T. Yanagida. "Horizontal Symmetry and Masses of Neutrinos." *Prog. Theor. Phys.*, 64, p. 1103, 1980. doi:10.1143/PTP.64.1103.

[52] R. N. Mohapatra and G. Senjanovic. "Neutrino Mass and Spontaneous Parity Nonconservation." *Phys. Rev. Lett.*, 44, p. 912, 1980. doi:10.1103/PhysRevLett.44.912.

[53] S. Davidson, E. Nardi, and Y. Nir. "Leptogenesis." *Phys. Rept.*, 466, pp. 105–177, 2008. doi:10.1016/j.physrep.2008.06.002. 0802.2962.

[54] C. Hagedorn, R. Mohapatra, E. Molinaro, C. Nishi, and S. Petcov. "CP Violation in the Lepton Sector and Implications for Leptogenesis." *Int. J. Mod. Phys. A*, 33, p. 1842006, 2018. doi:10.1142/S0217751X1842006X. 1711.02866.

[55] G. Benato. *Data Reconstruction and Analysis for the GERDA experiment*. Ph.D. thesis, University of Zurich, 2015.

[56] R. Mingazheva. *Calibration, Background Study, and Search for New Physics with the GERDA Experiment*. Ph.D. thesis, University of Zurich, 2019.

[57] S. Finch and W. Tornow. "Search for the β decay of 96 Zr." *Nucl. Instrum. Meth. A*, 806, pp. 70–74, 2016. doi:10.1016/j.nima.2015.09.098.

[58] R. Saakyan. "Two-Neutrino Double-Beta Decay." *Ann. Rev. Nucl. Part. Sci.*, 63, pp. 503–529, 2013. doi:10.1146/annurev-nucl-102711-094904.

[59] V. Tretyak and Y. Zdesenko. "Tables of the results of double Beta decay research." *Atom. Data Nucl. Data Tabl.*, 61, pp. 43–90, 1995. doi:10.1016/S0092-640X(95)90011-X.

[60] J. Engel and J. Menéndez. "Status and Future of Nuclear Matrix Elements for Neutrinoless Double-Beta Decay: A Review." *Rept. Prog. Phys.*, 80, p. 046301, 2017. doi:10.1088/1361-6633/aa5bc5. 1610.06548.

[61] O. Cremonesi and M. Pavan. "Challenges in double beta decay." *Advances in High Energy Physics*, 2014, 2014.

[62] S. Pascoli, S. Petcov, and T. Schwetz. "The Absolute neutrino mass scale, neutrino mass spectrum, majorana CP-violation and neutrinoless double-beta decay." *Nucl. Phys. B*, 734, pp. 24–49, 2006. doi:10.1016/j.nuclphysb.2005.11.003. hep-ph/0505226.

[63] N. Aghanim *et al.* "Planck 2018 results. VI. Cosmological parameters." 2018. 1807.06209.

[64] K. Nakamura *et al.* "Review of particle physics." *J. Phys. G*, 37, p. 075021, 2010. doi:10.1088/0954-3899/37/7A/075021.

[65] M. Aker, K. Altenmüller, M. Arenz, M. Babutzka, J. Barrett *et al.* "Improved upper limit on the neutrino mass from a direct kinematic method by KATRIN." *Physical review letters*, 123, p. 221802, 2019.

[66] G. Benato. "Effective Majorana Mass and Neutrinoless Double Beta Decay." *Eur. Phys. J. C*, 75, p. 563, 2015. doi:10.1140/epjc/s10052-015-3802-1. 1510.01089.

[67] M. Agostini *et al.* "Probing Majorana neutrinos with double-β decay." *Science*, 365, p. 1445, 2019. doi:10.1126/science.aav8613. 1909.02726.

[68] "The Large Enriched Germanium Experiment for Neutrinoless $\beta\beta$ Decay: LEGEND-1000 Preconceptual Design Report.", 2020.

[69] K. Lou *et al.* "Recent results of the Gotthard TPC experiment." In "4th International Symposium on Weak and Electromagnetic Interaction in Nuclei (WEIN 95)," pp. 192–203. 1995.

[70] C. Aalseth, F. Avignone III, R. Brodzinski, S. Cebrian, E. Garcia *et al.* "IGEX 76 Ge neutrinoless double-beta decay experiment: prospects for next generation experiments." *Physical Review D*, 65, p. 092007, 2002.

[71] H. V. Klapdor-Kleingrothaus, A. Dietz, L. Baudis, G. Heusser, I. Krivosheina *et al.* "Latest results from the Heidelberg-Moscow double beta decay experiment." *The European Physical Journal A-Hadrons and Nuclei*, 12, pp. 147–154, 2001.

[72] F. Descamps. "Neutrino Physics with SNO+." *Nucl. Part. Phys. Proc.*, 265-266, pp. 143–145, 2015. doi:10.1016/j.nuclphysbps.2015.06.037.

[73] A. Gando, Y. Gando, T. Hachiya, A. Hayashi, S. Hayashida *et al.* "Search for Majorana neutrinos near the inverted mass hierarchy region with KamLAND-Zen." *Physical review letters*, 117, p. 082503, 2016.

[74] J. Shirai. "Results and future plans for the KamLAND-Zen experiment." *J. Phys. Conf. Ser.*, 888, p. 012031, 2017. doi:10.1088/1742-6596/888/1/012031.

[75] G. Anton, I. Badhrees, P. Barbeau, D. Beck, V. Belov *et al.* "Search for neutrinoless double-β decay with the complete EXO-200 dataset." *Physical review letters*, 123, p. 161802, 2019.

[76] M. J. Jewell. *Search for neutrinoless double beta decay with EXO-200 and nEXO.* Ph.D. thesis, Stanford U., 2020.

[77] J. Aalbers *et al.* "DARWIN: towards the ultimate dark matter detector." *JCAP*, 11, p. 017, 2016. doi:10.1088/1475-7516/2016/11/017. 1606.07001.

[78] J. Martín-Albo, J. M. Vidal, P. Ferrario, M. Nebot-Guinot, J. Gómez-Cadenas *et al.* "Sensitivity of NEXT-100 to neutrinoless double beta decay." *Journal of High Energy Physics*, 2016, pp. 1–30, 2016.

[79] K. Han. "PandaX-III: Searching for Neutrinoless Double Beta Decay with High Pressure Gaseous Time Projection Chambers." *J. Phys. Conf. Ser.*, 1342, p. 012095, 2020. doi:10.1088/1742-6596/1342/1/012095. 1710.08908.

[80] C. Alduino, F. Alessandria, K. Alfonso, E. Andreotti, C. Arnaboldi *et al.* "First Results from CUORE: A Search for Lepton Number Violation via 0 ν β β Decay of Te 130." *Physical review letters*, 120, p. 132501, 2018.

[81] O. Azzolini, M. Barrera, J. Beeman, F. Bellini, M. Beretta *et al.* "First Result on the Neutrinoless Double-β Decay of Se 82 with CUPID-0." *Physical review letters*, 120, p. 232502, 2018.

[82] E. Armengaud, C. Augier, A. Barabash, F. Bellini, G. Benato *et al.* "The CUPID-Mo experiment for neutrinoless double-beta decay: performance and prospects." *The European Physical Journal C*, 80, pp. 1–15, 2020.

[83] C. E. Aalseth, N. Abgrall, E. Aguayo, S. Alvis, M. Amman *et al.*
"Search for Neutrinoless Double-β Decay in Ge 76 with the
Majorana Demonstrator." *Physical review letters*, 120, p. 132502, 2018.

[84] N. Abgrall *et al.* "The Large Enriched Germanium Experiment for
Neutrinoless Double Beta Decay (LEGEND)." *AIP Conf. Proc.*, 1894,
p. 020027, 2017. doi:10.1063/1.5007652. 1709.01980.

[85] M. Agostini *et al.* "Upgrade for Phase II of the Gerda experiment."
Eur. Phys. J. C, 78, p. 388, 2018. doi:10.1140/epjc/s10052-018-5812-2.
1711.01452.

[86] G. Douysset, T. Fritioff, C. Carlberg, I. Bergstrom, and M. Bjorkhage.
"Determination of the Ge-76 double beta decay Q value." *Phys. Rev.
Lett.*, 86, pp. 4259–4262, 2001. doi:10.1103/PhysRevLett.86.4259.

[87] K. Ackermann *et al.* "The GERDA experiment for the search of $0\nu\beta\beta$
decay in ^{76}Ge." *Eur. Phys. J. C*, 73, p. 2330, 2013.
doi:10.1140/epjc/s10052-013-2330-0. 1212.4067.

[88] M. Agostini *et al.* "Final Results of GERDA on the Search for
Neutrinoless Double-β Decay." *Physical Review Letters*, 125, p.
252502, 2020.

[89] "LNGS." https://www.lngs.infn.it/en/lngs-overview. Accessed:
2020-07-26.

[90] G. Bellini *et al.* "Cosmic-muon flux and annual modulation in
Borexino at 3800 m water-equivalent depth." *JCAP*, 05, p. 015, 2012.
doi:10.1088/1475-7516/2012/05/015. 1202.6403.

[91] M. Agostini *et al.* "Background-free search for neutrinoless double-β
decay of ^{76}Ge with GERDA." *Nature*, 544, p. 47, 2017.
doi:10.1038/nature21717. 1703.00570.

[92] J. J. Csáthy, T. Bode, J. Kratz, S. Schönert, and C. Wiesinger. "Optical
fiber read-out for liquid argon scintillation light." 2016. 1606.04254.

[93] A. C. Wegmann. *Characterization of the liquid argon veto of the GERDA
experiment and its application for the measurement of the ^{76}Ge half-life.*
Ph.D. thesis, U. Heidelberg (main), 2017.
doi:10.11588/heidok.00022568.

[94] C. Wiesinger. *No neutrinos not found: First exploration of neutrinoless
double beta decay half-lives beyond 10^{26} years.* Ph.D. thesis, Technische
Universität München, 2020.

[95] V. Gehman, S. Seibert, K. Rielage, A. Hime, Y. Sun, D. Mei, J. Maassen, and D. Moore. "Fluorescence Efficiency and Visible Re-emission Spectrum of Tetraphenyl Butadiene Films at Extreme Ultraviolet Wavelengths." *Nucl. Instrum. Meth. A*, 654, pp. 116–121, 2011. doi:10.1016/j.nima.2011.06.088. 1104.3259.

[96] V. Boccone *et al.* "Development of wavelength shifter coated reflectors for the ArDM argon dark matter detector." *JINST*, 4, p. P06001, 2009. doi:10.1088/1748-0221/4/06/P06001. 0904.0246.

[97] W. Shockley. "Currents to conductors induced by a moving point charge." *J. Appl. Phys.*, 9, pp. 635–636, 1938. doi:10.1063/1.1710367.

[98] S. Ramo. "Currents induced by electron motion." *Proc. Ire.*, 27, pp. 584–585, 1939. doi:10.1109/JRPROC.1939.228757.

[99] D. Gonzalez *et al.* "Pulse shape discrimination in the IGEX experiment." *Nucl. Instrum. Meth. A*, 515, pp. 634–643, 2003. doi:10.1016/j.nima.2003.06.008. hep-ex/0302018.

[100] M. Agostini *et al.* "Production, characterization and operation of ^{76}Ge enriched BEGe detectors in GERDA." *Eur. Phys. J. C*, 75, p. 39, 2015. doi:10.1140/epjc/s10052-014-3253-0. 1410.0853.

[101] M. Agostini *et al.* "Characterization of 30^{76}Ge enriched Broad Energy Ge detectors for GERDA Phase II." *Eur. Phys. J. C*, 79, p. 978, 2019. doi:10.1140/epjc/s10052-019-7353-8. 1901.06590.

[102] R. J. Cooper, D. C. Radford, P. A. Hausladen, and K. Lagergren. "A novel HPGe detector for gamma-ray tracking and imaging." *Nuclear Instruments and Methods in Physics Research Section A: Accelerators, Spectrometers, Detectors and Associated Equipment*, 665, pp. 25–32, 2011.

[103] A. Domula, M. Hult, Y. Kermaidic, G. Marissens, B. Schwingenheuer, T. Wester, and K. Zuber. "Pulse shape discrimination performance of Inverted Coaxial Ge detectors." *Nucl. Instrum. Meth. A*, 891, pp. 106–110, 2018. doi:10.1016/j.nima.2018.02.056. 1711.01433.

[104] V. DAndrea. *Improvement of Performance and Background Studies in Gerda Phase II*. Ph.D. thesis, Ph. D. Thesis, Gran Sasso Science Institute (GSSI), 2017.

[105] "ROOT." URL http://root.cern.ch.

[106] A. Lazzaro. *Signal processing and event classification for a background free neutrinoless double beta decay search with the GERDA experiment*. Ph.D. thesis, Munich, Tech. U., 2019.

[107] M. Agostini *et al.* "Pulse shape discrimination for GERDA Phase I data." *Eur. Phys. J. C*, 73, p. 2583, 2013. doi:10.1140/epjc/s10052-013-2583-7. 1307.2610.

[108] M. Agostini *et al.* "Results on $\beta\beta$ decay with emission of two neutrinos or Majorons in^{76} Ge from GERDA Phase I." *Eur. Phys. J. C*, 75, p. 416, 2015. doi:10.1140/epjc/s10052-015-3627-y. 1501.02345.

[109] M. Agostini *et al.* "Modeling of GERDA Phase II data." *JHEP*, 03, p. 139, 2020. doi:10.1007/JHEP03(2020)139. 1909.02522.

[110] M. Agostini *et al.* "Results on Neutrinoless Double-β Decay of ^{76}Ge from Phase I of the GERDA Experiment." *Phys. Rev. Lett.*, 111, p. 122503, 2013. doi:10.1103/PhysRevLett.111.122503.

[111] M. Agostini *et al.* "Limit on Neutrinoless Double Beta Decay of ^{76}Ge by GERDA." *Phys. Procedia*, 61, pp. 828–837, 2015. doi:10.1016/j.phpro.2015.06.002.

[112] M. Agostini *et al.* "Improved Limit on Neutrinoless Double-β Decay of ^{76}Ge from GERDA Phase II." *Phys. Rev. Lett.*, 120, p. 132503, 2018. doi:10.1103/PhysRevLett.120.132503. 1803.11100.

[113] T. R. Rodriguez and G. Martinez-Pinedo. "Energy density functional study of nuclear matrix elements for neutrinoless $\beta\beta$ decay." *Phys. Rev. Lett.*, 105, p. 252503, 2010. doi:10.1103/PhysRevLett.105.252503. 1008.5260.

[114] M. Mustonen and J. Engel. "Large-scale calculations of the double-β decay of ^{76}Ge,^{130} Te,^{136} Xe, and ^{150}Nd in the deformed self-consistent Skyrme quasiparticle random-phase approximation." *Phys. Rev. C*, 87, p. 064302, 2013. doi:10.1103/PhysRevC.87.064302. 1301.6997.

[115] N. Lpez Vaquero, T. R. Rodrguez, and J. L. Egido. "Shape and pairing fluctuations effects on neutrinoless double beta decay nuclear matrix elements." *Phys. Rev. Lett.*, 111, p. 142501, 2013. doi:10.1103/PhysRevLett.111.142501. 1401.0650.

[116] M. Horoi and A. Neacsu. "Shell model predictions for ^{124}Sn double-β decay." *Phys. Rev. C*, 93, p. 024308, 2016. doi:10.1103/PhysRevC.93.024308. 1511.03711.

[117] J. Hyvrinen and J. Suhonen. "Neutrinoless $\beta\beta$ decays to excited 0^+ states and the Majorana-neutrino mass." *Phys. Rev. C*, 93, pp. 1–15, 2016. doi:10.1103/PhysRevC.93.064306.

[118] J. Barea, J. Kotila, and F. Iachello. "$0\nu\beta\beta$ and $2\nu\beta\beta$ nuclear matrix elements in the interacting boson model with isospin restoration."

Phys. Rev., C91, p. 034304, 2015. doi:10.1103/PhysRevC.91.034304. 1506.08530.

[119] J. Menéndez. "Neutrinoless $\beta\beta$ decay mediated by the exchange of light and heavy neutrinos: The role of nuclear structure correlations." *J. Phys. G*, 45, p. 014003, 2018. doi:10.1088/1361-6471/aa9bd4. 1804.02105.

[120] L. Song, J. Yao, P. Ring, and J. Meng. "Nuclear matrix element of neutrinoless double-β decay: Relativity and short-range correlations." *Phys. Rev. C*, 95, p. 024305, 2017. doi:10.1103/PhysRevC.95.024305. 1702.02448.

[121] F. ˇSimkovic, A. Smetana, and P. Vogel. "$0\nu\beta\beta$ nuclear matrix elements, neutrino potentials and SU(4) symmetry." *Phys. Rev. C*, 98, p. 064325, 2018. doi:10.1103/PhysRevC.98.064325. 1808.05016.

[122] D.-L. Fang, A. Faessler, and F. r. Simkovic. "$0\nu\beta\beta$ -decay nuclear matrix element for light and heavy neutrino mass mechanisms from deformed quasiparticle random-phase approximation calculations for ^{76}Ge, ^{82}Se, ^{130}Te, ^{136}Xe , and ^{150}Nd with isospin restoration." *Phys. Rev. C*, 97, p. 045503, 2018. doi:10.1103/PhysRevC.97.045503. 1803.09195.

[123] L. Coraggio, A. Gargano, N. Itaco, R. Mancino, and F. Nowacki. "Calculation of the neutrinoless double-β decay matrix element within the realistic shell model." *Phys. Rev. C*, 101, p. 044315, 2020. doi:10.1103/PhysRevC.101.044315. 2001.00890.

[124] D. Adams *et al.* "Improved Limit on Neutrinoless Double-Beta Decay in ^{130}Te with CUORE." *Phys. Rev. Lett.*, 124, p. 122501, 2020. doi:10.1103/PhysRevLett.124.122501. 1912.10966.

[125] M. Agostini *et al.* "The first search for bosonic super-WIMPs with masses up to 1 MeV/c^2 with GERDA." *Phys. Rev. Lett.*, 125, p. 011801, 2020. doi:10.1103/PhysRevLett.125.011801. 2005.14184.

[126] M. Agostini *et al.* "$2\nu\beta\beta$ decay of ^{76}Ge into excited states with GERDA Phase I." *J. Phys. G*, 42, p. 115201, 2015. doi:10.1088/0954-3899/42/11/115201. 1506.03120.

[127] S. R. Elliott and P. Vogel. "Double beta decay." *Ann. Rev. Nucl. Part. Sci.*, 52, pp. 115–151, 2002. doi:10.1146/annurev.nucl.52.050102.090641. hep-ph/0202264.

[128] G. Gilmore. *Practical gamma-ray spectroscopy*. John Wiley & Sons, 2011.

[129] U. Fano. "Ionization Yield of Radiations. 2. The Fluctuations of the Number of Ions." *Phys. Rev.*, 72, pp. 26–29, 1947. doi:10.1103/PhysRev.72.26.

[130] R. C. Alig, S. Bloom, and C. W. Struck. "Scattering by ionization and phonon emission in semiconductors." *Phys. Rev. B*, 22, pp. 5565–5582, 1980. doi:10.1103/PhysRevB.22.5565.

[131] N. Strokan, V. Ajdačić, and B. Lalović. "Measurements of the Fano factor in germanium." *Nuclear Instruments and methods*, 94, pp. 147–149, 1971.

[132] B. Lowe. "Measurements of Fano factors in silicon and germanium in the low-energy X-ray region." *Nuclear Instruments and Methods in Physics Research Section A: Accelerators, Spectrometers, Detectors and Associated Equipment*, 399, pp. 354–364, 1997.

[133] M. Agostini *et al.* "Improvement of the energy resolution via an optimized digital signal processing in GERDA Phase I." *Eur. Phys. J. C*, 75, p. 255, 2015. doi:10.1140/epjc/s10052-015-3409-6. 1502.04392.

[134] M. Miloradovic. *Characterisation of Inverted Coaxial Detectors and Calibration Source Production for the GERDA Experiment*. Ph.D. thesis, University of Zurich, 2020.

[135] "Gamma rays energy values." URL http://www.radiochemistry.org/periodictable.

[136] R. L. Coldwell and G. P. Lasche. "Experimental measurements of Doppler broadening of escape peaks in HPGe detectors." *Journal of Radioanalytical and Nuclear Chemistry*, 307, pp. 2509–2512, 2016.

[137] J. C. Slater. "Atomic radii in crystals." *The Journal of Chemical Physics*, 41, pp. 3199–3204, 1964.

[138] F. Froborg. *Calibration of Phase I of the GERDA Double Beta Decay Experiment*. Ph.D. thesis, University of Zurich, 2012.

[139] E. L. Hull, J. Xing, D. L. Friesel, R. H. Pehl, N. W. Madden, T. W. Raudorf, and L. S. Varnell. "Charge Collection Physics in Semiconductor Detectors." 1996.

[140] N. Abgrall *et al.* "New limits on Bosonic Dark Matter, Solar Axions, Pauli Exclusion Principle Violation, and Electron Decay from the Majorana Demonstrator." *Phys. Rev. Lett.*, 118, p. 161801, 2017. doi:10.1103/PhysRevLett.118.161801. 1612.00886.

[141] M. Green. "LEGEND-1000 Simulations and Background Model.", 2020.

[142] P. Luke, F. Goulding, and N. Madden. "Low capacitance large volume shaped-field germanium detector." *IEEE Transactions on Nuclear Science*, 36(1), pp. 926–930, 1989.

[143] P. Krause. "The Liquid Argon Instrumentation of GERDA and LEGEND200." Neutrino 2020, 2020. URL https://nusoft.fnal.gov/nova/nu2020postersession/pdf/posterPDF-365.pdf.

[144] N. Abgrall *et al.* "The Majorana Demonstrator radioassay program." *Nucl. Instrum. Meth. A*, 828, pp. 22–36, 2016. doi:10.1016/j.nima.2016.04.070. 1601.03779.

[145] Y. Efremenko *et al.* "Use of poly(ethylene naphthalate) as a self-vetoing structural material." *JINST*, 14, p. P07006, 2019. doi:10.1088/1748-0221/14/07/P07006. 1901.03579.

[146] S. Alvis *et al.* "A Search for Neutrinoless Double-Beta Decay in ^{76}Ge with 26 kg-yr of Exposure from the MAJORANA DEMONSTRATOR." *Phys. Rev. C*, 100, p. 025501, 2019. doi:10.1103/PhysRevC.100.025501. 1902.02299.

[147] P. Barton, P. Luke, M. Amman, Y.-D. Chan, J. Detwiler, J. Loach, R. Martin, A. Poon, C. Tindall, and K. Vetter. "Low-noise low-mass front end electronics for low-background physics experiments using germanium detectors." In "2011 IEEE Nuclear Science Symposium and Medical Imaging Conference," pp. 1976–1979. 2011. doi:10.1109/NSSMIC.2011.6154397.

[148] I. Guinn *et al.* "Low Background Signal Readout Electronics for the MAJORANA DEMONSTRATOR." *J. Phys. Conf. Ser.*, 606, p. 012009, 2015. doi:10.1088/1742-6596/606/1/012009. 1502.03174.

[149] M. Willers. "Signal Readout Electronics for the LEGEND-200 Experiment." Neutrino 2020, 2020. URL https://nusoft.fnal.gov/nova/nu2020postersession/pdf/posterPDF-284.pdf.

[150] J. Heise. "The Sanford Underground Research Facility." *J. Phys. Conf. Ser.*, 1342, p. 012085, 2020. doi:10.5281/zenodo.1300395. 1710.11584.

[151] F. Duncan, A. Noble, and D. Sinclair. "The construction and anticipated science of SNOLAB." *Ann. Rev. Nucl. Part. Sci.*, 60, pp. 163–180, 2010. doi:10.1146/annurev.nucl.012809.104513.

[152] N. Smith. "The SNOLAB deep underground facility." *Eur. Phys. J. Plus*, 127, p. 108, 2012. doi:10.1140/epjp/i2012-12108-9.

[153] J.-P. Cheng *et al.* "The China Jinping Underground Laboratory and its Early Science." *Ann. Rev. Nucl. Part. Sci.*, 67, pp. 231–251, 2017. doi:10.1146/annurev-nucl-102115-044842. 1801.00587.

[154] C. Wiesinger, L. Pandola, and S. Schönert. "Virtual depth by active background suppression: Revisiting the cosmic muon induced background of GERDA Phase II." *Eur. Phys. J. C*, 78, p. 597, 2018. doi:10.1140/epjc/s10052-018-6079-3. 1802.05040.

[155] N. McFadden, S. R. Elliott, M. Gold, D. E. Fields, K. Rielage, R. Massarczyk, and R. Gibbons. "Large-Scale, Precision Xenon Doping of Liquid Argon." 2020. 2006.09780.

[156] H. Back, A. Alton, F. Calaprice, C. Galbiati, A. Goretti, C. Kendziora, B. Loer, D. Montanari, P. Mosteiro, and S. Pordes. "Depleted argon from underground sources." *Phys. Procedia*, 37, pp. 1105–1112, 2012. doi:10.1016/j.phpro.2012.04.099.

[157] "The Large Enriched Germanium Experiment for Neutrinoless $\beta\beta$ Decay: Legend-200 at Lngs.", 2018. URL http://pessina.mib.infn.it/Biblio/Biblio_Articoli/20180319Legend-200_proposal_submitted.pdf.

[158] L. Baudis, G. Benato, P. Carconi, C. M. Cattadori, P. De Felice, K. Eberhardt, R. Eichler, A. Petrucci, M. Tarka, and M. Walter. "Production and characterization of ^{228}Th calibration sources with low neutron emission for GERDA." *JINST*, 10, p. P12005, 2015. doi:10.1088/1748-0221/10/12/P12005. 1508.05731.

[159] M. Boswell *et al.* "MaGe-a Geant4-based Monte Carlo Application Framework for Low-background Germanium Experiments." *IEEE Trans. Nucl. Sci.*, 58, pp. 1212–1220, 2011. doi:10.1109/TNS.2011.2144619. 1011.3827.

[160] "GEANT4." https://geant4.web.cern.ch/.

[161] P. D. Group, P. Zyla, R. Barnett, J. Beringer, O. Dahl *et al.* "Review of particle physics." *Progress of Theoretical and Experimental Physics*, 2020, p. 083C01, 2020.

[162] R. Martin *et al.* "Determining the Drift Time of Charge Carriers in P-Type Point-Contact HPGe Detectors." *Nucl. Instrum. Meth. A*, 678, pp. 98–104, 2012. doi:10.1016/j.nima.2012.02.047. 1110.0131.

[163] "Photomultiplier tube." https://en.wikipedia.org/wiki/Photomultiplier_tube.

[164] S. DAmato. "SandBox: A facility for XENON photosensors characterization and measurements of photocathode uniformity.", 2016.

[165] L. Baudis, S. D'Amato, G. Kessler, A. Kish, and J. Wulf. "Measurements of the position-dependent photo-detection sensitivity of the Hamamatsu R11410 and R8520 photomultiplier tubes." 2015. 1509.04055.

[166] M. Walter. *Background Reduction Techniques for the GERDA Experiment*. Ph.D. thesis, University of Zurich, 2015.

[167] A. Behrens. *Light Detectors for the XENON100 and XENON1T Dark Matter Search Experiments*. Ph.D. thesis, University of Zurich, 2014.

[168] A. Brown. *Search for Elastic and Inelastic Dark Matter Interactions in XENON1T and Light Detection for XENONnT*. Ph.D. thesis, University of Zurich, 2020.

[169] J. Wulf. *Direct Dark Matter Search with XENON1T and Developments for Multi-Ton Liquid Xenon Detectors*. Ph.D. thesis, University of Zurich, 2018.

[170] L. Baudis, G. Benato, R. Dressler, F. Piastra, I. Usoltsev, and M. Walter. "Enhancement of Light Yield and Stability of Radio-Pure Tetraphenyl-Butadiene Based Coatings for VUV Light Detection in Cryogenic Environments." *JINST*, 10, p. P09009, 2015. doi:10.1088/1748-0221/10/09/P09009. 1503.05349.

ACKNOWLEDGMENTS